STOCHASTIC GEOMETRY BASED PERFORMANCE STUDY IN 5G WIRELESS NETWORKS

by

Zekun Zhang

A dissertation submitted in partial fulfillment
of the requirements for the degree

of

DOCTOR OF PHILOSOPHY

in

Electrical Engineering

Approved:

Rose Qingyang Hu, Ph.D. Major Professor	Jacob Gunther, Ph.D. Committee Member
Bedri Cetiner, Ph.D. Committee Member	Don Cripps, Ph.D. Committee Member
Haitao Wang, Ph.D. Committee Member	Richard S. Inouye, Ph.D. Vice Provost for Graduate Studies

UTAH STATE UNIVERSITY
Logan, Utah

2019

ABSTRACT

Stochastic Geometry Based Performance Study in 5G Wireless Networks

by

Zekun Zhang, Doctor of Philosophy

Utah State University, 2019

Major Professor: Rose Qingyang Hu, Ph.D.
Department: Electrical and Computer Engineering

As the complexity of modern cellular networks continuously increases along with the advancement of technologies and the explosion of mobile data traffic, conventional large scale system level simulations and analytical models become either overly complicated or less tractable. Therefore, novel analytical models are actively pursued. In recent years, stochastic geometry has been recognized as a powerful mathematical tool that can be used to model and analyze the key performance metrics of cellular networks. In this dissertation, stochastic geometry based mathematical models are developed to analyze the performance of some key 5G mobile technologies. This dissertation mainly focuses on three 5G technologies: Device-to-Device (D2D) communication, Non-orthogonal multiple access (NOMA), and ultra-dense networks (UDNs).

In the research on D2D communication, two schemes are proposed to support underlaid D2D communication in 5G cellular networks. The performance of the proposed schemes is analyzed in a system modeled by a 2-tier Poisson point process (PPP) and validated by simulations.

In the research on NOMA, analytical frameworks are developed to evaluate the performance of NOMA for both downlink and uplink 5G dense networks. Distinguished from the

existing publications on NOMA, the framework developed in this dissertation is the first one that considers the dense cellular network model with strong inter-cell interference.

In the research on UND, a dominant BS (base station)-based approximation framework is developed to address the short-range propagation features UDN. By applying reasonable mathematical approximations, the tractability of the PPP model is preserved and the closed form solution is derived. The numerical results demonstrate that the developed analytical model is accurate in a wide range of network densities.

The analysis conducted in this dissertation demonstrates that stochastic geometry models can serve as powerful tools to analyze the performance of 5G technologies in a dense wireless network deployment. The frameworks developed in this dissertation provide general yet powerful analytical tools that can be readily extended to facilitate other research in wireless networks.

(175 pages)

PUBLIC ABSTRACT

Stochastic Geometry Based Performance Study in 5G Wireless Networks

Zekun Zhang

As the complexity of modern cellular networks continuously increases along with the evolution of technologies and the quick explosion of mobile data traffic, conventional large scale system level simulations and analytical tools become either too complicated or less tractable and accurate. Therefore, novel analytical models are actively pursued. In recent years, stochastic geometry models have been recognized as powerful tools to analyze the key performance metrics of cellular networks. In this dissertation, stochastic geometry based analytical models are developed to analyze the performance of some key technologies proposed for 5G mobile networks. Particularly, Device-to-Device (D2D) communication, Non-orthogonal multiple access (NOMA), and ultra-dense networks (UDNs) are investigated and analyzed by stochastic geometry models, more specifically, Poisson Point Process (PPP) models.

D2D communication enables direct communication between mobile users in proximity to each other bypassing base station (BS). Embedding D2D communication into existing cellular networks brings many benefits such as improving spectrum efficiency, decreasing power energy consumption, and enabling novel location-based services. However, these benefits may not be fully exploited if the co-channel interference among D2D users and cellular users is not properly tackled. In this dissertation, various frequency reuse and power control schemes are proposed, aiming at mitigating the interference between D2D users and conventional cellular users. The performance gain of proposed schemes is analyzed on a system modeled by a 2-tier PPP and validated by numerical simulations.

NOMA is a promising radio access technology for 5G cellular networks. Different with widely applied orthogonal multiple access (OMA) such as orthogonal frequency division

multiple access (OFDMA) and single carrier frequency division multiple access (SC-FDMA), NOMA allows multiple users to use the same frequency/time resource and offers many advantages such as improving spectral efficiency, enhancing connectivity, providing higher cell-edge throughput, and reducing transmission latency. Although some initial performance analysis has been done on NOMA with single cell scenario, the system level performance of NOMA in a multi-cell scenario is not investigated in existing work. In this dissertation, analytical frameworks are developed to evaluate the performance of a wireless network with NOMA on both downlink and uplink. Distinguished from existing publications on NOMA, the framework developed in this dissertation is the first one that takes inter-cell interference into consideration.

UDN is another key technology for 5G wireless networks to achieve high capacity and coverage. Due to the existence of line-of-sight (LoS)/non-line-of-sight (NLoS) propagation and bounded path loss behavior in UDN networks, the tractability of the original PPP model diminishes when analyzing the performance of UDNs. Therefore, a dominant BS (base station)-based approximation model is developed in this dissertation. By applying reasonable mathematical approximations, the tractability of the PPP model is preserved and the closed form solution can be derived. The numerical results demonstrate that the developed analytical model is accurate in a wide range of network densities.

The analysis conducted in this dissertation demonstrates that stochastic geometry models can serve as powerful tools to analyze the performance of 5G technologies in a dense wireless network deployment. The frameworks developed in this dissertation provide general yet powerful analytical tools that can be readily extended to facilitate other research in wireless networks.

ACKNOWLEDGMENTS

First and foremost, I want to express my gratitude and appreciation to my major Ph.D. advisor Dr. Rose Qingyang Hu for her countless hours and efforts spent on helping me during every phase of my research. I have learned tremendously from her solid technical knowledge, great sense for research directions, strong writing and presentation skills. I also want to thank my committee members, Dr. Jacob Gunther, Dr. Bedri Cetiner, Dr. Don Cripps and Dr. Haitao Wang, for their excellent courses and invaluable help, and NSF grant NeTS-1423348, ECCS-1308006 and EARS-1547312 for providing the funding which has allowed me to focus my time and energy on this research. Finally, I would like to thank my parents and friends for their support during my Ph.D. journey.

Zekun Zhang

CONTENTS

LIST OF TABLES

LIST OF FIGURES

ACRONYMS

PPP	Poisson Point Process
CDF	Cumulative Distribution Function
CCDF	Complementary Cumulative Distribution Function
PDF	Probability Density Function
BS	Base Station
UE	User Equipment
SNR	Signal-to-noise Ratio
SINR	Signal-to-interference-plus-noise Ratio
D2D	Device-to-Device
CUE	Cellular User Equipment
DUE	D2D User Equipment
FFR	Fractional Frequency Reuse
FPC	Fractional Power Control
NOMA	Non-orthogonal Multiple Access
OMA	Orthogonal Multiple Access
UDN	Ultra Dense Network
LoS	Line-of-sight
NLoS	Non-ling-of-sight

CHAPTER 1

Introduction

As the long-term evolution (LTE) system embodying 4G is reaching maturity, the next generation (5G) wireless networks have been fully fledged and are about to be deployed in the near future. Compared to the current 4G LTE networks, 5G networks are expected to provide ultra-high data rate (typically in Gbps order), extremely low latency, massive connectivity, and significantly improved user quality of service (QoS) [1]. Among the typical service requirements for 5G systems, ultra-high data rate, which is about 1000x current 4G technologies, is considered as the most challenging objective. Therefore, technologies that are promising to improve the spectral efficiency of the system, such as Device-to-Device (D2D) communication, non-orthogonal multiple access (NOMA), and ultra-dense network (UDN), have attracted tremendous attention in both academia and industry.

In the development of the technologies aiming at improving the spectral efficiency of the 5G system, one of the biggest challenges is to combat inter-cell interference. However, until just a few years ago, the mathematical performance analysis incorporating inter-cell interference is only available by resorting to some overly simplified and idealized models such as Wyner model [2] and regular hexagonal (or square) lattice. The results acquired from these models can be inaccurate in general and do not provide much insightful guidance to the performance of most users in a system. Moreover, the tractability and accuracy of these models can be further deteriorated when they are used for more complicated heterogeneous and ad hoc deployments [3]. An alternative to the aforementioned models is to exhaustively simulate the networks and then take the average over many sources of randomness such as channel fading distributions, nodes locations, and noise. Although system-level simulations are indispensable for cellular network analysis and design, this approach tends to be extremely time-consuming, overly complicated, and error-prone [4].

Despite being extensively desired and pursued, tractable models that accurately model

inter-cell interference in large scale multi-cell wireless networks were unavailable in the past decades until the stochastic geometry model was introduced a few years ago [3]. In recent years, stochastic geometry model has been recognized as a powerful tool for analyzing the performance of multi-cell systems. Among various stochastic geometry models, homogeneous Poisson point process (PPP) has become a widely adopted model owing to its ability to yield tractable yet accurate results. Although the approach of applying PPP to conventional downlink system is demonstrated in [3], how to extend PPP to analyze the complicated schemes in dense heterogeneous 5G wireless networks is not apparent. As cellular networks evolve to introduce multi-tiers of communications into the networks, provide different services for various users, and densify the deployment of BS, many challenges arise for stochastic geometry analysis due to the extra complexity brought by new technologies proposed for 5G mobile networks. The main objective of this dissertation is to address these challenges by providing accurate yet tractable solutions.

This introductory chapter consists of three parts. Section 1.1 provides the background knowledge on why stochastic geometry model is a powerful tool to yield accurate and tractable analytical results for large-scale multi-cell cellular networks. Section 1.2 briefly introduces the specific 5G technologies studied in this dissertation. The contributions of this dissertation for each of these technologies are also highlighted. Finally the dissertation outline is provided in Section 1.3.

1.1 Stochastic Geometry Tool for Analyzing Cellular Networks

Although the initial idea of modeling cellular networks by using stochastic geometry tools was started as early as 1997 [5], the key metrics such as coverage and rate was not in the scope of the study. Instead of assuming the location of base stations (BSs) is deterministic as in regular grid models, stochastic geometry model assumes the BSs are randomly placed in the space following certain point process. So far there are various point processes that have been proposed to model cellular networks, such as homogeneous PPP [3], determinantal Point Processes [6], hard-core processes [7], and so on. Among all these point processes, homogeneous PPP is the most widely used model due to its tractability and accuracy.

Therefore, this dissertation focuses on homogeneous PPP as well as its variations. As inhomogeneous PPP is rarely used in the wireless communications research, PPP is simply used to refer homogeneous PPP if not specified throughout the dissertation.

PPP model assumes that the locations of BSs follow a PPP of intensity λ. Perhaps counter-intuitively, introducing additional resource of randomness (the location of BSs) actually makes the model more tractable and accurate to evaluate the key metrics of system performance such as coverage probability (distribution of signal-to-interference-plus-noise ratio (SINR)) and average achievable data rate. The insight behind this fact is that the locations of BSs are all independent in the PPP model and hence substantial stochastic geometry tools can be brought to facilitate the analysis [8]. For a more comprehensive exposition on the PPP model, interested readers can refer to [4] which is a concise tutorial or [9] which is a thorough book.

As demonstrated in [3], the PPP model is significantly more tractable than traditional regular grid model and can evaluate a real deployment at least as accurately as the grid model. As the deployment of modern networks tends to be opportunistic, irregular, and dense, the PPP model is envisaged to be increasingly close to the real deployment.

Although the distribution of SINR can be derived in a closed form with the plain PPP model proposed in [3], this succinct result is only available for some simple scenarios, such as a conventional single tier downlink cellular network. The choice of large-scale and small-scale channel fading models also affects the tractability of the PPP model significantly. As the cellular network continues to evolve with more complicated technologies, many challenges have arisen for analyzing the performance of these technologies. In the next section, the selected 5G technologies studied in this dissertation are introduced along with the contributions of this dissertation on each of them.

1.2 Key 5G Technologies

In order to meet the exponentially increasing mobile traffic demand [10], 5G cellular networks are expected to provide better services such as higher data rate, massive connectivity, and lower latency. To realize these expectations, many new technologies are envisaged

to be included in 5G and the 5G network architecture will be significantly different from the existing ones. To facilitate the design of novel technologies, accurate yet tractable analytical models are actively pursued. Although the original plain PPP model works fine for analyzing conventional cellular networks, it is not directly implementable for 5G networks with new and complicated features. Recall that the conventional homogeneous cellular network mainly consists of one tier macro BS and the users are typically multiplexed in orthogonal access schemes. By applying the PPP model, the SINR distribution and the average achievable rate for a typical user, in such a simple scenario, can be derived in a neat form [3, 11]. Unfortunately, the structure of the envisaged 5G networks is much more complicated than the existing networks and how to apply PPP to these new network scenarios is not apparent. This dissertation focuses on analyzing the performance of new 5G technologies by utilizing stochastic geometries tools. As there are numerous technologies proposed for 5G, by no means can this dissertation cover all of them. Instead, three typical technologies, namely D2D communication, NOMA, and UDN, are the focuses of this dissertation and comprehensively investigated. These technologies are briefly introduced in the rest of this section, together with the contributions of this dissertation on each of them.

1.2.1 D2D communication

D2D communication enables two nearby users to communicate with each other bypassing the BS. In a traditional cellular network, all communications must go through the BS regardless of the distance between the source device and the destination device. This architecture is not quite efficient when two communicating devices are close to each other, especially when supporting the prevalence of high data rate services in proximity (e.g., video sharing, online game, local social networking). As such local services are booming, D2D communication can greatly improve system capacity as well as user experience.

In the majority of the literature and so as in this dissertation, D2D communications are proposed to share the same spectrum with cellular communications (i.e., underlay in-band D2D) [12]. Although embedding D2D communication into an existing cellular system possesses many potential gains mentioned above, it also introduces new problems that must

be solved properly to acquire the expected gains [13]. In particular, the co-channel interference between cellular users and D2D users must be coordinated to achieve the expected benefits. In this dissertation, two new schemes are proposed to address this problem. In the first scheme, fractional power control (FPC) and fractional frequency reuse (FFR) are exploited to mitigate the interference between uplink cellular users and D2D users. In the second scheme, a distance-based power control scheme for D2D users is proposed to achieve the expected performance gains without generating evident interference to uplink cellular users. Both proposed schemes are analyzed by stochastic geometry model based on PPP and validated by simulations.

1.2.2 NOMA

Non-orthogonal multiple access (NOMA), recognized as a promising candidate radio access technology (RAT) in the 5G wireless system, has received tremendous attention lately. In contrast to orthogonal multiple access (OMA), NOMA allows multiple users to use the same frequency/time resource at the same time and offers many advantages such as improving spectral efficiency, enhancing connectivity, providing higher cell-edge throughput, and reducing transmission latency [14–17]. Generally NOMA can be classified into two categories, namely code domain NOMA (CD-NOMA) and power domain NOMA (PD-NOMA). CD-NOMA utilizes different codes on the same resource while PD-NOMA assigns users with distinct power levels to achieve the multiplexing gain. CD-NOMA can obtain a spreading gain at the cost of more consumed bandwidth. This dissertation focuses on PD-NOMA, which multiplexes users in the power domain.

As NOMA has attracted more and more attention from both academia and industry, a tractable analytical model that is able to evaluate the performance of NOMA at the system level is greatly desired. In this dissertation, frameworks that explicitly take inter-cell interference in a dense system into consideration are developed to evaluate the performance of a wireless system with NOMA. The developed framework can be applied to both downlink and uplink scenarios. In addition, the potential of applying simultaneous wireless information and power transfer (SWIPT) in a NOMA system is investigated. All the analytical

results are validated by simulation results.

1.2.3 UDN

In the third generation (3G) cellular networks, the typical density of BSs is about $4-5$ BSs/km^2. In the fourth generation (4G) cellular networks, such as Long Term Evolution-Advanced (LTE-A) mobile communication systems, the typical density of BSs is approximately $8-10$ BSs/km^2. In 5G cellular networks, the density of BSs is anticipated to go up to $40-50$ BSs/km^2, making the future 5G cellular network ultra-dense [18].

UDNs are envisaged as a key technology for 5G cellular systems [1, 18]. Since the distance from transmitters to receivers is greatly reduced in UDNs, signals will be propagated in much shorter distances. Therefore, short-range propagation features need to be considered to generate meaningful and accurate analytical results. As the original PPP based analysis highly relies on the channel model, the system models developed for macro-cell networks are not applicable to UDNs. The short-range propagation features, such as line-of-sight (LoS)/non-line-of-sight (NLoS) propagation and Nakagami fading, make the analysis using stochastic geometry models difficult. In order to evaluate the system-level performance of a UDN, accurate and tractable analytical models are actively pursued and explored. In this dissertation, an analytical model for UDNs is developed based on the dominant BS-based approach in order to address the short-range propagation features of a UDN. Owing to the flexibility of the developed model, it is also applicable to analyze other novel technologies in 5G cellular networks. Although the developed model is constructed based on some reasonable approximations, the numerical simulations prove that it is accurate in a wide range of system settings.

1.3 Dissertation Outline

As mentioned above, the research presented in this dissertation uses stochastic geometry tools to analyze the technologies developed for 5G mobile networks. The main technical contributions of this dissertation are covered in Chapter 2 to Chapter 10.

Chapter 2 to Chapter 4 focus on D2D communication. In Chapter 2, a comprehensive

overview of D2D is provided. The related works and challenges on D2D communication are discussed. Two schemes proposed for underlay D2D, namely FPC + FFR scheme and distance based power control scheme, are presented and analyzed in Chapter 3 and Chapter 4 respectively.

Chapter 5 to Chapter 9 cover the contents on NOMA. In Chapter 5, the concept of NOMA is explained. The existing works on NOMA are reviewed and the motivations of the NOMA research in this dissertation are elaborated. In Chapter 6 and Chapter 7, analytical frameworks are developed for downlink and uplink NOMA separately. In Chapter 8, a unified downlink and uplink NOMA framework is developed. In Chapter 9, the gain of NOMA with SWIPT over OMA in term of harvested energy is investigated.

Chapter 10 covers the contents on UDN. In Chapter 10, a dominant BS-based framework is developed for UDNs. The developed framework incorporates the short-range propagation features of UDN while retains the tractability of PPP. The accuracy of the developed model is validated by simulations.

Finally, Chapter 11 concludes this dissertation by summarizing the key contributions and discussing potential future research directions.

CHAPTER 2

D2D Communication

2.1 Overview

The basic idea of Device-to-device communication (D2D) is illustrated in Fig. 2.1. In a traditional cellular network as shown in Fig. 2.1a, all communications must go through the base station (BS) even if the users intended to communicate are in proximity. Although it works fine for low data rate services such as voice call and text message, this architecture is not spectral and energy efficient, especially when the pair of transmitter and receiver is far away from the BS but close to each other. The basic idea of D2D communication is illustrated in Fig. 2.1b. In contrast with traditional cellular communication, the users in proximity are able to communicate with each other directly bypassing the BS. By leveraging the spatial proximity, D2D communication can improve the spectral efficiency, energy efficiency, delay, and fairness of the network [19].

2.1.1 Taxonomy

D2D communication can be classified into inband D2D and outband D2D based on the spectrum in which D2D communication occurs. Inband D2D uses the licensed cellular spectrum for both D2D and cellular links. In contrast, outband D2D proposes to use unlicensed spectrum such as the industrial, scientific and medical (ISM) band. In addition, both inband D2D and outband D2D can be further classified into some sub-categories depending on other system configurations. The features and some related papers for each category and sub-category of D2D are introduced in the rest of this subsection. In addition, the advantages and disadvantages of each type of D2D are listed.

Inband D2D. As interference in the unlicensed spectrum is uncontrollable, some researchers proposed to implement inband D2D so that the communications in the network

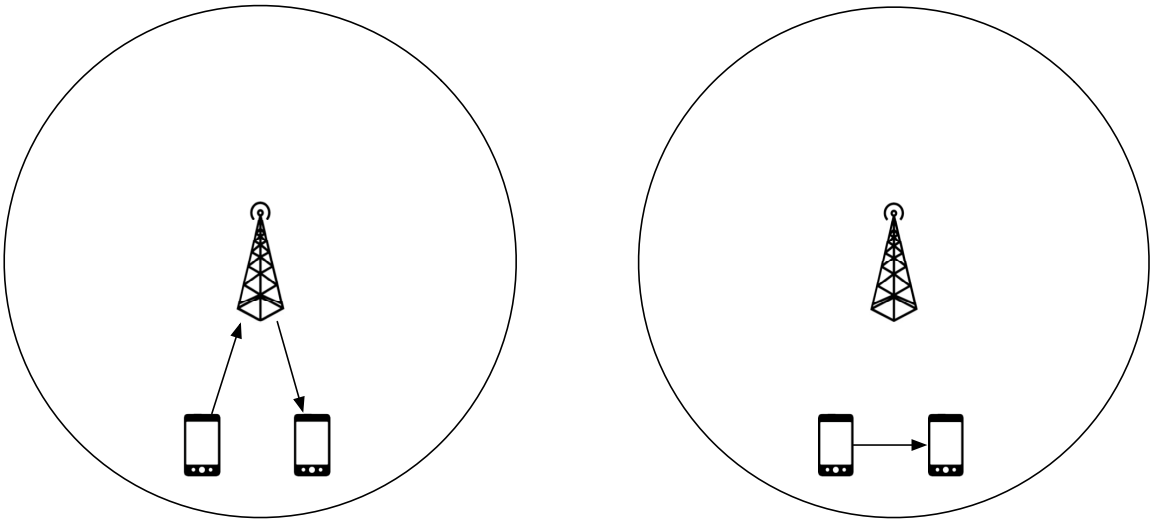

(a) Traditional cellular communication (b) D2D communication

Fig. 2.1: Illustration of D2D communication

can be controlled by a central entity such as BS [19]. Inband D2D can improve the spectrum efficiency of cellular networks by allowing the D2D users and cellular users to share the spectrum resource. Depending on how spectrum resource is shared, inband D2D can be further classified into *underlay inband D2D* and *overlay inband D2D*.

In underlay D2D, D2D users and cellular users use the same spectrum resource simultaneously. The disadvantage of underlay D2D is that D2D users and cellular users generate interference to each other as they are operated on the same spectrum bands. The expected gain of D2D communication may not be achieved if the interference is not well-coordinated [20]. The interference can be mitigated by introducing interference coordination [21], resource allocation [22], or power control [23] schemes. However, these schemes bring extra complexity into the network and hence increase the computational overhead.

To avoid the interference between D2D users and cellular users while retaining the benefit of centralized control, some researchers proposed overlay D2D [24, 25]. In overlay D2D, a portion of the cellular spectrum resources is reversed and dedicated to D2D users. In contrast to underlay D2D, the complexity of overlay D2D is much lower and the concern of interference is eliminated. However, the amount of available resources for cellular users is reduced and the potential gain of applying D2D communication can be low.

Outband D2D. To completely eliminate the potential negative influence on cellular users, outband D2D is proposed [26–28] in which unlicensed spectrum is exploited to support the D2D communication. Outband D2D normally requires user devices to be equipped with another interface operating on the unlicensed band such as WiFi Direct [29], ZigBee [30] or Bluetooth [31], and thus users can have simultaneous D2D and cellular communications. Despite working on the unlicensed band, outband D2D can still be controlled by the cellular network as suggested in [26,27] and such a method is further classified as controlled outband D2D. In contrast to the controlled outband D2D, some researchers suggested to leave D2D in outband autonomous mode [28] and this D2D method is classified as autonomous outband D2D.

2.1.2 Relationship with other paradigms

Although the architecture of D2D communication may look similar to some ad-hoc paradigms such as Mobile Ad-hoc NETworks (MANET) [32] and Cognitive Radio Networks (CRN) [33], the key difference is that D2D is still under the control of a central cellular entity such as a BS. With a central cellular entity, many challenges existing in MANET and CRN, such as white space detection, collision avoidance, and synchronization, do not apply to D2D.

Summary: This section briefly introduced the concept of D2D communication and the categories of D2D in current research. More detail about D2D communication can be found in [12,34] which are comprehensive survey papers. Among all types of D2D communications (underlay inband, overlay inband, controlled outband, and autonomous outband), underlay inband D2D attracts the most research attention and it is also the focus of this dissertation. In the next section, some good papers focus on underlay inband D2D are carefully reviewed.

2.2 Underlay Inband D2D

As of today, the majority of available literature on D2D has been focusing on underlay inband D2D (simply referred as underlay D2D in the rest of this dissertation) due to its advantage of achieving the best spectrum efficiency [34]. However, as mentioned above,

D2D users and cellular users may generate mutual interference as they share the same spectrum resource. Therefore, most of the related work focuses on how to mitigate this mutual interference between D2D and cellular users.

In [35], the authors proposed mode selection for underlay D2D. In this scheme, D2D users have two operation modes, D2D mode, and cellular mode. If two D2D users intending to communicate to each other are in proximity, and their transmissions do not cause harmful interference to the cellular users, they can operate in D2D mode and use the cellular spectrum resources. On the other hand, if the BS detects that D2D users may generate non-negligible interference to other cellular users, D2D users have to communicate in cellular mode. By applying the algorithm developed therein, numerical results show that mode selection can bring significant performance gain to the network without causing notable degradation to cellular users.

In [23], the authors proposed to group each cellular user with a pair of D2D users based on certain criteria. Users within one group share the spectrum resource. For example, D2D user and the cellular user that are far away from each other are grouped together to avoid mutual interference. The resource and power allocation for all the users is formed as an optimization problem and solved by an advanced mathematical method. The Numerical results show that this scheme can significantly improve the performance of the system in terms of D2D access rate and the overall network throughput.

In [36], an interference limited area (ILA) control scheme was proposed for the coexistence of D2D communication and uplink cellular network. ILA is defined as the area in which the interference to signal ratio (ISR) at the D2D receiver is greater than a predetermined threshold. This method does not allow cellular users located in the ILA to use the same resources as D2D users. Despite its simplicity, numerical results show that this method brings a great performance gain and provides good protection to cellular users.

2.3 Motivations

The following issues have not been adequately addressed in the existing literature.

1. The performance of many proposed schemes are only evaluated by simulations. The analytical results are very limited.

2. In most of the existing studies, only single cell scenario is considered while inter-cell interference is completely neglected, which can cause inaccurate performance evaluation in the dense wireless network.

3. Many proposed schemes are overly complicated, which can impose significant computation overhead to the system.

These observations motivate the D2D research study in this dissertation. The goal of the study is to develop tractable yet accurate scheme for underlay D2D communications in a multi-cell scenario. Two schemes are developed and presented in the next two chapters. In Chapter 3, fractional power control and fractional frequency reuse are used to mitigate the interference between D2D users and uplink cellular users. In Chapter 4, a distance-based power control scheme is developed for D2D users in order to control the interference to uplink cellular users. Both schemes consider a multi-cell scenario and are analyzed by using PPP models. Analytical results and simulation results are provided and compared.

CHAPTER 3

D2D Communication Underlay in Uplink Cellular Networks with Fractional Power Control and Fractional Frequency Reuse

3.1 Related Works and Contributions

This chapter presents the first scheme developed for underlay D2D in this dissertation. As mentioned in the last chapter, the key disadvantage of underlay D2D is the interference caused by D2D user equipment (DUE) to the cellular user equipment (CUE) and vice versa. In this chapter, a resource allocation scheme is developed to mitigate this interference. The developed scheme is based on two widely employed schemes in Long Term Evolution (LTE) cellular networks: fractional frequency reuse (FFR) and fractional power control (FPC).

FFR and FPC have been recognized as effective schemes to mitigate inter-cell interference in uplink cellular networks [37]. FFR is mainly used to improve the cell-edge user performance by strategically giving certain spectrum resources to reduce interference for users located in poor signal-to-interference-and-noise-ratio (SINR). In FFR deployments, the reuse factor for the cell-center area is 1 while the reuse factor is typically higher than 1, e.g., equal to 3, at the cell-edge. FPC allows cell-center users with good channel conditions to achieve higher received signal quality than cell-edge users while keeping the cell-edge user experience at acceptable levels.

There are some existing works on D2D communication underlaying an FFR-based cellular network. In [38], a novel radio resource allocation scheme is proposed. In this scheme, DUEs and CUEs use different frequency bands selected based on their locations. The study in [38] focuses on the downlink scenario, and the performance evaluation of the proposed scheme is only based on simulations. [39] provides an analytical study on D2D in a downlink scenario by only allowing D2D communication at the cell-edge to avoid strong interference from BSs. [40] extends the work of [38] to the uplink scenario. The study in [40]

assumes that there is only one D2D pair allowed in one cell, while intercell interference and multiple D2D pairs per cell are not considered.

This chapter proposes a resource allocation scheme for D2D communication underlaying an uplink cellular network. The proposed scheme leverages both FPC and FFR to mitigate the interference between CUEs and DUEs. A multi-cell scenario is considered in this chapter and the PPP model is used to analyze the performance of the system. Compared to the existing works, the study in this chapter provides the mathematical analysis of the proposed scheme which takes inter-cell interference into consideration explicitly.

3.2 System Model

This chapter considers a D2D network underlaying an uplink cellular network. BSs are regularly placed in a hexagonal grid. The area of each cell is denoted as $\frac{1}{\lambda_b}$, where λ_b is the density of BSs on the two-dimensional plane, and each cell is further approximated to a disk with radius $R = \sqrt{\frac{1}{\pi\lambda_b}}$. It is assumed that CUEs are uniformly distributed in each cell, while the distribution of DUEs follows a PPP with density λ_d on the two-dimensional plane. Fractional path-loss inversion is applied for uplink power control, i.e., $P_c = r^{\alpha\epsilon}$, where P_c is the transmit power of a CUE, $\alpha > 2$ is the path-loss exponent and $\epsilon \in (0, 1)$ is the power control parameter. In this model, a DUE represents a pair of UEs which communicate with each other in the D2D mode. A fixed transmit distance d and a fixed transmit power $P_d = d^{\alpha}$ are set for all DUEs. Although the expressions of DUE and CUE powers are normalized for simplicity, they can be conveniently scaled back to their actual values. Rayleigh fading channel is assumed for all links with the fading gain h following an exponential distribution with mean equal to 1. CUEs in each cell are assigned orthogonal resources so there is no intra-cell interference among CUEs. D2D communication is supported in the underlay mode, meaning that DUEs share resources with CUEs without causing excessive interference. To mitigate the interference between DUEs and CUEs, an FFR scheme is applied in which each cell is divided into two areas called the inner cell area and the outer cell area, see Figure 3.1. The ratio of the inner cell area size over the entire cell is denoted as $\beta \in (0, 1)$. DUEs and CUEs in the same inner/outer area are allocated

different spectrum resources to avoid severe interference. For comparison, the performance of both CUEs and DUEs in two models, termed as basic FFR (B-FFR) + FPC model and enhanced FFR (E-FFR) + FPC model, are analyzed.

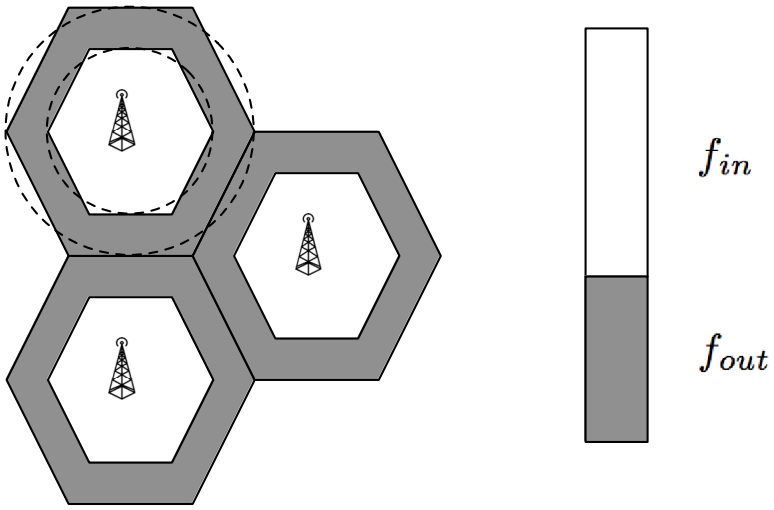

Fig. 3.1: B-FFR + FPC Model

3.2.1 B-FFR + FPC Model

In the B-FFR + FPC model, the total frequency resource is divided into two parts f_{in} and f_{out}. In each cell, CUEs in the inner area can only use f_{in} and CUEs in the outer area can only use f_{out}. The bandwidth allocated to f_{in} and f_{out} is proportional to the area size the areas cover, which means $\frac{f_{in}}{f_{out}} = \frac{\beta}{1-\beta}$. DUEs in the outer area can reuse f_{in} without causing significant interference to CUEs in the inner area since outer cell DUEs are at least $\sqrt{\beta}R$ away from the receiving BSs. On the other hand, inner cell CUEs will not overwhelm outer cell DUEs with interference because the transmit power of inner cell CUEs is quite low due to uplink power control. f_{out} is not used by DUEs at all in this model for the following reasons. If inner cell DUEs reuse f_{out}, they will generate significant interference to outer cell DUEs as inner cell DUEs are close to BS. On the other hand, outer cell CUEs transmit with relatively high power and hence DUEs in the same area will

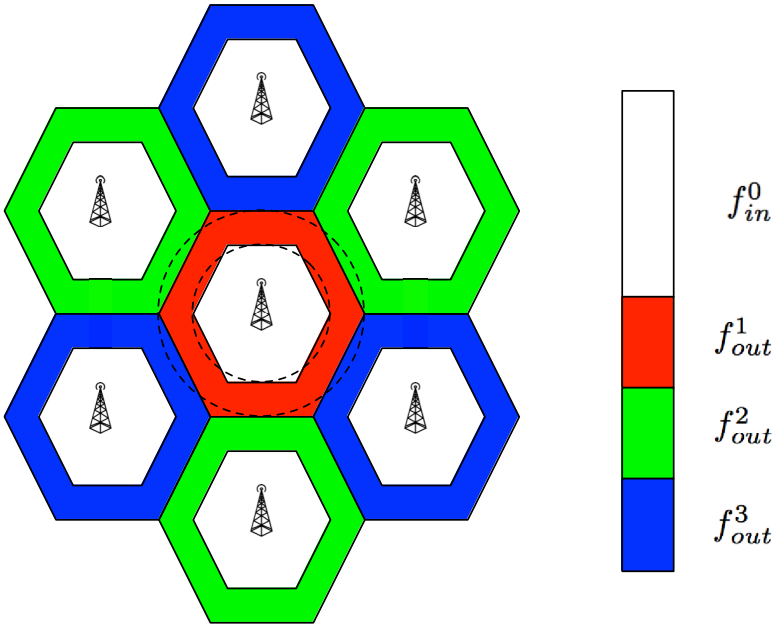

Fig. 3.2: E-FFR + FPC Model

suffer from severe interference. f_{out} is not reused in this model to avoid strong interference to both DUEs and CUEs. FPC is applied to inner cell CUEs to improve the performance of outer cell DUEs. Actually, the SINR distribution of CUEs may not degrade significantly by applying this FPC scheme. Although the received power for the cell center CUEs is reduced, inter-cell co-channel CUE interference is also reduced. The resulting SINR may be still kept at similar levels until the interference from DUEs becomes more significant. This result is more straightforward when there is no D2D communication which will be shown later in the numerical results section of this chapter.

3.2.2 E-FFR + FPC Model

In the B-FFR + FPC Model, f_{out} is not used by DUEs. Also, DUEs are limited to outer cell areas only. To utilize frequency resources more efficiently, the B-FFR scheme is modified to allow DUEs operate in inner cell areas as well [40]. In this scheme, the total spectrum is divided into four parts, namely f_{in}^0, f_{out}^1, f_{out}^2, and f_{out}^3. Furthermore, $f_{out}^1 = f_{out}^2 = f_{out}^3$, $f_{in}^0 + f_{out}^1 + f_{out}^2 + f_{out}^3 = F$, and $\frac{f_{in}^0}{f_{out}^1} = \frac{\beta}{1-\beta}$. F is the total available

frequency band and it is normalized to 1. All inner cell CUEs use f_{in}^0. However, each outer cell CUE can only use one of f_{out}^1, f_{out}^2, and f_{out}^3, as shown in Figure 3.2. f_{in}^0 and f_{out}^1 can be expressed in terms of β as $f_{in}^0 = \frac{\beta}{3-2\beta}$ and $f_{out}^1 = \frac{1-\beta}{3-2\beta}$. In this scheme, outer cell DUEs reuse f_{in}^0 as shown in Figure 3.3, which is the same assumption as for the B-FFR + FPC Model. Inner cell DUEs reuse the frequency resources of neighboring outer cells as shown in Figure 3.4. The closest interfering DUEs to an outer cell CUE come from the neighboring inner cell while only $\frac{1}{3}$ of the total neighboring outer cell CUEs interfere with inner cell DUEs. Therefore, in this scheme DUEs can be supported in both inner and outer cell areas. The same FPC scheme is also applied as for the B-FFR + FPC model so that system performance can be further improved.

3.3 Coverage Study

In this section, the coverage probability of both CUEs and DUEs are derived. The coverage probability is defined as the possibility that the SINR of a randomly chosen DUE or CUE is above a certain threshold T ($\mathbb{P}[SINR > T]$). A full load scenario is assumed, i.e., all resources are occupied all the time. Without loss of generality, the coverage study focuses on a single resource by assuming wideband flat fading for all UEs in the network.

3.3.1 Coverage in the B-FFR + FPC Model

The analysis starts with deriving the coverage probability for inner cell CUEs. The interference to an inner cell CUE comes from co-channel CUEs in other inner cells and co-channel outer cell DUEs. The SINR of an inner cell CUE can be expressed as

$$SINR_c^{in} = \frac{hP_c^{in} r_{in}^{-\alpha}}{I_c^{in} + I_d^{out} + \sigma^2} = \frac{h r_{in}^{(\epsilon-1)\alpha}}{I_c^{in} + I_d^{out} + \sigma^2},$$

where σ^2 denotes the noise power, r_{in} is the distance between the CUE and the BS, I_c^{in} denotes the interference from co-channel CUEs in other inner cells, and I_d^{out} denotes the interference from co-channel outer cell DUEs. Note that at the right-hand side of the above

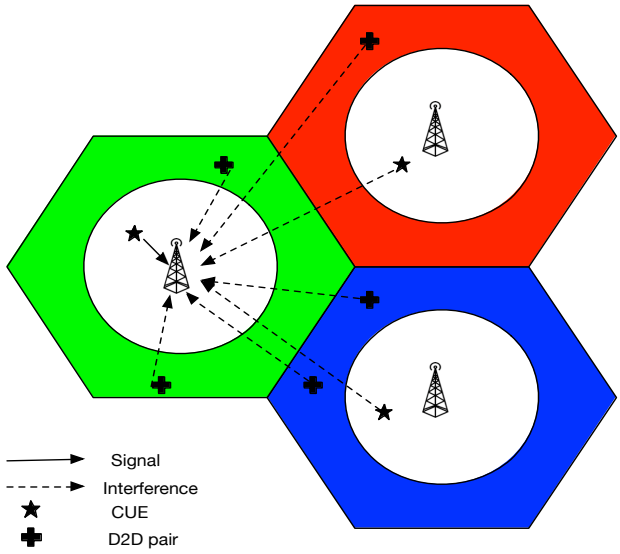

(a) Analysis for inner cell CUE.

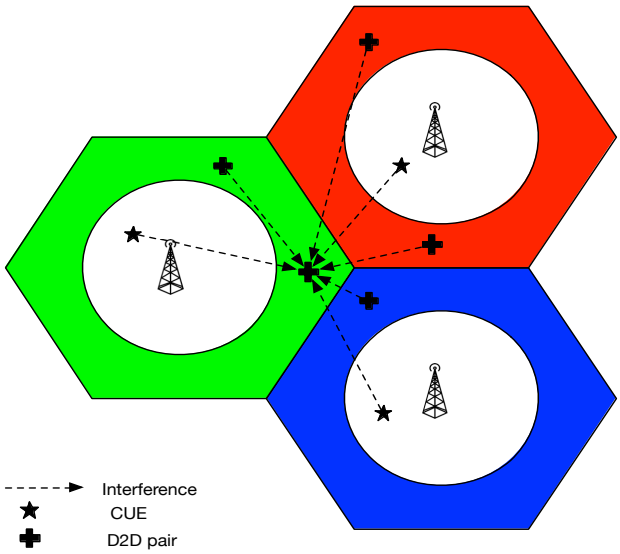

(b) Analysis for outer cell DUE.

Fig. 3.3: DUEs in outer areas and CUEs in inner areas.

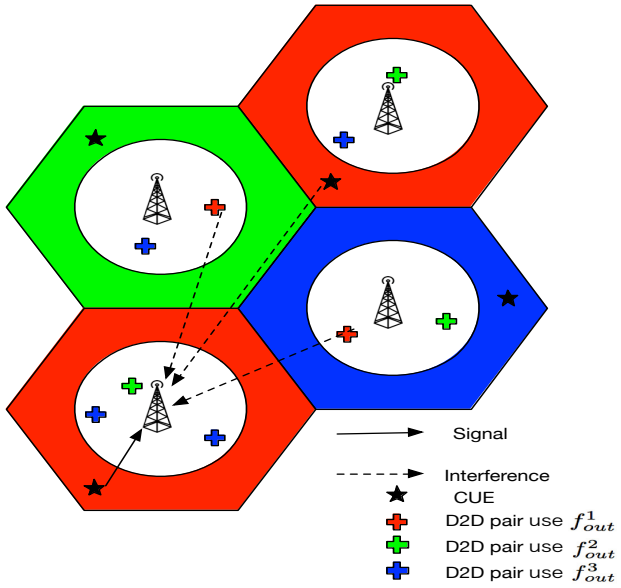

(a) Analysis for outer cell CUE.

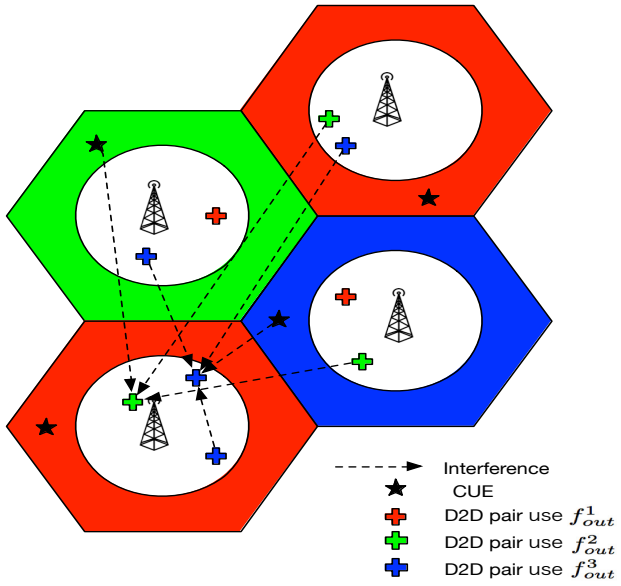

(b) Analysis for inner cell DUE.

Fig. 3.4: DUEs in inner areas and CUEs in outer areas.

equation the transmission power of the inner cell CUE is replaced by $P_c = r^{\epsilon\alpha}$ as FPC is applied. By following a similar approach as the one presented in [41, 42], one can obtain the coverage probability of an inner cell CUE as

$$\mathbb{P}[SINR_c^{in} > T] = \int_0^{\sqrt{\beta}R} \mathbb{P}[SINR_c^{in} > T | r_{in}] f_{r_{in}}(r_{in}) dr_{in}, \tag{3.1}$$

$$\mathbb{P}[SINR_c^{in} > T | r_{in}] = \mathcal{L}_{I_c^{in}}(T r_{in}^{(1-\epsilon)\alpha}) \mathcal{L}_{I_d^{out}}(T r_{in}^{(1-\epsilon)\alpha}) e^{-T r_{in}^{(1-\epsilon)\alpha} \sigma^2}, \tag{3.2}$$

$$f_{r_{in}}(x) = \frac{1}{\beta} 2\pi\lambda_b x, x \in [0, \sqrt{\frac{\beta}{\pi\lambda_b}}], \tag{3.3}$$

$$\mathcal{L}_{I_c^{in}}(S) \approx \exp\Big(- 2\pi\lambda_b S \mathbb{E}[P_c^{in}] \frac{(R(2-\sqrt{\beta}))^{2-\alpha}}{\alpha - 2}\Big), \tag{3.4}$$

$$\mathbb{E}[P_c^{in}] = \int_0^{\sqrt{\frac{\beta}{\pi\lambda_b}}} \frac{1}{\beta} 2\pi\lambda_b x \cdot x^{\epsilon\alpha} dx = \frac{\beta^{\frac{\epsilon\alpha}{2}} R^{\epsilon\alpha+2}, 2\pi\lambda_b}{\epsilon\alpha + 2}, \tag{3.5}$$

$$\mathcal{L}_{I_d^{out}}(S) \approx \exp\Big(- \pi\lambda_d (SP_d)^{\frac{2}{\alpha}} \int_{\frac{\beta}{(SP_d)^{\frac{2}{\alpha}} \pi\lambda_b}}^{\infty} \frac{1}{1 + x^{\frac{\alpha}{2}}} dx\Big), \tag{3.6}$$

where $\mathcal{L}_{I_c^{in}}(s)$ and $\mathcal{L}_{I_d^{out}}(s)$ are the Laplace transformers of random variables I_c^{in} and I_d^{out}, respectively, evaluated at point s, and $f_{r_i}(x)$ is the PDF of the distance between an inner cell CUE and its serving BS. The exact expression of (3.2) is difficult to derive and hence some approximations are adopted in (3.4) and (3.6) to obtain succinct results. In (3.4), the distribution of all interfering CUEs is approximated as a PPP with density λ_b, although they are actually uniformly distributed in each cell. This assumption is proven in [11] for a generic uplink cellular network and is also numerically validated in [42]. In (3.6), it is assumed that the interfering DUEs are distributed over all areas outside the typical inner cell area, though in fact they are only located in the outer area of each cell. This approximation can be justified as follow. When focusing on the outer cell area of the typical cell and its first-tier neighboring cells, within which DUEs contribute the majority interference, the assumption is consistent with the actual case. Hence, the slight overestimation of the DUE interference assumed here does not crucially impact the accuracy of the coverage study. Note that the assumptions described above are also applied to the rest of the analysis in

this chapter.

For outer cell DUEs which reuse f_{in} with inner cell CUEs, interference comes from all outer cell DUEs and inner cell CUEs. The SINR of an outer cell DUE can be expressed as

$$SINR_d^{out} = \frac{hP_d d^{-\alpha}}{I_c^{in} + I_d^{out} + \sigma^2}. \tag{3.7}$$

By using the approach presented in [42], the coverage probability is calculated as

$$\mathbb{P}[SINR_d^{out} > T] = \mathcal{L}_{I_c^{in}}\Big(\frac{Td^{\alpha}}{P_d}\Big)\mathcal{L}_{I_d^{out}}\Big(\frac{Td^{\alpha}}{P_d}\Big)e^{-\frac{Td^{\alpha}}{P_d}\sigma^2}, \tag{3.8}$$

$$\mathcal{L}_{I_c^{in}}\Big(\frac{Td^{\alpha}}{P_d}\Big) = \exp\Big(-\frac{\pi\lambda_b}{sinc(\frac{2}{\alpha})}\mathbb{E}[(P_c^{in})^{\frac{2}{\alpha}}]\Big(\frac{Td^{\alpha}}{P_d}\Big)^{\frac{2}{\alpha}}\Big), \tag{3.9}$$

$$\mathbb{E}[(P_c^{in})^{\frac{2}{\alpha}}] = \int_0^{\sqrt{\frac{\beta}{\pi\lambda_b}}} \frac{2}{\beta}\pi\lambda_b x \cdot (x^{\epsilon\alpha})^{\frac{2}{\alpha}} dx = \frac{\pi\lambda_b\beta^{\epsilon}R^{2\epsilon+2}}{\epsilon+1}, \tag{3.10}$$

$$\mathcal{L}_{I_d^{out}}\Big(\frac{Td^{\alpha}}{P_d}\Big) = \exp\Big(-\frac{\pi\lambda_d}{sinc(\frac{2}{\alpha})}\mathbb{E}[P_d^{\frac{2}{\alpha}}]\Big(\frac{Td^{\alpha}}{P_d}\Big)^{\frac{2}{\alpha}}\Big). \tag{3.11}$$

Since the outer cell CUEs in this model do not share frequency resources with DUEs, FPC is not applied, i.e., $\epsilon = 1$. By following a similar approach as above, the SINR and coverage probability of an outer cell CUE are given as

$$SINR_c^{out} = \frac{hP_c r_{out}^{-\alpha}}{I_c^{in} + \sigma^2} = \frac{h}{I_c^{in} + \sigma^2}, \tag{3.12}$$

$$\mathbb{P}[SINR_c^{out} > T] = \mathcal{L}_{I_c^{out}}(T)e^{-T\sigma^2}, \tag{3.13}$$

$$\mathcal{L}_{I_c^{out}}(S) = \exp\Big(-2\pi\lambda_b S\mathbb{E}[P_c^{out}]\frac{1}{\alpha-2}R^{2-\alpha}\Big), \tag{3.14}$$

$$\mathbb{E}[P_c^{out}] = \int_{\sqrt{\frac{\beta}{\pi\lambda_b}}}^{\sqrt{\frac{1}{\pi\lambda_b}}} f_r^{out}(x)x^{\alpha}dx = \frac{(1-\beta^{\frac{\alpha}{2}+1})}{(\frac{\alpha}{2}+1)(\pi\lambda_b)^{\frac{\alpha}{2}}(1-\beta)}, \tag{3.15}$$

$$f_r^{out}(x) = \frac{2\pi\lambda_b x}{1-\beta}, \quad x \in [\sqrt{\frac{\beta}{\pi\lambda_b}}, \sqrt{\frac{1}{\pi\lambda_b}}]. \tag{3.16}$$

3.3.2 Coverage in the E-FFR + FPC Model

In the B-FFR + FPC model analyzed in Section 3.3.1, f_{out} is not reused by DUEs to avoid strong interference to both CUEs and DUEs. The disadvantage of this model is that it may not be able to fully exploit all available frequency resources. Besides, DUEs are constrained to outer cell areas under the B-FFR + FPC model. Whereas in reality, D2D communication could be desirable anywhere in the cell. To address these issues, E-FFR + FPC model is proposed. f_{out} is equally partitioned into k portions, namely $f_{out}^1, f_{out}^2, ..., f_{out}^k$, where k is the reuse factor, which is assumed to be equal to 3 in this study. CUEs in the outer area of each cell use a frequency portion which is different from the one used by its neighboring outer cells as shown in Figure 3.4(a). In this case, the closest interfering CUE to the target cellular link is $(\sqrt{3k}-1)R$ away from the target BS. This distance is quite larger than that of the B-FFR + FPC model which is R. Also, the number of interfering CUEs is $\frac{1}{k}$ of the number in the B-FFR + FPC model, hence intercell interference is effectively mitigated. Inner cell DUEs are allowed to reuse frequency resources with CUEs in their neighboring cell as shown in Figure 3.4(b). In this case, the closest interfering DUE to the target BS is $(2-\sqrt{\beta})R$. As DUEs typically transmit with lower power and are placed at a relatively large distance from co-channel CUEs, they are not expected to generate significant interference to cellular communications. The closest interfering CUE to an inner cell DUE is $(1-\sqrt{\beta})R$. Although this isolation can alleviate interference to DUEs, the potential benefit does not seem to be obvious and is therefore neglected during the analysis. The improvement to the performance of DUEs in this model mainly comes from the fact that only CUEs in $\frac{1}{k}$ cells will cause interference. Also, the number of interfering DUEs is $\frac{k-1}{k}$ of that in the B-FFR + FPC model, which is expected to only slightly affect the final result and therefore is neglected as well.

Note that the coverage analysis for inner CUEs and outer cell DUEs is the same as that in the B-FFR + FPC model. There are differences only for outer cell CUEs and inner cell DUEs. Following the same approach as in Section 3.3.1, the equations for the SINR and coverage probability of a typical outer cell CUE are given by:

$$SINR_c^{out} = \frac{P_c^{out} r_{out}^{-\alpha} h}{I_c^{out} + I_d^{in} + \sigma^2} = \frac{h}{I_c^{out} + I_d^{in} + \sigma^2}, \tag{3.17}$$

$$\mathbb{P}[SINR_c^{out} > T] = \mathcal{L}_{I_c^{out}}(T)\mathcal{L}_{I_d^{in}}(T)e^{-T\sigma^2}, \tag{3.18}$$

$$\mathcal{L}_{I_c^{out}}(S) = \exp\Big(- 2\pi\frac{\lambda_b}{k} S\mathbb{E}[P_c^{out}]\frac{1}{\alpha - 2}(\sqrt{3k}R - R)^{2-\alpha}\Big), \tag{3.19}$$

$$\mathbb{E}[P_c^{out}] = \int_{\sqrt{\frac{\beta}{\pi\lambda_b}}}^{\sqrt{\frac{1}{\pi\lambda_b}}} f_r^{out}(x)x^{\alpha}dx = \frac{(1 - \beta^{\frac{\alpha}{2}+1})}{(\frac{\alpha}{2}+1)(\pi\lambda_b)^{\frac{\alpha}{2}}(1-\beta)}, \tag{3.20}$$

$$\mathcal{L}_{I_d^{in}}(S) = \exp\Big(- 2\pi\lambda_d S P_d \frac{1}{\alpha - 2}\big((2 - \sqrt{\beta})R\big)^{2-\alpha}\Big). \tag{3.21}$$

The corresponding equations for the SINR and coverage probability of inner cell DUEs are given by:

$$SINR_d^{in} = \frac{P_d d^{-\alpha} h}{I_c^{out} + I_d^{in} + \sigma^2}, \tag{3.22}$$

$$\mathbb{P}[SINR_d^{in} > T] = \mathcal{L}_{I_c^{out}}\Big(\frac{Td^{\alpha}}{P_d}\Big)\mathcal{L}_{I_d^{in}}\Big(\frac{Td^{\alpha}}{P_d}\Big)e^{-\frac{Td^{\alpha}}{P_d}\sigma^2}, \tag{3.23}$$

$$\mathcal{L}_{I_c^{out}}(S) \approx \exp\Big(- \frac{\pi\frac{\lambda_b}{k}}{sinc(\frac{2}{\alpha})}\mathbb{E}[(P_c^{out})^{\frac{2}{\alpha}}]S^{\frac{2}{\alpha}}\Big), \tag{3.24}$$

$$\mathbb{E}[(P_c^{out})^{\frac{2}{\alpha}}] = \int_{\sqrt{\frac{\beta}{\pi\lambda_b}}}^{\sqrt{\frac{1}{\pi\lambda_b}}} f_r^{out}(x)\cdot(x^{\alpha})^{\frac{2}{\alpha}}dx = \frac{1+\beta}{2\pi\lambda_b}. \tag{3.25}$$

3.4 Numerical Evaluation

In this section, the numerical results for the E-FFR + FPC model are presented at first. Then, the performance of the B-FFR + FPC and E-FFR + FPC models are compared. The first study is essentially a sensitivity study for ϵ. Intuitively, a smaller value of ϵ is expected to degrade the performance of inner cell CUEs since the transmit power decreases. However, due to the decrease of the intercell interference, the resulting SINR may actually increase. The SINR distributions of inner cell CUEs with and without underlaying DUEs are shown in Figure 3.5. From Figure 3.5, if there are no underlaying DUEs, the SINR distribution of CUEs is actually better with smaller ϵ. Also one can see from Figure 3.5 that a slight decrease of ϵ does not cause significant degradation to CUEs and this behavior

brings remarkable improvement to outer cell DUEs as shown in Figure 3.6. A very small value for ϵ will ultimately severely impact the performance of CUEs, while the benefit to DUEs by further decreasing the CUE transmit power is limited given the dominant interference from DUEs in this case.

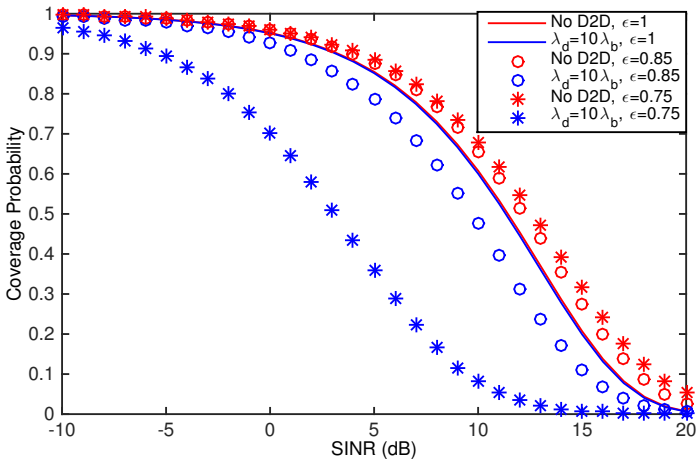

Fig. 3.5: SINR distribution of inner cell CUEs.

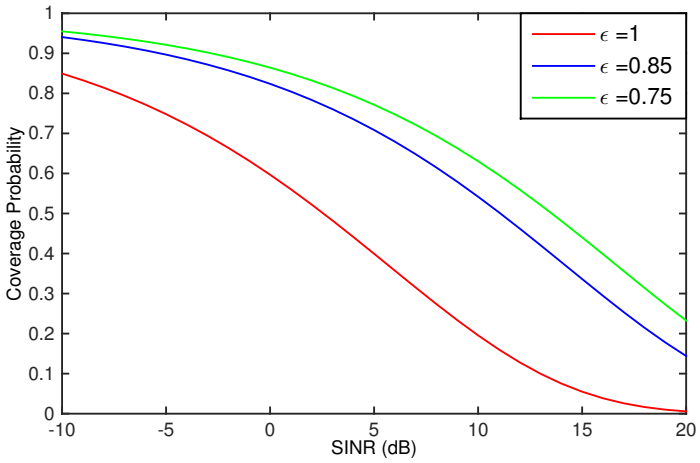

Fig. 3.6: SINR distribution of outer cell DUEs.

In the B-FFR + FPC model, each cell can access the entire frequency resource, while in the E-FFR + FPC model each cell can only access $\frac{1}{3-2\beta}$ of the total bandwidth. Therefore, a larger β means more available spectrum resource per cell. However, a larger β also raises the average power of CUEs in both inner and outer cell areas, which results in a worse interference environment based on the analytical results of the paper. The overall coverage probability of CUEs and DUEs, i.e., $\mathbb{P}[SINR_c > T]$ and $\mathbb{P}[SINR_d > T]$, can be obtained by combining their respective coverage probability in the inner and outer cell areas:

$$\mathbb{P}[SINR_c > T] = \beta\mathbb{P}[SINR_c^{in} > T] + (1-\beta)\mathbb{P}[SINR_c^{out} > T], \tag{3.26}$$

$$\tag{3.27}$$

$$\mathbb{P}[SINR_d > T] = \frac{2\beta}{1+\beta}\mathbb{P}[SINR_d^{in} > T] + \frac{(1-\beta)}{1+\beta}\mathbb{P}[SINR_d^{out} > T]. \tag{3.28}$$

Figure 3.7 shows that the coverage performance is degraded for both CUEs and DUEs if β increases. Even though the SINR distribution degrades, the overall throughput in a cell may still increase due to the fact that more frequency resources are available per cell when β increases.

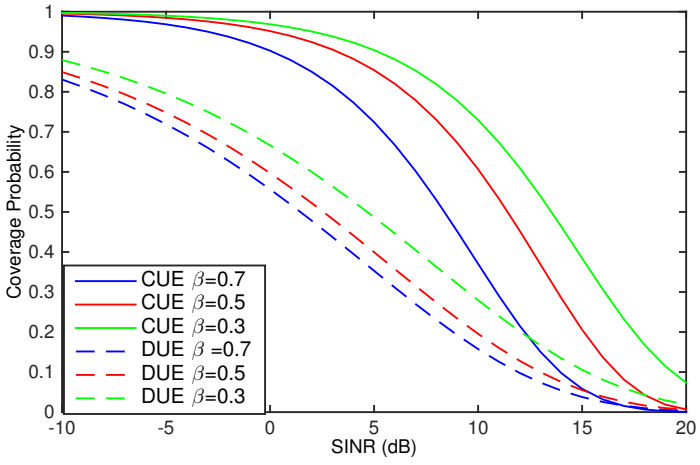

Fig. 3.7: Overall SINR distribution of CUEs and DUEs.

Figure 3.8 shows that the normalized per cell throughput of CUEs decreases as ϵ decreases. In an LTE network with no underlaying DUEs, a smaller value for ϵ tends to increase the total throughput. However, in a D2D underlay network, the interference from DUEs remains unchanged when the value of ϵ changes. Thus, the DUE interference becomes relatively stronger as the CUE transmit power decreases with smaller values of ϵ. One can see that there exists an optimal value of β for some values of ϵ. Also, there is a trade-off between the performance of CUEs and available resources for different β values. Finally, for some values of ϵ the influence of β is monotonic, i.e., the increase of β value monotonically decreases the normalized per cell throughput of CUEs.

From Figure 3.9, the normalized per cell throughput of DUEs keeps decreasing as β increases if no FPC is applied. Although DUEs can access more bandwidth in each cell for a larger β, this benefit is offset by the interference from CUEs if there is no FPC. However, the improvement of the DUE performance is remarkable if slightly lower the transmit power for inner cell CUEs by using FPC, e.g., $\epsilon = 0.8$. Also one can see an excessive reduction of the CUE power, e.g., $\epsilon = 0.5$ will significantly hurt the CUE performance while the performance gain for DUEs is only marginal.

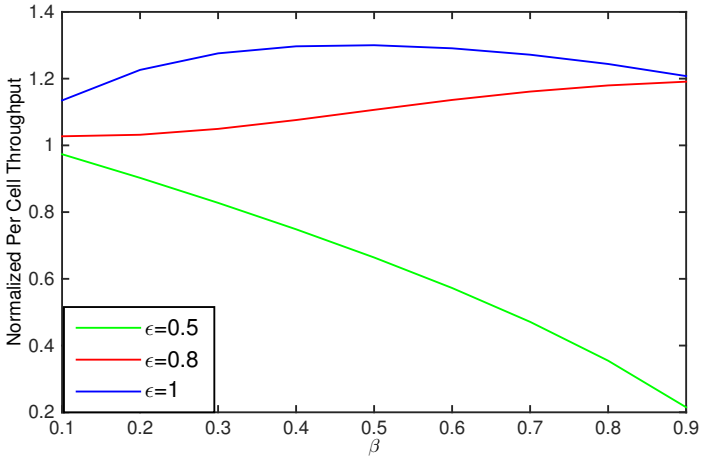

Fig. 3.8: Normalized Per Cell Throughput of CUEs

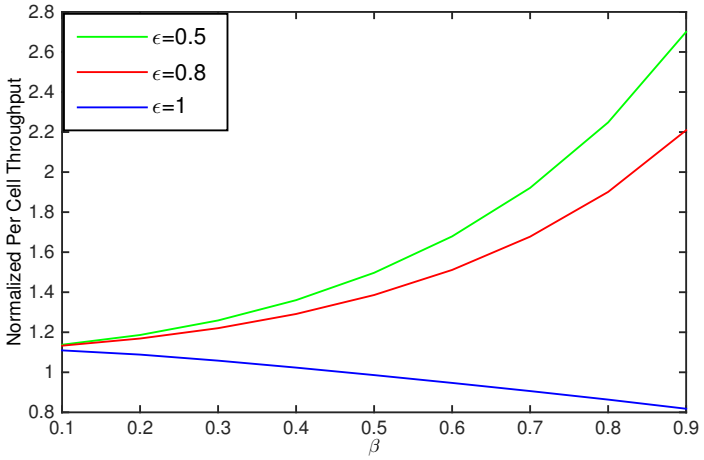

Fig. 3.9: Normalized Per Cell Throughput of DUEs

Figure 3.10 compares the normalized per cell throughput of CUEs and DUEs in the B-FFR + FPC and E-FFR + FPC models. Figure 3.10 shows that the normalized per cell throughput of CUEs in the B-FFR + FPC model always outperforms that in the E-FFR + FPC model. This is because CUEs can access more bandwidth in the B-FFR + FPC. Although the SINR distribution of outer cell CUEs in the E-FFR + FPC model is better, this improvement cannot counteract the decrease of frequency resource usage. The normalized per cell throughput of DUEs in the E-FFR + FPC is higher than that in the B-FFR + FPC model when $\beta \leq 0.5$. After that point, it is slightly worse than that in the B-FFR + FPC. As β increases, the resource gap between the B-FFR + FPC model and the E-FFR + FPC model reduces and, thus, the overall SINR distribution degrades in the E-FFR + FPC model as shown in Figure 3.11. From these comparisons, one can conclude that the B-FFR + FPC model can provide better service for CUEs, while the E-FFR + FPC model is more beneficial for DUEs. Therefore, the final model selection depends on the specific system design goals, e.g., CUE throughput requirements, as well as system deployment configurations such as the density of DUEs.

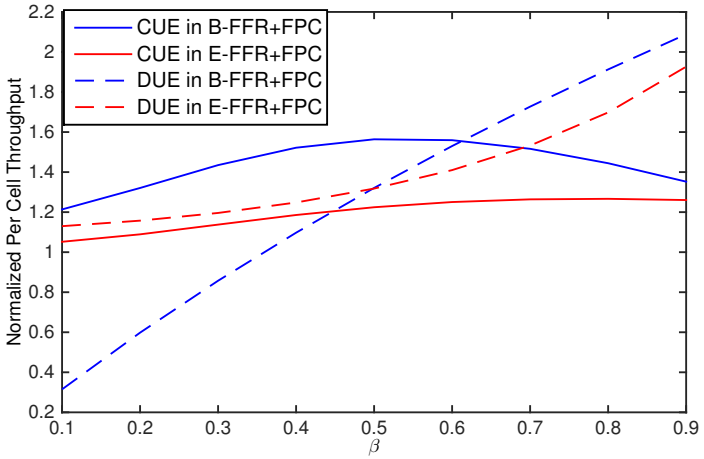

Fig. 3.10: B-FFR + FPC vs. E-FFR + FPC, $\epsilon = 0.85$.

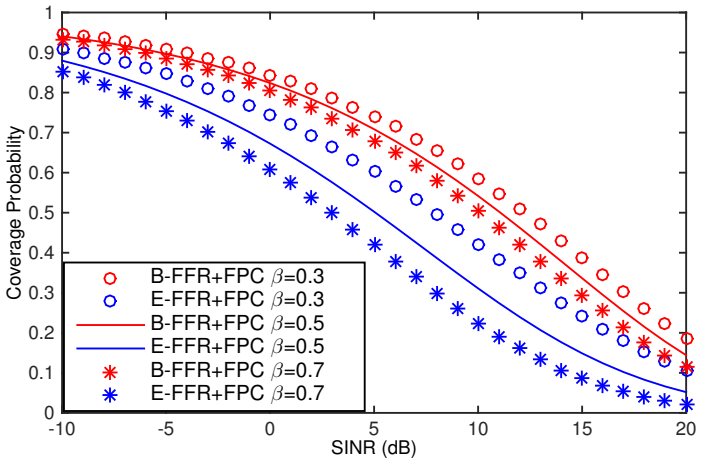

Fig. 3.11: Coverage Probability of DUE in B-FFR + FPC and E-FFR + FPC, $\epsilon = 0.85$.

3.5 Conclusion

This chapter analyzes the performance of both DUEs and CUEs in a D2D underlay cellular network employing FFR and FPC. By using a PPP model to model the UE distributions in the network, the coverage probabilities are derived, and a numerical study of the impact of key system design parameters on the throughput performance is provided. The content in this section contains the preliminary results of the application of FFR and FPC in a cellular network supporting underlay D2D communications. More advanced resource allocation and power control schemes can be further developed based on this work.

CHAPTER 4

Underlay D2D Communication in Uplink Cellular Networks with Distance-Based Power Control

Although embedding D2D communication into an existing cellular system possesses many potential gains mentioned in previous context, it also introduces new problems that must be solved properly to acquire the expected gains. In a cellular network with underlaid D2D communications, DUEs share frequency resources with CUEs and inevitably generate interference to cellular links. Therefore interference management techniques must be applied to coordinate the resource sharing among CUEs and DUEs. In this chapter, a distance-based power control scheme is developed for underlay D2D communication in uplink cellular network. The proposed scheme is analyzed by using PPP model. The analytical results are validated by simulations.

4.1 Related Works and Contributions

As a key technique to tackle the interference between CUEs and DUEs, power control has attracted considerable attention and has already been considered in many works. In [43] a simple transmit power reduction method is proposed for DUEs in a single cell scenario to control the influence from DUEs to CUEs. A dynamic power control mechanism is proposed in [44], which adjusts the transmit power of a DUE to exclude the co-channel CUEs out of its coverage area. In [45], authors analyzed optimal power control between cellular and D2D users and derived a closed form solution for most of the considered scenarios.

Although a lot of research has been made on the power control scheme for D2D communication, most of them are based on a grid system model, which is not a desirable tool for analytical study. To the best of our knowledge, [46] is the only one to focus on D2D power control by using the stochastic geometry method. Authors in [46] proposed two power control algorithms, namely centralized and distributed power control. Normally a

centralized power control algorithm in a D2D supported cellular network can effectively control interference generated by co-channel DUEs at the cost of a high channel feedback overhead. A distributed power control algorithm, on the other hand, only uses limited or local channel information and may not provide the same effective interference mitigation as in the centralized scheme.

In this dissertation, a distributed distance-based power control scheme for D2D communication is proposed. The DUE transmit power is decided based only on the distance information between itself and the associated BS, and hence an excessive signaling overhead can be avoided. A multi-cell uplink cellular system is considered in this chapter and modeled by a PPP. After applying some reasonable assumptions and approximations, analytical results can be expressed in succinct yet effective forms.

The rest of this chapter is organized as follows. In Section 4.2 the system model is described and the proposed power control scheme is introduced. In Section 4.3, the coverage probability for CUEs and DUEs are derived respectively. In Section 4.4, the performance results from both analysis and simulations are presented. Finally conclusions are drawn in Section 4.5.

4.2 System Model and Powew Control Scheme

4.2.1 System Model

In this chapter, a multi-cell uplink cellular network with underlaid D2D communication is considered, as shown in Figure 4.1. BSs are placed in a hexagon regular grid. The area of each cell is denoted as $\frac{1}{\lambda_b}$, where λ_b is the BS density in the 2-D plane. To simplify the expression, during analysis each cell is approximated to a disk with radius $R = \sqrt{\frac{1}{\pi\lambda_b}}$.

The system uses frequency reuse 1, meaning the same radio resources are used among all the cells. The radio resources are partitioned into a number of sub-bands and resources are allocated in the unit of sub-band. For notational simplicity, the bandwidth of each sub-band is normalized to 1. The analysis of performance focuses on a typical sub-band by assuming flat fading channels across sub-bands. There are two types of users in the system,

DUEs and CUEs. In the proposed scheme, the spectrum resource of one CUE is allowed to be shared with multiple DUEs in each cell and hence they generate interference to each other. There is no intra-cell interference for CUEs as orthogonal radio access scheme is assumed for CUEs in each cell while resources are reused among different cells. A heavy load scenario is assumed, which means there is one CUE on each sub-band for all BSs at any given time. Based on these assumptions, on a certain sub-band, each cell has one CUE and multiple DUEs, which all share the same normalized bandwidth. Without loss of generality, the analysis presented in this chapter is for a typical receiver (DUE receiver for D2D link or BS for cellular link) located at the origin of the plane operating on a typical sub-band, as the statistics seen from a PPP is independent of the test location according to Slivnyak-Mecke theorem [47, Ch. 2.5].

On the typical sub-band under analysis, the CUEs are uniformly distributed in each cell. In the model of this chapter, a DUE actually represents a pre-assigned D2D pair, in which two devices in the same cell communicate to each other in the D2D mode. The communication distance d between two D2D users forming a pair is fixed at a small value, e.g., 25 meters. The locations of all DUEs operating on the typical sub-band is assumed to follow a 2-D homogeneous PPP distribution with a density λ_d, $\lambda_d \geq \lambda_b$.

Wireless channel consists of path-loss and Rayleigh fading, the gain of which follows an exponential distribution with mean 1. Path-loss inversion is used for uplink power control. Denoted as r the distance from a typical CUE to its associated BS, the uplink transmit power can be expressed as $P_c = r^\alpha$, where $\alpha > 2$ is path-loss exponent and the PDF of r is $f_r(r) = \frac{2r}{R^2}$, $r \in (0, R)$.

4.2.2 Distance-based Power Control Scheme for D2D

The proposed power control scheme is elaborated in this sub-section. Assume the distance from a DUE to its associated BS is D and the transmit power of that DUE under distance based power control is $P_d = \eta D^\alpha$, where η is a control parameter with a small value so that the tagged DUE will not cause excessive interference to CUEs and to other DUEs in the same cell. Under this power control scheme, DUEs closer to the BS can only transmit

at a lower power to avoid causing significant interference to uplink CUEs. DUEs at cell edge can transmit at a higher power as their interference to uplink CUEs is diminished due to path-loss. Owing to distance based power control, the average interference to a CUE is the same among all the DUEs in the same cell. For the analytical purpose, the transmit power for both CUEs and DUEs are normalized. Their normalized powers can be scaled back to the real power values conveniently without affecting the analytical results.

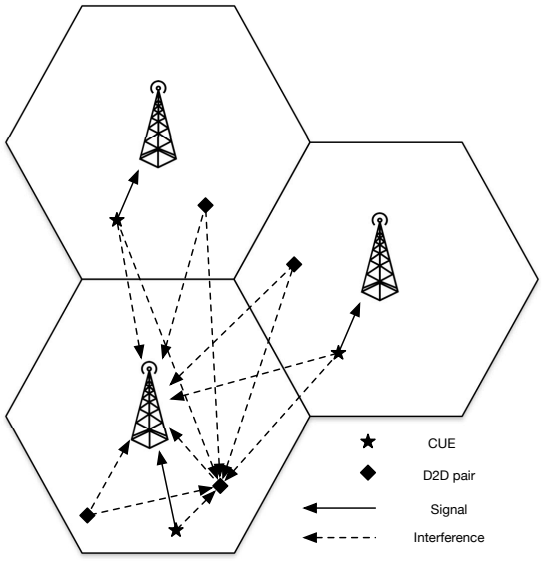

Fig. 4.1: System model considering the cell at bottom as typical cell and one D2D pair inside as the typical one

4.3 Coverage Probability

In this section coverage probabilities for both CUEs and DUEs are analyzed. Recall that the coverage probability, which can be expressed as $\mathbb{P}[SINR > T]$, is the complementary cumulative distribution function (CCDF) of SINR over the entire network and represents the probability that the instantaneous SINR of a randomly chosen CUE or DUE is greater than a certain threshold T. As a fully loaded scenario is considered, the typical sub-band is always occupied by one CUE and multiple DUEs in each cell. Thus CUE density is always equal to the BS density λ_b. Hereafter, λ_b is simply used to represent the CUE

density as well.

4.3.1 CUE Coverage Probability

In the system model described in Figure 4.1, the interference to a typical CUE consists of two parts, i.e., interference from CUEs in other cells denoted as I_c^{out}, and interference from all the DUEs in the system denoted as I_d. I_c^{out} can be evaluated by using the same method in [41]. The locations of CUEs in all other cells are assumed to form a 2-D homogeneous PPP with a density λ_b and their distances to their respective associated BSs are i.i.d. With this assumption, the analytical results derived here are approximations but with high accuracy. This will be validated by simulations in the next section. To analyze I_d, the interfering DUEs are further partitioned into two groups, i.e., same cell DUEs, or S-DUEs, and other cell DUEs, or O-DUEs. The interference distributions of S-DUEs and O-DUEs are analyzed separately. The location distribution and transmit power distribution for S-DUEs can be derived accurately, based on which their interference can be calculated. For O-DUEs, their transmit powers are assumed to be i.i.d. In reality, they do not cause much interference in this case as they are in other cells and they transmit with low power. By summarizing the above statements, the coverage probability of the typical CUE can be expressed in a neat form, presenting a desirable theoretical platform for analysis.

The SINR expression of the typical uplink CUE is

$$SINR_c = \frac{hr^{-\alpha}P_c}{\delta^2 + I_c^{out} + I_d^{in} + I_d^{out}}. \tag{4.1}$$

h represents the Rayleigh fading gain of the desired signal and it follows the exponential distribution with mean 1. I_d^{in}, and I_d^{out} denote the interference from DUEs in the typical cell and interference from DUEs outside the typical cell, respectively. δ^2 is the noise power.

The coverage probability can thus be expressed as

$$\begin{aligned}\mathbb{P}[\text{SINR}_c > T] &= \mathbb{P}[\frac{hr^{-\alpha}P_c}{\delta^2 + I_c^{out} + I_d^{in} + I_d^{out}} > T] \\ &= \mathbb{P}[h > T(\delta^2 + I_c^{out} + I_d^{in} + I_d^{out})] \\ &= \mathcal{L}_{I_c^{out}}(T)\mathcal{L}_{I_d^{in}}(T)\mathcal{L}_{I_d^{out}}(T)\exp(-\delta^2 T) \\ &\approx \mathcal{L}_{I_c^{out}}(T)\mathcal{L}_{I_d^{in}}(T)\mathcal{L}_{I_d^{out}}(T). \end{aligned} \tag{4.2}$$

The second equal sign satisfies due to $P_c = r^{\alpha}$. The third equal sign is obtained by using $h \sim \exp(1)$. Noise is neglected in the last approximation as the considered system is interference limited. $\mathcal{L}_{I_c^{out}}(S)$, $\mathcal{L}_{I_d^{in}}(S)$, and $\mathcal{L}_{I_d^{out}}(S)$ are the Laplace transforms of random variables I_c^{out}, I_d^{in}, and I_d^{out}, respectively, all evaluated at S. The derivation of $\mathcal{L}_{I_c^{out}}(S)$ is provided at first, which corresponds to the interference from CUEs in other cells. By following the same derivation given in [11], one can get

$$\begin{aligned}\mathcal{L}_{I_c^{out}}(S) &= \exp\Big(-2\pi\lambda_b \int_R^{\infty} \big(1 - \mathbb{E}_{P_c,g}[\exp(-SgP_c v^{-\alpha})]\big) v dv\Big) \\ &= \exp\Big(-2\pi\lambda_b \int_R^{\infty} \big(1 - \mathbb{E}_{P_c}[\frac{1}{1+SP_c v^{-\alpha}}]\big) v dv\Big). \end{aligned} \tag{4.3}$$

The second equal sign is true based on $g \sim \exp(1)$, where g is the channel gain of each interfering link. Using Jensen's inequality one can get $\mathbb{E}_{P_c}\big[\frac{1}{1+SP_c v^{-\alpha}}\big] \geq \frac{1}{1+S\mathbb{E}[P_c]v^{-\alpha}}$. Therefore, (4.3) can be approximated with a slight under estimation in the following.

$$\begin{aligned}\mathcal{L}_{I_c^{out}}(S) &\geq \exp\Big(-2\pi\lambda_b \int_R^{\infty} \big(1 - \frac{1}{1+S\mathbb{E}[P_c]v^{-\alpha}}\big) v dv\Big) \\ &= \exp\Big(-\pi\lambda_b (S\mathbb{E}[P_c])^{\frac{2}{\alpha}} \int_{\frac{R^2}{(S\mathbb{E}[P_c])^{\frac{2}{\alpha}}}}^{\infty} \frac{1}{1+x^{\frac{\alpha}{2}}} dx\Big). \end{aligned} \tag{4.4}$$

$$\mathbb{E}[P_c] = \int_0^R f_r(r) P_c dr = \int_0^R f_r(r) r^{\alpha} dr = \frac{2R^{\alpha}}{2+\alpha}. \tag{4.5}$$

Equation (4.4) is derived by using $x = \frac{v^2}{(S\mathbb{E}[P_c])^{\frac{2}{\alpha}}}$. Although (4.4) is a lower bound of $\mathcal{L}_{I_c^{out}}(S)$, simulation results in the next section demonstrate that (4.4) actually gives a very

tight approximation. If path-loss exponent α is set to 4, the integration in (4.4) can be eliminated and expression in (4.4) can be further simplified as

$$\mathcal{L}_{I_c^{out}}(S) = \exp\Big(- \pi\lambda_b(S\mathbb{E}[P_c])^{\frac{2}{\alpha}}\big(\frac{\pi}{2} - atan(\frac{R^2}{(S\mathbb{E}[P_c])^{\frac{2}{\alpha}}})\big)\Big). \tag{4.6}$$

$\mathcal{L}_{I_d^{in}}(S)$ can be derived by following the similar method described above.

$$\mathcal{L}_{I_d^{in}}(S) = \exp\Big(- 2\pi\lambda_d \int_0^R (1 - \mathbb{E}_{g,P_d}[\exp(-SgP_d v^{-\alpha})])vdv\Big). \tag{4.7}$$

The dummy variable v above corresponds to the distance from each S-DUE to the typical BS. Replacing P_d with ηv^α and using $g \sim \exp(1)$, the integral in (4.7) can be further simplified to

$$\begin{aligned}
\mathcal{L}_{I_d^{in}}(S) &= \exp\Big(- 2\pi\lambda_d \int_0^R (1 - \mathbb{E}_{g,P_d}[\exp(-Sg\eta v^\alpha v^{-\alpha})])vdv\Big) \\
&= \exp\Big(- 2\pi\lambda_d \int_0^R \frac{S\eta}{1+S\eta} vdv\Big) \\
&= \exp\Big(- 2\pi\lambda_d \frac{S\eta R^2}{2(1+S\eta)}\Big).
\end{aligned} \tag{4.8}$$

The second equation comes from using the moment generating function of g which is $\mathbb{E}(e^{gs}) = \frac{1}{1-s}$. The derivation of $\mathcal{L}_{I_d^{out}}(S)$ starts with the following expression,

$$\mathcal{L}_{I_d^{out}}(S) = \int_R^\infty (1 - \mathbb{E}_{g,P_d}[\exp(-SgP_d v^{-\alpha})])vdv. \tag{4.9}$$

Note that now the dummy variable v denotes the distance from each O-DUE to the typical BS. Since low power DUEs from other cells are far away from the typical BS, $1 - \mathbb{E}_{g,P_d}[\exp(-SgP_d v^{-\alpha})]$ can be approximated by its first order Taylor expansion at 0

which is $v^{-\alpha}S\mathbb{E}[g]\mathbb{E}[P_d]$. Then one can get

$$\begin{aligned}\mathcal{L}_{I_d^{out}}(S) &= \int_R^\infty v^{-\alpha}S\mathbb{E}[g]\mathbb{E}[P_d]vdv \\ &= \int_R^\infty \frac{2\eta R^\alpha}{\alpha+2}Sv^{1-\alpha}dv \\ &= \frac{2\eta R^2}{\alpha^2-4}S, \end{aligned} \tag{4.10}$$

where the second equal sign comes from $\mathbb{E}[g]=1$ and $\mathbb{E}[P_d]=\frac{2\eta R^\alpha}{\alpha+2}$. $\mathbb{E}[P_d]$ can be derived in a similar approach as how $\mathbb{E}[P_c]$ is derived. Note that the distribution of D for each DUE is the same as r. By substituting (4.4)(4.8)(4.10) back to (4.2) and applying $S=T$, the closed form (approximated) expression of the uplink CUE coverage probability is obtained.

4.3.2 DUE Coverage Probability

DUE SINR and its coverage probability can be expressed as

$$\text{SINR}_d = \frac{hP_d d^{-\alpha}}{\delta^2 + I_c + I_d} = \frac{h\eta D^\alpha d^{-\alpha}}{\delta^2 + I_c + I_d}.$$

$$\begin{aligned}\mathbb{P}[\text{SINR}_d > T] &= \int_0^R \mathbb{P}[\text{SINR}_d > T|D]f_D(D)dD \\ &= \int_0^R \mathbb{P}[h > \frac{Td^\alpha}{D^\alpha\eta}(\delta^2+I_c+I_d)|D]f_D(D)dD. \end{aligned} \tag{4.11}$$

$$\begin{aligned}\mathbb{P}[h > \frac{Td^\alpha}{D^\alpha\eta}(\delta^2+I_c+I_d)|D] &= \mathcal{L}_{I_c}(\frac{Td^\alpha}{D^\alpha\eta})\mathcal{L}_{I_d}(\frac{Td^\alpha}{D^\alpha\eta})\exp(-\delta^2\frac{Td^\alpha}{D^\alpha\eta}) \\ &\approx \mathcal{L}_{I_c}(\frac{Td^\alpha}{D^\alpha\eta})\mathcal{L}_{I_d}(\frac{Td^\alpha}{D^\alpha\eta}). \end{aligned} \tag{4.12}$$

$f_D(D)$ is the PDF of the distance from the typical DUE to its associated BS, which is the same as $f_r(r)=\frac{2r}{R^2}$, $r\in(0,R)$. Again noise is neglected in an interference limited system. From equation (4.12) one can see the interference to DUE consists of two parts, namely interference from CUEs I_c and interference from other DUEs I_d. Interfering DUEs

are not further partition into S-DUEs and O-DUEs because the distributions of S-DUEs and O-DUEs now depend on the location of the typical DUE and is hard to track. Instead, an alternative method is provided to tackle this issue in the following.

To analyze I_c, again all the interfering CUEs are assumed to follow a 2-D homogeneous PPP and their transmit powers are i.i.d. However, when analyzing the coverage probability of the typical DUE, this approximation is not as accurate as when analyzing that of the CUE shown earlier on. Two possible reasons that degrade the accuracy are as follows. First, for a CUE, the closest interfering CUE is at least R distance away from the typical BS. However, the distance between an interfering CUE and the typical DUE can be very close. Second, there is a correlation between the location of a DUE and its interfering UE (either DUE or CUE). For example, a DUE close to the cell edge receives a higher interference than the one in the cell center. Although based on the above assumption there is a gap between the analytical result and simulation result, the analytical result still provides a tight upper bound for the simulated DUE coverage probability, as shown later.

The derivation of I_d has a similar difficulty as discussed above. The accurate power distribution for the interfering DUEs is difficult to model. However, as the interference to a DUE is dominated by co-channel CUEs, one can simply assume the powers of interfering DUEs are i.i.d and this assumption will not impact the analytical results notably. The rest derivation proceeds in the following.

$$\mathcal{L}_{I_c}(S) = \exp\left(- \frac{\pi\lambda_b}{sinc(\frac{2}{\alpha})}\mathbb{E}[P_c^{\frac{2}{\alpha}}]S^{\frac{2}{\alpha}}\right). \tag{4.13}$$

$$\mathcal{L}_{I_d}(S) = \exp\left(- \frac{\pi\lambda_d}{sinc(\frac{2}{\alpha})}\mathbb{E}[P_d^{\frac{2}{\alpha}}]S^{\frac{2}{\alpha}}\right). \tag{4.14}$$

$$\mathbb{E}[P_d^{\frac{2}{\alpha}}] = \frac{\eta^{\frac{2}{\alpha}}R^2}{2}, \mathbb{E}[P_c^{\frac{2}{\alpha}}] = \frac{R^2}{2}.$$

Equations (4.13) and (4.14) are directly obtained from equation (33) in [41]. In brief, equation (33) derived in [41] states that when the locations of all the interfering devices follows a PPP with density λ, and the transmit power of each interfering device P is i.i.d.,

then the Laplace transform of the accumulated interference at a typical point I evaluated at S is

$$\mathcal{L}_I(S) = \exp\left(- \frac{\pi\lambda}{sinc(\frac{2}{\alpha})}\mathbb{E}[P^{\frac{2}{\alpha}}]S^{\frac{2}{\alpha}}\right). \tag{4.15}$$

Substituting $S = \frac{Td^\alpha}{D^\alpha\eta}$ and equations (4.13), (4.14) back to (4.12), one can get the coverage probability for the typical DUE.

$$\begin{aligned}
&\mathbb{P}[\text{SINR}_d > T] = \\
&\int_0^R \exp\left(- \frac{\pi\lambda_b}{sinc(\frac{2}{\alpha})}\mathbb{E}[P_c^{\frac{2}{\alpha}}](\frac{Td^\alpha}{D^\alpha\eta})^{\frac{2}{\alpha}}\right)* \\
&\exp\left(- \frac{\pi\lambda_d}{sinc(\frac{2}{\alpha})}\mathbb{E}[P_d^{\frac{2}{\alpha}}](\frac{Td^\alpha}{D^\alpha\eta})^{\frac{2}{\alpha}}\right)\frac{2D}{R^2}dD \\
&= \int_0^{R^2} \exp(\frac{A}{x})\frac{1}{R^2}dx \\
&= \frac{1}{R^2}\Big(x\exp(\frac{A}{x}) - AE_i(\frac{A}{x})\Big)\Big|_1^{R^2}.
\end{aligned} \tag{4.16}$$

$$A = -\frac{\pi}{sinc(\frac{2}{\alpha})}(\frac{Td^\alpha}{\eta})^{\frac{2}{\alpha}}\big(\lambda_b\mathbb{E}[P_c^{\frac{2}{\alpha}}] + \lambda_d\mathbb{E}[P_d^{\frac{2}{\alpha}}]\big). \tag{4.17}$$

The second equal sign of (4.16) is satisfied by using $x = D^2$ and $E_i(x) = \int_{-\infty}^{x}\frac{e^t}{t}dt$, which is the 1-argument exponential integral.

4.3.3 Coverage Probability without Power Control

So far the coverage probability of DUE and CUE with proposed power control scheme are derived. For comparison, the coverage probability of DUE and CUE without power control are also provided in this subsection. A fixed power $P_{d,fix}$ is assigned for all DUEs. By following the similar mathematical derivation shown above, the CUE coverage probability

is expressed in equation (4.18) and DUE coverage is provided in equation (4.19).

$$\mathbb{P}[\text{SINR}_c > T] = \exp\Big(- \pi\lambda_b (T\mathbb{E}[P_c])^{\frac{2}{\alpha}} \int_{\frac{R^2}{(S\mathbb{E}[P_c])^{\frac{2}{\alpha}}}}^{\infty} \frac{1}{1+x^{\frac{\alpha}{2}}} dx \Big) \exp\Big(- \frac{\pi\lambda_d}{sinc(\frac{2}{\alpha})} P_{d,fix}^{\frac{2}{\alpha}} T^{\frac{2}{\alpha}} \Big). \tag{4.18}$$

$$\mathbb{P}[\text{SINR}_d > T] = \exp\Big(- \frac{\pi\lambda_b}{sinc(\frac{2}{\alpha})} \mathbb{E}[P_c^{\frac{2}{\alpha}}] (\frac{Td^{\alpha}}{P_{d,fix}})^{\frac{2}{\alpha}} \Big) \exp\Big(- \frac{\pi\lambda_d}{sinc(\frac{2}{\alpha})} P_{d,fix}^{\frac{2}{\alpha}} (\frac{Td^{\alpha}}{P_{d,fix}})^{\frac{2}{\alpha}} \Big). \tag{4.19}$$

4.4 Numerical Evaluation

In this section numerical results are presented from both analytical study and simulation. The coverage performance is evaluated for two cases, one with power control and the other one without power control. The impact of D2D power control parameter η on the overall coverage is also discussed. Unless otherwise mentioned, the parameters used in simulations are given in Table 4.1.

Table 4.1: Simulation Parameters

Density of BS λ_b	$10^{-6}\ m^{-2}$
Density of D2D pairs λ_d	$10 \cdot \lambda_b$
D2D power control parameter η	0.001
Pathloss exponent α	4
D2D transmission length d	25 m

From Figure 4.2 one can see that the analytical result (blue solid line) matches the simulation result (blue circles) very well. Recall that in the analysis, the locations of other cell CUEs are approximated to follow a PPP, whereas in the simulation each other cell CUE is uniformly distributed in the associated cell. To further investigate the impact of assumptions made during analysis, the simulation results for two other cases are also included. One assumes that other cell CUEs are distributed as PPP and the other one assumes other cell CUEs are uniformly distributed, both with no DUEs. The uniform

distribution is more accurate while the PPP distribution is an approximation made in this paper for better analytical tractability. From the two red curves in Figure 4.2, the PPP assumption actually results in a quite tight upper bound estimation for the more realistic uniform distribution. Another notable outcome is that under the proposed scheme the CUE coverage in the system with underlay DUEs (blue dots) is almost the same as the CUE coverage without underlay DUEs (red dots), which clearly shows that the existence of DUEs only has a slight impact on CUEs if distance-based power control is applied.

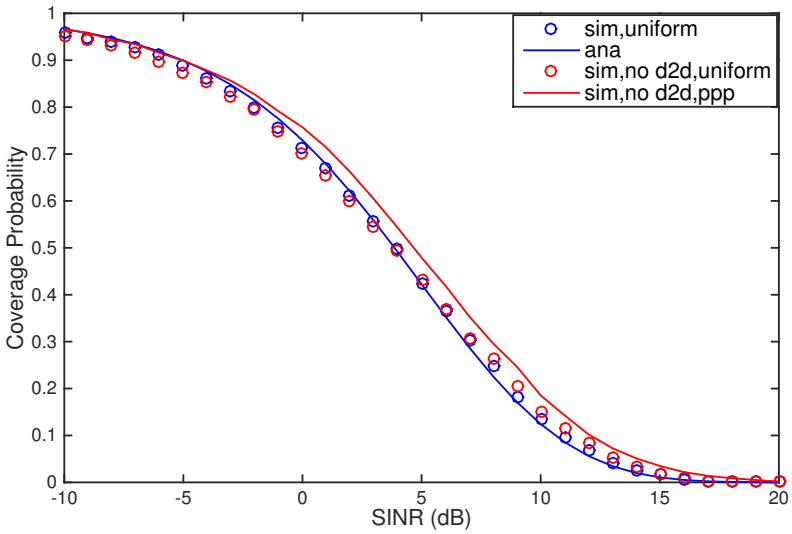

Fig. 4.2: CUE Coverage Probability: Theoretical vs. Simulation

In Figure 4.3, even with a few assumptions made during DUE coverage analysis, the analytical results for DUE coverage can still match the simulation results very well. The analytical results provide a tight upper bound in most of the cases. Recall that $P_d = \eta D^{\alpha}$. Thus a higher η value allows for a higher transmit power from DUEs, leading to better DUE coverage, as shown in Figure 4.3. However, a higher η value could potentially impact CUE coverage. More results will be presented in the next two figures.

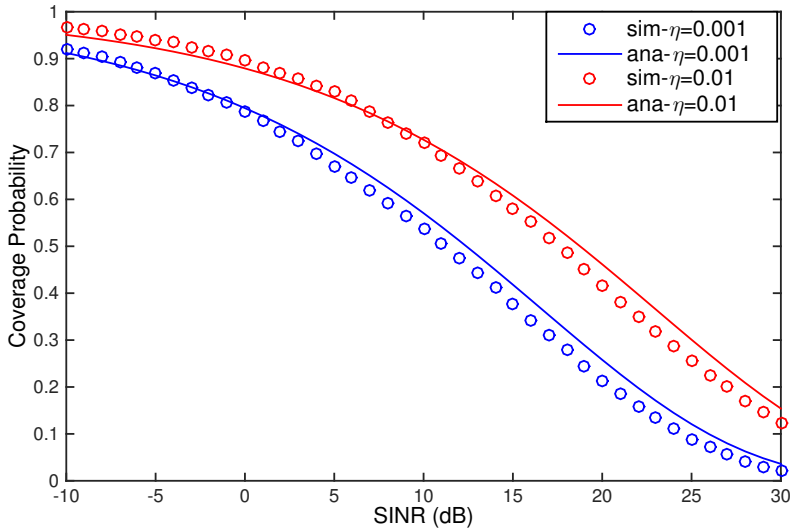

Fig. 4.3: DUE Coverage Probability: Theoretical vs. Simulation

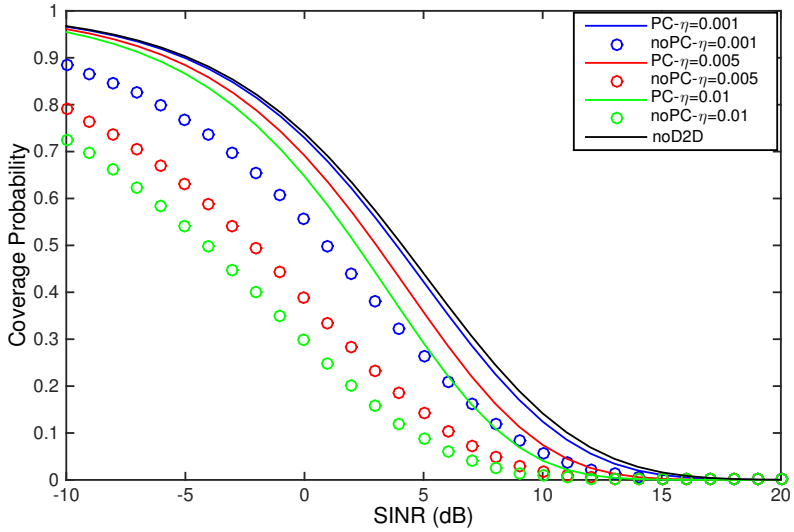

Fig. 4.4: CUE Coverage Probability: Power Control vs. No Power Control

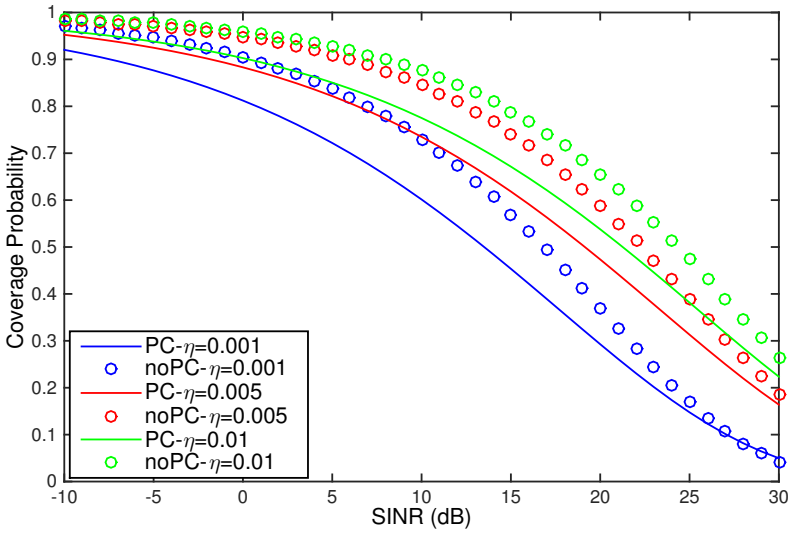

Fig. 4.5: DUE Coverage Probability: Power Control vs. No Power Control

Further in Figure 4.4 and Figure 4.5, the performance between the two cases are compared, one with the proposed distance-based power control and one without power control. More specifically, DUEs in the no power control case are set with a fixed transmit power $P_{d,fix} = \mathbb{E}[P_d]$. Figure 4.4 shows that the distance based power control scheme can effectively protect CUEs from being interfered by DUEs. With $\eta = 0.001$, there is barely any impact on CUEs from DUEs with power control while at the same time about 80 percent DUEs have SINR above 0 dB. In the no power control case, although Figure 4.5 shows setting DUE power at a fixed value can improve the performance of DUEs to some extent, the interference to CUEs is clearly causing CUE performance to degrade as shown in Figure 4. Note that significant performance degradation of CUE should be avoided since in most cases CUEs are considered as the primary users. By further observing the curves with $\eta = 0.005$ and $\eta = 0.01$ in Figure 4.5, one can see that the DUE performance gain from power increase quickly saturates when η exceeds a certain value. This is because if the transmit power of DUEs increases to a certain level, the interference from other DUEs becomes dominant compared to the interference from CUEs, which offsets the increase of DUE signal power and causes the saturation of DUE performance improvement.

4.5 Conclusion

In this chapter, a distance-based power control scheme is developed for underlay D2D in an uplink cellular network. The developed scheme is able to support dense D2D communications without causing a notable performance degradation to the primary cellular users. The coverage probabilities of both CUEs and DUEs under developed scheme are analyzed by using stochastic geometry method. Although some approximations are applied during the analysis, the analytical results are still accurate as validated by the simulation results. The developed scheme is proven to benefit both CUEs and DUEs. Owing to the simplicity of the scheme, it can be combined with other more sophisticated resource allocation or interference cancellation schemes conveniently.

CHAPTER 5

Introduction to NOMA

5.1 Overview

In the existing wireless communications systems such as 4G LTE, orthogonal multiple access (OMA) schemes such as orthogonal frequency division multiple access (OFDMA) and single carrier frequency division multiple access (SC-FDMA) have been widely used [48]. While OMA can effectively minimize inter-user interference with a relatively low implementation complexity, its spectral efficiency and connectivity capability can be further improved [49]. In order to meet demands such as very high data rates and tremendous connectivities required by the next generation (5G) cellular network [1], new radio access technologies (RATs) are actively pursued and explored.

Non-orthogonal multiple access (NOMA), recognized as a promising candidate RAT in the 5G wireless system, has received tremendous attention lately. In contrast to OMA, NOMA allows multiple users to use the same frequency/time resource at the same time and offers many advantages such as improving spectral efficiency, enhancing connectivity, providing higher cell-edge throughput, and reducing transmission latency [14–17, 50]. NOMA is generally classified into two categories, namely code domain NOMA (CD-NOMA) and power domain NOMA (PD-NOMA). CD-NOMA utilizes different codes on the same resource to achieve multiplexing gain while PD-NOMA assigns users with distinct power levels to maximize the performance. CD-NOMA can obtain a spreading gain at the cost of more consumed bandwidth [16]. PD-NOMA multiplexes users on the power domain. At the transmitter side, messages for multiple users are superposed by Superposition Coding (SC) [51]. At the receiver side, Successive Interference Cancellation (SIC) [52, 53] is utilized to extract the intended message. This dissertation focuses on PD-NOMA and just refer it as NOMA if not otherwise mentioned.

There have been many standardization activities on the implementation of NOMA in 5G wireless mobile networks. Particularly, in [54] the performance of multiuser superposition transmission (MUST), the downlink version of NOMA, is comprehensively studied and some conclusions are drawn in the following.

- MUST can increase system capacity as well as improve user experience in certain scenarios.
- MUST is generally more beneficial when the network experiences higher traffic load.
- MUST is generally more beneficial in user-perceived throughput for wideband scheduling case, compared to the subband scheduling case.
- MUST is generally more beneficial in user-perceived throughput for cell-edge users, compared to other UEs.
- MUST-far users can be legacy users when quadrature phase-shift keying (QPSK) is applied to MUST-far users or the most two significant bits in the modulation symbol are assigned to far UE.

Based on the advantages of MUST listed above, MUST can be implemented in scenarios of 5G networks such as machine-to-machine (M2M) communications, ultra-dense networks (UDN) and massive machine-type communications (mMTC) [55] where massive connections and the Internet of Things (IoT) functionality of 5G are required.

5.2 NOMA Basics

Figure 5.1 illustrates a simple downlink NOMA scenario with one base station (BS) and 2 user equipments (UEs). The transmission bandwidth allocated to two UEs is 1 Hz. In NOMA, signals for 2 UEs are superposed by using SC at the transmitter side. Denoting the signal for UE-i, $i \in \{1, 2\}$, as x_i where $\mathbb{E}[|x_i|^2] = 1$, the coded signal at transmitter is

$$x = \sqrt{P_1}x_1 + \sqrt{P_2}x_2.$$

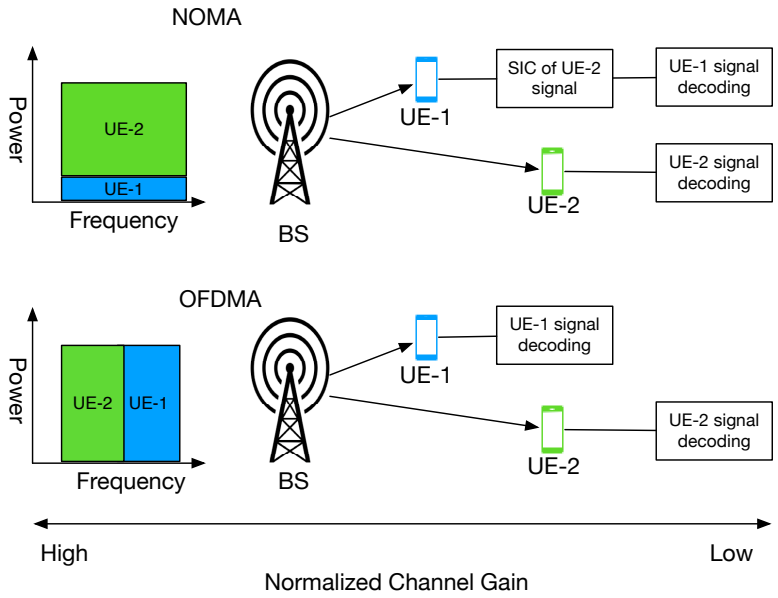

Fig. 5.1: Simple comparison between basic downlink NOMA and OMA (OFDMA)

P_i is the transmit power allocated to UE-i and the sum of P_i is restricted to P, i.e., $P_1 + P_2 = P$. In this example P_i is set as $P_1 = 0.2P$ and $P_2 = 0.8P$. Then the received signal at UE-i is

$$y_i = h_i x + w_i,$$

where w_i denotes that Gaussian noise including inter-cell interference and the power density of w_i is N_0. h_i is the complex channel coefficient from BS to UE-i. In downlink NOMA, SIC is implemented at UEs and the optimal decoding order is in the order of increasing channel gain normalized by noise and inter-cell interference, i.e., $\frac{|h_i|^2}{N_0}$ [56, 57]. In the 2-UE case above, assuming $\frac{|h_1|^2}{N_0} > \frac{|h_2|^2}{N_0}$, UE-2 does not need to perform SIC since it comes first in the decoding order. Therefore, UE-2 decodes its received signal x_2 directly treating x_1 as interference and the throughput of UE-2 can be represented as

$$R_2 = \log_2 \left(1 + \frac{P_2|h_2|^2}{P_1|h_2|^2 + N_0}\right).$$

Different from UE-2, UE-1 first decodes x_2 to subtract its component from the received signal y_1. The throughput at UE-1 decoding x_2 can be then represented as

$$R_{1\to 2} = \log_2\left(1 + \frac{P_2|h_1|^2}{P_1|h_1|^2 + N_0}\right).$$

As $\frac{|h_1|^2}{N_0} > \frac{|h_2|^2}{N_0}$, $R_{1\to 2} > R_2$ is guaranteed which means x_2 can be completely decoded at UE-1 assuming SIC process at UE-1 is error free. After subtracting x_2 from y_1, the throughput of UE-1 decoding its own signal x_1 is

$$R_1 = \log_2\left(1 + \frac{P_1|h_1|^2}{N_0}\right).$$

In comparison with NOMA, the throughput of each UE in OMA (i.e., OFDMA) systems shown in Figure 5.1 can be derived as

$$R_1^o = \frac{1}{2}\log_2\left(1 + \frac{P|h_1|^2}{N_0}\right), R_2^o = \frac{1}{2}\log_2\left(1 + \frac{P|h_2|^2}{N_0}\right), \tag{5.1}$$

by assuming the bandwidth and the transmit power are allocated to each UE equally. When $\frac{|h_1|^2}{N_0} = 20$ dB and $\frac{P|h_2|^2}{N_0} = 0$ dB, the authors of [56] numerically compared throughput of each UE between NOMA and OMA, and demonstrated that the corresponding gains of NOMA from OMA are 32% and 48% for UE-1 and UE-2, respectively. Besides the numerical example shown here, the performance gain of NOMA is also theoretically analyzed in [15].

The gain of NOMA comes from the multiplexing gain, which is achieved from the channel gain difference between 2 UEs through using SC at the transmitter side and SIC at the receiver side. Although in NOMA the transmit power allocated to a single UE can be lower than that in OMA, i.e., the transmit power of UE-1 is $0.2P$ and $0.5P$ for NOMA and OMA respectively, both UEs can benefit from more bandwidth scheduled to them. While NOMA relies on advanced receiver processing ability such as SIC, the expectation for processing ability advancement of user devices is reasonable, generally following Moore's law. The merits of NOMA can be summarized as the following [16].

1. Spectral Efficiency: As shown in the example above, NOMA can offer higher spectral efficiency for both UEs. This advantage of NOMA over OMA can also be explained from the perspective of information theory. As proofed in [58], NOMA with SC at the transmitter side and SIC at the receiver side can achieve the optimal capacity region of the downlink broadcast channel. However, OMA is not able to do so.

2. Connectivity: Different with OMA, the number of supported users in NOMA is not strictly limited by the amount of available resources and their scheduling granularity. Therefore, NOMA can be used to address the challenges of massive connectivity.

3. Robust Performance Gain: NOMA transmitter does not rely much on instantaneous channel state information (CSI), which requires timely feedback signaling from UEs, to perform multiplexing. Therefore the robust performance gain can be expected irrespective UE mobility and signaling latency.

5.3 Related works

Non-orthogonal multiple access (NOMA), as a promising candidate RAT in the 5G network, has received considerable attention recently [15, 56, 59, 60]. Many problems about NOMA have been studied by published works. In [59], the authors considered user fairness in the downlink NOMA and investigated power allocation (PA) techniques that ensure fairness for users. Authors of [61] investigated the system level performance of NOMA in various environments including macro cells and small cells, and showed that the performance gain of NOMA can be obtained in both macro cell and small cell deployments. In [62], authors proposed two user pairing schemes and investigated how to further enhance the performance gain of NOMA over conventional OMA.

Authors in [15] developed analytical results on outage probability for m-th UE and of the ergodic sum rate in a single cell downlink NOMA. However, due to less tractability of the model used in [15], the closed form expression for the ergodic sum rate is difficult to derive. Moreover, inter-cell interference, which is a pervasive problem in most of the

existing wireless networks, is not explicitly considered in [15] and neither do many other works on NOMA.

The study in [59] showed that NOMA can be applied to both downlink and uplink. However, so far downlink is considered more promising and has been preliminarily standardized as introduced in the last section. The number of existing works on uplink NOMA is limited. Authors in [63] proposed a power back-off scheme, in which the arrived power of each UE is gradually degraded with certain step size. However, inter-cell interference is not considered in this work.

5.4 Contributions

As introduced in the last section, the existing works focusing on the performance analysis on NOMA haven been quite limited. Moreover, to the best of our knowledge, none of these works considered the inter-cell interference due to the lack of tractable mathematical models. Motivated by this observation, research on NOMA in this dissertation mainly focuses on developing tractable models for both downlink and uplink NOMA in a multi-cell system by using stochastic geometry tools. The contribution of each chapter on NOMA is summarized as follows.

In Chapter 6, the performance of downlink NOMA is evaluated in term of the coverage probability and average achievable rate by using a stochastic geometry model. More specifically, the PPP model is used in the study. The inter-cell interference is explicitly considered. Without loss of generality, the analysis starts with a 2-UE NOMA case. Then the analytical results are extended to a general M-UE NOMA scenario. Owing to the tractability of the PPP model, all the analytical results are expressed in a pseudo-closed form with computable numerical integration, or in a nice closed form under some special cases. The developed work can be used as a framework for downlink NOMA and to incorporate more advanced schemes such as optimal NOMA power allocation and user pairing.

In Chapter 7, a fractional power control (FPC) based uplink NOMA scheme is proposed and the analytical model is formulated using stochastic geometry to evaluate the performance of the proposed scheme. As the complexity of SIC scales at least linearly with

the number of the users that are involved in a transmission [64], NOMA with 2 or 3 simultaneously multiplexed users is practical in reality [65]. The work in Chapter 7 focuses on the NOMA study with 2 UEs forming a NOMA pair. Whereas the analytical results derived in this chapter can be extended to a general NOMA case.

Although downlink and uplink NOMA are addressed in Chapter 6 and Chapter 7 respectively, the models developed in these two chapters are different. In Chapter 8, a unified downlink and uplink NOMA model is developed. Different with the models developed in Chapter 6 and 7, which can only be used to model downlink or uplink scenario, the model developed in Chapter 8 can be used for both downlink and uplink scenarios. Also, a user pairing scheme is proposed and analyzed in Chapter 8.

In addition to the analytical frameworks developed for general NOMA system, the gain of NOMA with SWIPT over OMA in terms of harvested energy is investigated in Chapter 9. With the power splitting scheme proposed in Chapter 9, UEs can harvest the maximum amount of energy while still achieve the same data rates as what can be achieved in the traditional OMA schemes.

CHAPTER 6

Stochastic Geometry Based Performance Study on Downlink NOMA

The principle of downlink NOMA is introduced in Chapter 5. Before the content of this chapter is published in [66], [15] is the only one that focuses on evaluating the performance of downlink NOMA by using the stochastic geometry method. As mentioned previously, the work in [15] is less tractable and did not take inter-cell interference into consideration. In this chapter, the PPP model is used to analyze the system performance of downlink NOMA.

6.1 System Model

A multi-cell downlink cellular network is considered in this chapter. The location of BSs follows a 2-D homogeneous PPP Φ with a density λ. Each UE is associated with the closest BS, which means UEs associated with a BS are located in the Voronoi cell of the associated BS as shown in Figure 6.1. The transmission distance between UE_i and its associated BS is denoted by r_i. For all UEs, $\{r_i\}$ is independently and identically distributed (i.i.d.) with a probability density function (PDF) given in [3] as $f_{r_i}(r_i) = e^{-\lambda\pi r_i^2} 2\pi\lambda r_i$. The reuse factor of the system under study is 1. Hence all the cells have the same radio resources which can be normalized to 1. An interference limited wireless system is assumed given a dense deployment of small cells and hence the impact of noise can be neglected throughout this chapter. All BSs transmit at the power P_{total}. A channel model that comprises standard path-loss and Rayleigh fading is adopted. $c_i = \frac{h_i r_i^{-\alpha}}{I_i}$ is defined as the channel gain of UE_i normalized by interference, where $h_i \sim \exp(1)$ denotes Rayleigh fading gain and $r_i^{-\alpha}$ corresponds to path-loss. $\alpha > 2$ is the path-loss exponent and $I_i = \sum_{j \in \Phi / b_o} g_j R_{j,i}^{-\alpha} P_{total}$ is the sum of the inter-cell interference from all other BSs, where g_j and $R_{j,i}$ are the Rayleigh fading gain of interfering channel and transmission distance from BS j to UE_i, respectively. Without loss of generality, a NOMA group consists of M UEs, which are sorted based on

their normalized channel gain in ascending order as $c_1 \leq \cdots \leq c_M$. Based on this order, NOMA scheme can allow UE_i to decode the interfering NOMA signals from UE_m, $m \leq i$, and then remove the interfering NOMA signals from the received signal, in a successive manner. Assume the transmission power of UE_i is P_i with $\sum_{i \in M} P_i = P_{total}$. According to the principle of NOMA and the order of UE channel gains, P_i is allocated in descending order, i.e., $P_1 \geq \cdots \geq P_M$, which is reverse to the order of c_i.

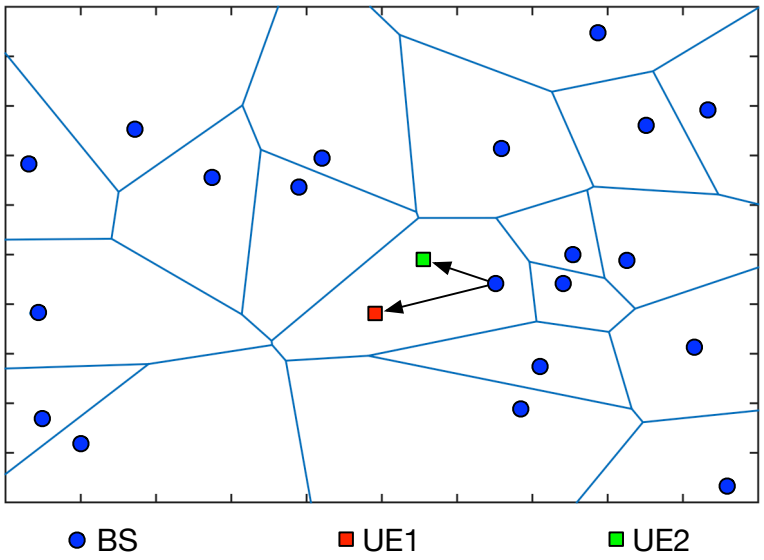

Fig. 6.1: System Model

6.2 Coverage Probability and Average Achievable Rate

In this section, the coverage probability for each UE in a typical cell is analyzed. After that, the average achievable rate is further computed by using the derived analytical results. For simplicity, the analysis starts with a 2-UE NOMA case and then is further extended to a general NOMA scheme with M UEs, $M \geq 2$. The signals intended to UE_1 and UE_2 are denoted as x_1 and x_2, respectively, where $\mathbb{E}[|x_i|^2] = 1$. According to the NOMA principle [56], the transmitted signal at BS is coded as the composite signal from UE_1 and

UE_2,

$$x = \sqrt{P_1}x_1 + \sqrt{P_2}x_2. \tag{6.1}$$

Thus the received signal at UE_i can be represented in an interference limited system as

$$y_i = \sqrt{h_i r_i^{-\alpha}}x + \sqrt{I_i}. \tag{6.2}$$

The coverage probability is defined as $\mathbb{P}[SIR > T]$, which represents the probability that the instantaneous signal-to-interference ratio (SIR) of any UE is greater than a certain threshold T. It can also be understood as the complementary cumulative distribution function (CCDF) of SIR over the entire network. The SIR used here is different from the definition of SIR in OMA. Other than the real SIR at the receiving antenna of a UE, the SIR after SIC that can be used to calculate the average achievable rate is of more interest. The SIR after SIC is named as NOMA SIR throughout this dissertation. In the 2-UE case, UE_1 does not need to perform interference cancellation and directly treats x_2 as interference since it comes the first in the decoding order. UE_2 first decodes x_1 and removes it from the received composite signal y_2, based on which UE_2 can further decode x_2. Assuming successful decoding and no error propagation, the NOMA SIR of UE_1 and UE_2 can be respectively expressed as

$$SIR_1 = \frac{h_1 r_1^{-\alpha} P_1}{I_1 + h_1 r_1^{-\alpha} P_2}, \quad SIR_2 = \frac{h_2 r_2^{-\alpha} P_2}{I_2}. \tag{6.3}$$

6.2.1 Channel Gain Distribution

To evaluate the coverage probability, channel gain distribution needs to be derived at first. For a given normalized channel gain $c = \frac{hr^{-\alpha}}{I}$, where h, r and I are the corresponding components as defined before by removing the subscripts, the cumulative distribution function (CDF) is $F_c(C) = \mathbb{P}[c \leq C] = 1 - \mathbb{P}[c > C]$. By following the similar way presented in [3], the complete expression of $\mathbb{P}[c > C]$ is given below.

$$\begin{aligned}\mathbb{P}[c > C] &= \mathbb{E}_r[\mathbb{P}[c > C|r]] \\ &= \int_{r>0} \mathbb{P}\Big[\frac{hr^{-\alpha}}{I} > C\Big|r\Big] f_r(r)dr \\ &= \int_{r>0} \mathbb{E}_I[\mathbb{P}[h > Cr^{\alpha}I|r, I]]f_r(r)dr \\ &\overset{(a)}{=} \int_{r>0} \mathbb{E}_I[\exp(-Cr^{\alpha}I)|r, I]f_r(r)dr \\ &= \int_{r>0} \mathcal{L}_I(Cr^{\alpha})f_r(r)dr, \end{aligned} \tag{6.4}$$

where (a) follows from $h \sim \exp(1)$. $\mathcal{L}_I(s) = \mathbb{E}_I[e^{-sI}]$ is the Laplace transform of random variable I evaluated on s. The full expression of $\mathcal{L}_I(s)$ is given by

$$\begin{aligned}\mathcal{L}_I(s) &= \mathbb{E}_{\Phi,g}\Big[\exp(-s\sum_{j\in\Phi/b_o} g_j R_j^{-\alpha}P_{total})\Big] \\ &= \mathbb{E}_{\Phi}\Big[\prod_{j\in\Phi/b_o} \mathbb{E}_{g_j}[\exp(-sg_jR_j^{-\alpha}P_{total})]\Big] \\ &\overset{(a)}{=} \exp\Big(-2\pi\lambda\int_r^{\infty}\big(1-\mathbb{E}_g[\exp(-sgv^{-\alpha}P_{total})]\big)vdv\Big) \\ &\overset{(b)}{=} \exp\Big(-2\pi\lambda\int_r^{\infty}\big(1-\frac{1}{1+sv^{-\alpha}P_{total}}\big)vdv\Big) \\ &= \exp\Big(-2\pi\lambda\int_r^{\infty}\frac{1}{1+\frac{v^{\alpha}}{sP_{total}}}vdv\Big) \\ &\overset{(c)}{=} \exp\Big(-\pi\lambda(sP_{total})^{\frac{2}{\alpha}}\int_{\frac{r^2}{(sP_{total})^{\frac{2}{\alpha}}}}^{\infty}\frac{1}{1+u^{\frac{\alpha}{2}}}du\Big). \end{aligned} \tag{6.5}$$

In the above (a) follows from the probability generating functional (PGFL) of PPP [9], which states that $\mathbb{E}[\prod_{x\in\Phi} f(x)] = \exp(-\lambda\int_{\mathbb{R}^2}(1-f(x))dx)$. (b) follows from $g \sim \exp(1)$ and (c) is acquired by change of variable $u = \frac{v^2}{(sP_{total})^{\frac{2}{\alpha}}}$. By substituting $s = Cr^{\alpha}$ back into (6.5), one can get the complete expression of $\mathcal{L}_I(Cr^{\alpha})$ as

$$\mathcal{L}_I(Cr^{\alpha}) = \exp\Big(-\pi\lambda r^2(CP_{total})^{\frac{2}{\alpha}}\int_{(CP_{total})^{-\frac{2}{\alpha}}}^{\infty}\frac{1}{1+u^{\frac{\alpha}{2}}}du\Big). \tag{6.6}$$

Combining (6.6) with (6.4) and using $f_r(r) = e^{-\lambda\pi r^2} 2\pi\lambda r$, one can write the following.

$$\begin{aligned}
&\mathbb{P}[c > C] \\
&= \int_{r>0} \exp\Big(- \pi\lambda r^2 (CP_{total})^{\frac{2}{\alpha}} \int_{(CP_{total})^{-\frac{2}{\alpha}}}^{\infty} \frac{1}{1+u^{\frac{\alpha}{2}}} du \Big) \\
&\quad \cdot e^{-\lambda\pi r^2} 2\pi\lambda r dr \\
&\overset{(a)}{=} \int_{v>0} e^{\left(-v\pi\lambda(1+(CP_{total})^{\frac{2}{\alpha}} \int_{(CP_{total})^{-\frac{2}{\alpha}}}^{\infty} \frac{1}{1+u^{\frac{\alpha}{2}}} du)\right)} \pi\lambda dv \\
&= \frac{1}{1+(CP_{total})^{\frac{2}{\alpha}} \int_{(CP_{total})^{-\frac{2}{\alpha}}}^{\infty} \frac{1}{1+u^{\frac{\alpha}{2}}} du},
\end{aligned} \tag{6.7}$$

where (a) uses $v = r^2$. Finally, the CDF of the channel gain is derived as

$$F_c(C) = 1 - \frac{1}{1+(CP_{total})^{\frac{2}{\alpha}} \int_{(CP_{total})^{-\frac{2}{\alpha}}}^{\infty} \frac{1}{1+u^{\frac{\alpha}{2}}} du}. \tag{6.8}$$

For a special case with $\alpha = 4$, (6.8) can be further simplified to

$$F_c(C) \overset{\alpha=4}{=} 1 - \frac{1}{1+\sqrt{CP_{total}}(\frac{\pi}{2} - \arctan(\frac{1}{\sqrt{CP_{total}}}))}. \tag{6.9}$$

Knowing only the CDF of the channel gain is sufficient to compute the UE coverage probability in the system model considered in this chapter. The PDF of channel gain is also presented for any further NOMA study based on this framework. By taking the derivative on $F_c(c)$, the PDF can be found as

$$\begin{aligned}
f_c(c) &= \frac{dF_c(c)}{dc} \\
&= \frac{\mu(c)'\nu(c) + \mu(c)\nu'(c)}{1 + 2\mu(c)\nu(c) + \mu(c)^2\nu(c)^2},
\end{aligned} \tag{6.10}$$

where

$$\mu(c) = (cP_{total})^{\frac{2}{\alpha}}, \quad \mu'(c) = \frac{d\mu(c)}{dc} = \frac{2}{\alpha} P_{total}^{\frac{2}{\alpha}} c^{\frac{2}{\alpha}-1},$$

$$\nu(c) = \int_{(cP_{total})^{-\frac{2}{\alpha}}}^{\infty} \frac{1}{1+u^{\frac{\alpha}{2}}} du,$$

$$\nu'(c) = \frac{d\nu(c)}{dc} = \frac{2P_{total}}{\alpha(cP_{total})^{\frac{2}{\alpha}}(1+cP_{total})}.$$

6.2.2 NOMA Coverage for the 2-UE case

In this subsection, the coverage probability for UE_1 and UE_2 in a 2-UE NOMA case are derived. Two UEs among all UEs associated with the typical BS are randomly selected and marked as UE_a and UE_b. These two UEs are ranked based on their channel gains in an ascending order. After sorting, the subscript of two selected UE will be remarked as $UE_1 = \{UE_i | UE_i \in \{UE_a, UE_b\}, c_i = \min(c_a, c_b)\}$ and $UE_2 = \{UE_i | UE_i \in \{UE_a, UE_b\}, c_i = \max(c_a, c_b)\}$. Now $c_1 = \min(c_a, c_b)$ and $c_2 = \max(c_a, c_b)$, which follows the order rule as $c_1 \leq c_2$. Based on [67], for $z = \max(x, y)$ and $w = \min(x, y)$, the CDF of z and w can be determined as $F_z(z) = F_{xy}(z, z)$ and $F_w(w) = F_x(w) + F_y(w) - F_{xy}(w, w)$. As $\{c_i\}$ is i.i.d. and $F_c(c)$ is given in (6.8), the CDF of c_1 and c_2 can be obtained as follows.

$$\begin{aligned} F_{c_1}(c_1) &= F_{c_a}(c_1) + F_{c_b}(c_1) - F_{c_a c_b}(c_1, c_1) \\ &= 2F_c(c_1) - F_c(c_1)^2. \end{aligned} \tag{6.11}$$

$$F_{c_2}(c_2) = F_{c_a c_b}(c_2, c_2) = F_c(c_2)^2. \tag{6.12}$$

For a target SIR value of T, the coverage probability of UE_1 is

$$\begin{aligned} \mathbb{P}[SIR_1 > T] &= 1 - \mathbb{P}[SIR_1 \leq T] \\ &= 1 - \mathbb{P}\Big[\frac{h_1 r_1^{-\alpha} P_1}{I_1 + h_1 r_1^{-\alpha} P_2} \leq T\Big] \\ &= 1 - \mathbb{P}\Big[\frac{1}{\frac{I_1}{h_1 r_1^{-\alpha} P_1} + \frac{P_2}{P_1}} \leq T\Big] \\ &= 1 - \mathbb{P}\Big[\frac{I_1}{h_1 r_1^{-\alpha} P_1} \geq \frac{1}{T} - \frac{P_2}{P_1}\Big]. \end{aligned} \tag{6.13}$$

Due to NOMA inter-user interference, SIR_1 has an upper bound as $\lim_{I_1 \to 0} SIR_1 = \frac{P_1}{P_2}$. So $\mathbb{P}[SIR_1 > T] = 0$ when $T \geq \frac{P_1}{P_2}$. When $T < \frac{P_1}{P_2}$, the derivation is continued as

$$\begin{aligned}
\mathbb{P}[SIR_1 > T] &= 1 - \mathbb{P}\Big[\frac{h_1 r_1^{-\alpha}}{I_1} \leq \frac{1}{\big(\frac{1}{T} - \frac{P_2}{P_1}\big)P_1}\Big] \\
&= 1 - \mathbb{P}\Big[c_1 \leq \frac{1}{\big(\frac{1}{T} - \frac{P_2}{P_1}\big)P_1}\Big] \\
&= 1 - F_{c_1}\left(\frac{1}{\frac{P_1}{T} - P_2}\right). \qquad (6.14)
\end{aligned}$$

The coverage probability of UE_2 can be acquired by following the same method above hence the result is given directly without details for derivation. It assumes that the NOMA inter-user interference form UE_1 is completely eliminated by SIC at UE_2. There is no such a limitation on SIR_2, as on SIR_1.

$$\mathbb{P}[SIR_2 > T] = 1 - F_{c_2}\left(\frac{T}{P_2}\right). \qquad (6.15)$$

For a general α, the coverage probability of UE_i is in a quasi-closed form due to the numerical integration included in (6.8). When $\alpha = 4$, a nice closed form expression can be acquired by employing (6.9) instead of (6.8).

6.2.3 Average Achievable Rate for 2-UE case

In this subsection, the average achievable rate of UE_i is computed in units of nats/Hz (1 bit = ln(2) =0.693 nats). It is assumed that all UEs use adaptive modulation and coding so that they can achieve Shannon bound for their instantaneous SIR, i.e. $\ln(1 + SIR)$. τ_i

denotes the average achievable rate of UE_i. For UE_1,

$$\begin{aligned}
\tau_1 &\triangleq \mathbb{E}[\ln(1+SIR_1)] \\
&= \int_{c_1>0} \mathbb{E}\Big[\ln\Big(1+\frac{h_1 r_1^{-\alpha} P_1}{I_1 + h_1 r_1^{-\alpha} P_2}\Big)\Big] f_{c_1}(c_1) dc_1 \\
&\overset{(a)}{=} \int_{c_1>0}\int_{t>0} \mathbb{P}\Big[\ln\Big(1+\frac{h_1 r_1^{-\alpha} P_1}{I_1 + h_1 r_1^{-\alpha} P_2}\Big) > t\Big] dt \cdot f_{c_1}(c_1) dc_1 \\
&\overset{(b)}{=} \int_{c_1>0}\int_{t=0}^{\ln(\frac{P_1}{P_2}+1)} \mathbb{P}\Big[\frac{h_1 r_1^{-\alpha} P_1}{I_1 + h_1 r_1^{-\alpha} P_2} > e^t - 1\Big] dt \cdot f_{c_1}(c_1) dc_1 \\
&= \int_{t=0}^{\ln(\frac{P_1}{P_2}+1)} \Big(1 - F_{c_1}\Big(\frac{1}{\frac{P_1}{e^t-1} - P_2}\Big)\Big) dt,
\end{aligned} \tag{6.16}$$

where (a) follows from $\mathbb{E}[X] = \int_{t>0} \mathbb{P}(X > t) dt$ for a positive random variable X and (b) follows from $\lim_{I_1 \to 0} \ln(1 + \frac{h_1 r_1^{-\alpha} P_1}{I_1 + h_1 r_1^{-\alpha} P_2}) = \ln(\frac{P_1}{P_2} + 1)$. The achievable average rate of UE_2, τ_2, can be derived in the same way.

$$\tau_2 = \int_{t>0} \Big(1 - F_{c_2}\big(\frac{e^t - 1}{P_2}\big)\Big) dt. \tag{6.17}$$

6.2.4 Coverage Probability and Average Achievable Rate for the M-UE case

By observing the expression of coverage probability and the achievable average rate for UE_1 and UE_2 in the 2-UE case, the results can be extended into a general M-UE NOMA scenario. The SIR of UE_i in an M-UE scenario can be expressed as

$$\begin{aligned}
SIR_i &= \frac{h_i r_i^{-\alpha} P_i}{I_i + h_i r_i^{-\alpha} \sum_{j=i+1}^{M} P_j} \\
&= \frac{1}{\frac{1}{c_i P_i} + \frac{\sum_{j=i+1}^{M} P_j}{P_i}}.
\end{aligned} \tag{6.18}$$

Notice that $\sum_{j=i+1}^{M} P_j = 0$ when $i = M$. There is an upper bound for all $SIR_i, i \neq M$ as $\lim_{I_i \to 0} SIR_i = \frac{P_i}{\sum_{j=i+1}^{M} P_j}$. So for $T > \frac{P_i}{\sum_{j=i+1}^{M} P_j}$, the coverage probability of UE_i is 0 and for $T \leq \frac{P_i}{\sum_{j=i+1}^{M} P_j}$, the expression can be derived by following the same method applied on

the 2-UE case. The complete result can be expressed as

$$\mathbb{P}[SIR_i > T] = \begin{cases} 0, & \text{if } T > \frac{P_i}{\sum_{j=i+1}^{M} P_j}; \\ 1 - F_{c_i}\Big(\frac{1}{\frac{P_i}{T} - \sum_{j=i+1}^{M} P_j}\Big), & \text{otherwise.} \end{cases} \tag{6.19}$$

$F_{c_i}(c_i)$ can be calculated using the knowledge of order statistics [68]. For n independent random variables $X_1, X_2, ..., X_n$ each with CDF P(x), the CDF of mth order statistics $X_{(m)}$ is $F_m(x) = \sum_{i=m}^{n} \binom{n}{i} P^i(x)[1 - P(x)]^{n-i}$. The smallest order statistics $X_{(1)}$ and the highest one $X_{(n)}$ have simpler expressions as $F_1(x) = 1 - [1 - P(x)]^n$ and $F_{(n)}(x) = P^n(x)$. Since $\{c_i\}$ is i.i.d., the CDF of UE_i's channel gain can be expressed as

$$F_{c_i}(c_i) = \sum_{j=i}^{M} \binom{M}{j} F_c(c_i)^j [1 - F_c(c_i)]^{M-j}. \tag{6.20}$$

Again for the sake of completeness, the PDF of c_i is also given as

$$f_{c_i}(c_i) = \frac{M!}{(i-1)!(M-i)!} F_c^{i-1}(c_i)[1 - F_c(c_i)]^{M-i} f_c(c_i). \tag{6.21}$$

By using (6.19), the average achievable rate can be computed by following the same method applied in the last subsection. Due to the limitation of coverage probability, the average achievable rate of UE_i also has an upper bound as $\lim_{I_i \to 0} \tau_i = \ln(1 + \frac{P_i}{\sum_{j=i+1}^{M} P_j})$ for $i \neq M$. The complete expression of τ_i is provided below. Notice that when $i = M$, the range of the integration is $(0, \infty)$.

$$\tau_i = \int_{t=0}^{\ln(1+\frac{P_i}{\sum_{j=i+1}^{M} P_j})} \left(1 - F_{c_i}\Big(\frac{1}{\frac{P_i}{e^t - 1} - \sum_{j=i+1}^{M} P_j}\Big)\right) dt. \tag{6.22}$$

To make a fair comparison between NOMA and conventional OMA, i.e., OFDMA in this study, the coverage probability and average achievable rate when using OMA are also presented. The result for a randomly chosen UE using OMA is published in [3], while the result provided here is for each UE out of M UEs in a cell, which can be understood as a decomposition of the result in [3]. The mean value is given as $\frac{\sum_{i=1}^{M} \tau_i}{M}$. Each UE in OMA is

assumed to be assigned an equal amount of bandwidth and allocated with the same downlink transmission power. The SIR expression, coverage probability and average achievable rate of UE_i using OMA can be acquired by making some simple modification on the previous NOMA analytical results. Thus in the following, the results are given directly without going through the details on derivations.

$$SIR_i^{OMA} = \frac{h_i r_i^{-\alpha} P_{total}/M}{\sum_{j\in\Phi/b_o} g_j R_{j,i}^{-\alpha} P_{total}/M} = c_i P_{total}, \tag{6.23}$$

$$\mathbb{P}[SIR_i^{OMA} > T] = 1 - F_{c_i}(\frac{T}{P_{total}}), \tag{6.24}$$

$$\tau_i^{OMA} = \frac{1}{M}\int_{t>0} \big(1 - F_{c_i}(\frac{e^t - 1}{P_{total}})\big)dt. \tag{6.25}$$

6.3 Numerical Evaluation

Both simulation results and analytical results are presented in this section. The performance of NOMA and OFDMA are compared under various settings. For OFDMA, it is assumed that the frequency resources are allocated equally to two UEs hence each of them will have 0.5 frequency resource as the overall bandwidth is normalized to 1. $\epsilon \in (0.5, 1)$ is used to represent the relationship between P_1 and P_2 in the 2-UE case, i.e., $P_1 = \epsilon P_{total}$ and $P_2 = (1-\epsilon)P_{total}$. $\alpha = 4$ is used in this section.

Figure 6.2 presents the coverage probability for NOMA UEs and OFDMA UEs. The analytical results match simulation results tightly. From the curves, it is clear that there is a trade-off between the performance of UE_1 and UE_2 when changing the value of ϵ. When comparing NOMA and OFDMA, for each UE, its coverage probability in the NOMA mode is always worse than its coverage probability in the OFDMA mode due to extra NOMA interference as well as due to a smaller transmission power for the NOMA UE. However, the advantage of NOMA can be observed from the average achievable rate as shown in Figure 6.3, which clearly shows that NOMA can achieve a much higher overall sum rate than OFDMA in the most scenarios. The impact of power allocation on NOMA is further investigated by changing ϵ. The average achievable rate under NOMA has an intersection

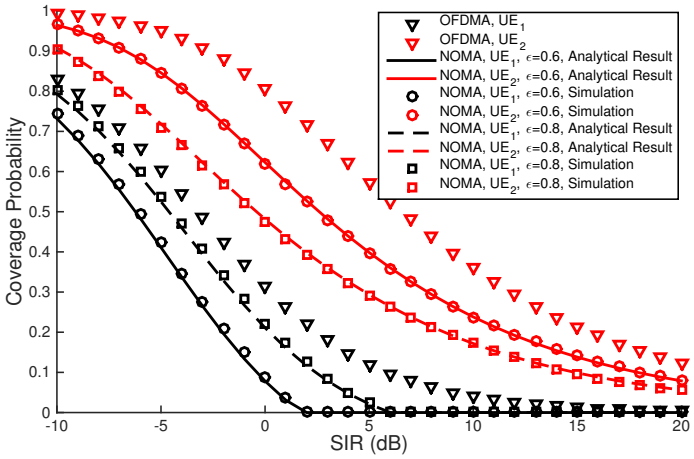

Fig. 6.2: Coverage probability for OFDMA UE and NOMA UE with different ϵ

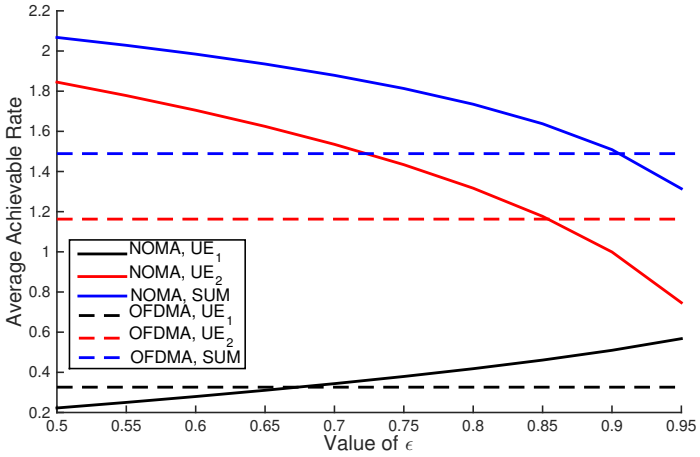

Fig. 6.3: Average Achievable Rate for OFDMA UE and NOMA UE with different ϵ

with that under OFDMA for both UE_1 and UE_2 and the intersecting values of ϵ for UE_1 and UE_2 are different. Also one can observe that when $\epsilon \in (0.655, 0.85)$, both UE_1 and UE_2 under NOMA outperform their respective average achievable rate under OFDMA. These observations are useful for seeking the optimal power allocation scheme aiming at different objectives, i.e., total throughput or user fairness.

In Figure 6.4, the impact of imperfect SIC is investigated with simulation results. The error propagation model proposed in [69] is used to model the impact caused by imperfect SIC in NOMA. The degree of SIC error at UE_i is presented by ρ, which is the percentage of inter-user interference that fails to be decoded. For instance, the SIR for UE_2 considering imperfect SIC can be expressed as $SIR_2 = \frac{h_2 r_2^{-\alpha} P_2}{I_2 + \rho h_2 r_2^{-\alpha} P_1}$. From Figure 6.4, even 1% unsuccessful decoding will result in more than 10% degradation on average achievable rate. And if ρ reaches 10%, NOMA throughput gain completely disappears regardless of ϵ settings. From this observation, one can conclude that failing to eliminate inter-user interference is fatal to NOMA and can be a challenging issue for implementing NOMA in practice.

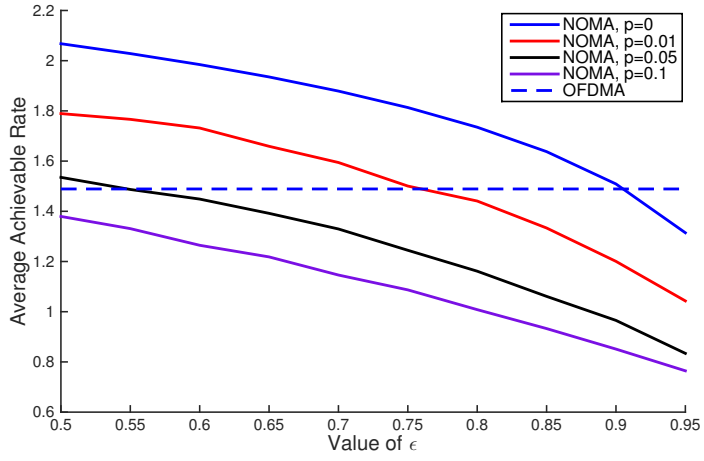

Fig. 6.4: Average Achievable Rate for NOMA UE with Imperfect SIC

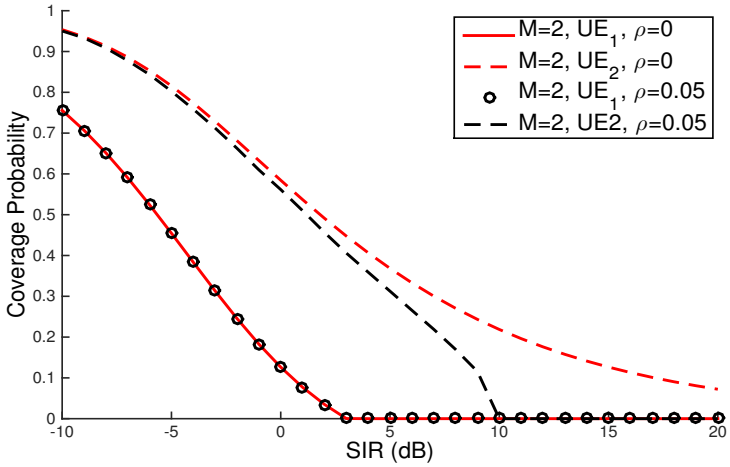

2-UE NOMA

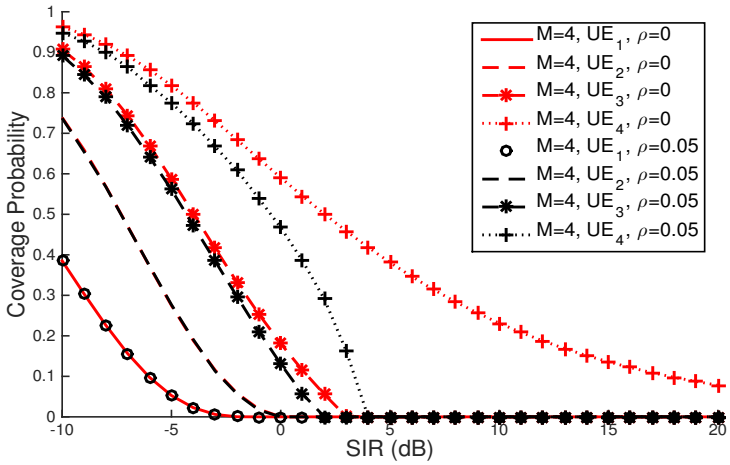

4-UE NOMA

Fig. 6.5: Coverage Probability for 4-UE and 2-UE NOMA with and without Imperfect SIC

In Figure 6.5, the impact of imperfect SIC on the coverage probability for the 4-UE and 2-UE NOMA scenarios is investigated. Simulation results are used for comparison. In each NOMA scenario ($M = 2,\ 4$), UE_i is allocated a power of $P_i = \frac{M-i+1}{\theta}$, where θ is a constant to guarantee $\sum_{i=1}^{M} P_i = P_{total}$. Note that UE_1 is immune to imperfect SIC as it does not need to process any interference cancellation. From Figure 6.5, one can observe that UE_M, which comes the last in the decoding order, suffers the most from imperfect SIC as it has the most residual interference if a certain percentage of NOMA inter-user interference, i.e., $\rho \sum_{j=1}^{M-1} P_j$, fails to be decoded. Moreover, P_M is the smallest power among $\{P_i\}$ based on the NOMA power allocation principle and hence makes UE_M even more vulnerable to additional interference. From Figure 6.5 one can also observe that the impact of imperfect SIC is more significant as M increases. This fact can be observed more clearly from the achievable rate in Figure 6.6. The throughput gain of NOMA over OFDMA degrades faster as M increases.

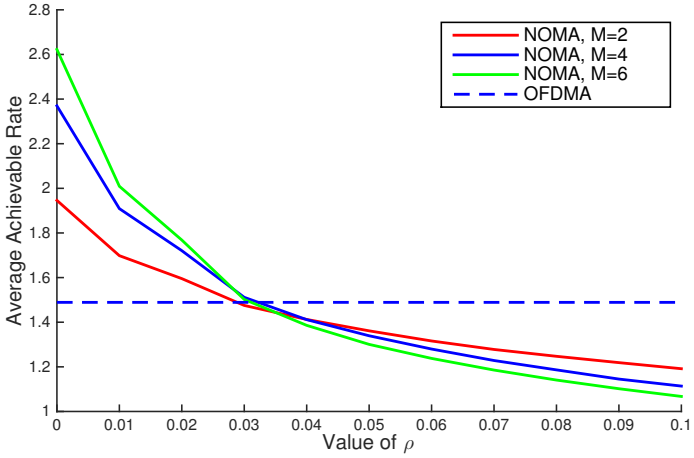

Fig. 6.6: Average Achievable Rate for 2-UE, 4-UE and 6-UE NOMA with different SIC error ρ

6.4 Conclusion

In this chapter, the performance of NOMA on the coverage probability and the average achievable rate is evaluated by using stochastic geometry method. The analysis explicitly considers inter-cell interference in the model and provides results in a tractable form. The analytical study considers a general M-UE NOMA scheme with flexible power allocation among M UEs. The analytical study is validated by simulation results. The study shows that NOMA, in general, will degrade UE SIR performance but improves overall system throughout, especially when the NOMA SIC error is low. The work in this chapter builds a general mathematical framework to evaluate more advanced NOMA schemes in the future.

CHAPTER 7

Uplink Non-Orthogonal Multiple Access with Fractional Power Control

To perform uplink NOMA successfully, the received signal of each user equipment (UE) within a NOMA group at base station needs to be decodable. On the other hand, fractional power control (FPC) is widely applied in the existing wireless networks to mitigate inter-cell interference by giving cell center and cell edge users different target receiving signal power levels. NOMA can exploit this difference in the received powers and group cell edge UEs and cell center UEs into a NOMA group so that further spectrum efficiency can be realized. In this chapter, an analytical framework for uplink NOMA with FPC is developed and performance on the system is evaluated in terms of coverage and average user achievable rate. The analysis of an OMA scheme with FPC is also provided for comparison. The analytical results are validated by simulations. The performance study demonstrates that NOMA with FPC can bring considerable capacity gain compared to OMA with FPC.

7.1 Related Works and Contributions

The key issue of using uplink NOMA is how to ensure that the received signal powers from different UEs have sufficient disparity so that SIC process at the BS can decode them in the power domain [63]. The normal uplink power control used in an OMA system such as LTE targets at the same arrived power level at BS and hence it is not suitable for NOMA, which needs disparity on the received power levels. Authors in [63] proposed a power back-off scheme, in which the arrived power of each UE is gradually degraded with certain step size. Before the content of this chapter is published in [70], [63] is the only one that focuses on evaluating the performance of uplink NOMA by using the stochastic geometry method. However, inter-cell interference is not considered in [63] and the power control scheme proposed therein needs extra signaling to allocate power for UEs. In this chapter, FPC based NOMA is proposed and the analytical model is formulated using stochastic geometry

to evaluate the performance of the proposed scheme. FPC, which is widely applied in the existing wireless networks to mitigate inter-cell interference [71], can result in diverse arrived powers at BS and hence can be exploited to facilitate NOMA. As the complexity of SIC scales at least linearly with the number of the users that are involved in a transmission [64], NOMA with 2 or 3 simultaneously multiplexed users is practical in reality [65]. Therefore, this chapter focuses on the NOMA study with 2 UEs forming a NOMA pair, whereas the analysis can be extended to a general NOMA case.

7.2 System Model

This chapter considers a multi-cell uplink system that uses NOMA and FPC. The typical BS under analysis is termed as BS_0 and it locates at the center of a disc with a radius R. UEs associated with BS_0 are uniformly distributed in the disc. The distance between a UE to BS_0 is denoted by r. The probability density function (PDF) of r is expressed as $f_r(r) = \frac{2r}{R^2}, r \in (0, R)$. Among all UEs associated with BS_0, two UEs UE_i, $i \in \{1, 2\}$ are selected to form a NOMA pair as shown in Fig. 7.1. UE_1 represents a user that is close to cell center and whose distance to BS_0 is less than R_1, $R_1 \in (0, R)$. UE_2 represents a user that locates close to cell edge and whose distance to BS_0 is greater than R_2, $R_2 \in (R_1, R)$. Denoting the transmitting distance from UE_i to BS_0 as r_i, the PDF of r_1 is $f_{r_1}(r_1) = \frac{2r_1}{R_1^2}, r_1 \in (0, R_1)$ and the PDF of r_2 is $f_{r_2}(r_2) = \frac{2r_2}{R^2 - R_2^2}, r_2 \in (R_2, R)$. The system resources are partitioned into a number of orthogonal equal-sized sub-bands and the bandwidth of each sub-band is normalized to 1. There is no interference among sub-bands in each cell. Due to frequency reuse one, there exists inter-cell interference. This chapter focuses on the analysis and performance evaluation of applying FPC based NOMA on uplink. Although the analysis assumes that each NOMA group consists of two users, this work can be generalized to NOMA with $K (K > 2)$ users.

The locations of interfering UEs in other cells using the same sub-band are assumed to follow a 2-D homogeneous Poisson Point Process (PPP) Φ with a density λ. By assuming the interfering UEs have the same density as the UEs in the typical cell under analysis, one can set $\lambda = \frac{2}{\pi R^2}$. The distance from an interfering UE_j, $j \in \Phi$, to its associated BS is

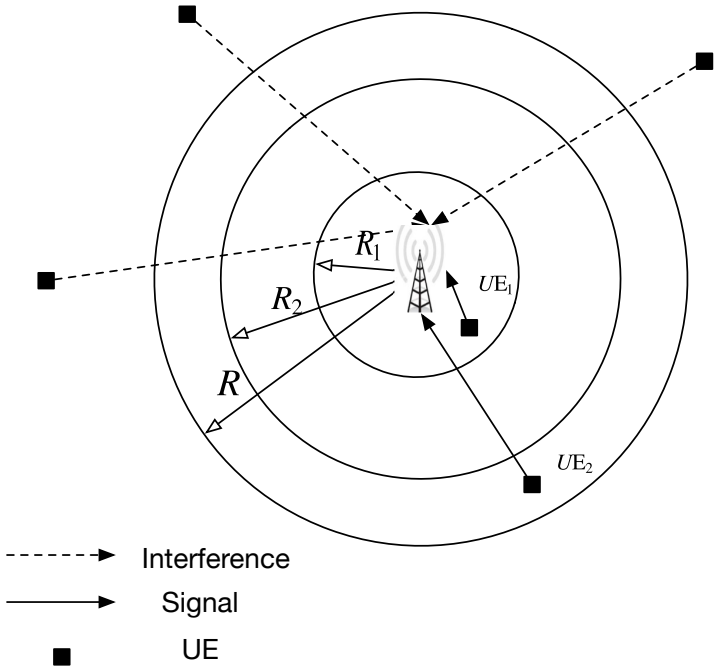

Fig. 7.1: System Model

denoted as l_j and the distance from UE_j to BS_0 is denoted as $r_{j,0}$. It is assumed that $\{l_j\}$ are independent and identically distributed (i.i.d.) and the PDF of l_j is $f_{l_j}(l_j) = \frac{2l_j}{R^2}, l_j \in (0, R)$, which is the same as r.

In this chapter, the general channel model is composed of path-loss and Rayleigh fading. The Rayleigh fading gain follows an exponential distribution with mean 1. It is assumed that Rayleigh fading distribution of all the channels is i.i.d.. The channel gain from UE_i to BS_0 can be expressed as $r_i^{-\alpha} h_i$, where $\alpha > 2$ is the path-loss exponent and $h_i \sim \exp(1)$ denotes Rayleigh fading gain. With FPC on the uplink, the transmit power of UE_i is expressed as $P_i = r_i^{\beta\alpha}$, where $\beta \in [0, 1]$ is a fractional power control parameter. The case that the required transmit power exceeds the maximum UE hardware capacity occurs rarely and is not considered in this chapter. If $\beta = 0$, no uplink power control is performed and all UEs transmit at the same power level. If $\beta = 1$, the path loss is completely compensated for all the UEs so that all the UEs should have the same target received power level at BS.

$0 < \beta < 1$ partially compensates the path-loss for UEs and the received power level at BS for each UE is a function of its path-loss. A UE closer to the BS will have a higher target received power level than a UE further away from the BS. Thus FPC allows cell center UEs to achieve a higher data rate than the UEs at cell edge so that overall higher system throughput is obtained with a tradeoff on the cell edge UE performance. SIC in NOMA needs different power levels to decode a composite signal, which actually is made possible by FPC. In this chapter, the nature of FPC is explored, i.e., cell center and cell edge UEs have different levels of received powers at BS. From that perspective, a smaller value of β can be more beneficial to the SIC performance at BS.

7.3 Uplink FPC with NOMA Transmission

With FPC the received uplink power of UE_i can be expressed as $h_i r_i^{-\alpha} P_i = h_i r_i^{(\beta-1)\alpha}$. As $\beta \in [0, 1]$, the received power is inversely proportional to distance r_i. Although $r_2 > r_1$, the received power of UE_2 may occasionally be greater than UE_1 due to small scale fading. In this chapter, it assumes that the values of R_1 and R_2 are sufficiently apart so that the received power of UE_1 is always greater than UE_2. In that case, UE_1 and UE_2 form a NOMA pair with UE_1 as the strong user since FPC gives UE_1 a higher received power. Based on the principle of NOMA, the SIC receiver is carried out at BS_0 to decode the superimposed signal. In the 2-UE NOMA case, the signal from UE_1, which has a stronger received power, is decoded first by treating the received signal from UE_2 as interference. After the first round SIC decoding and assuming SIC successfully decodes UE_1's signal with no error, BS_0 removes UE_1's signal from the composite received signal and then decodes UE_2's signal without inter-user interference. The post-processing signal-to-interference-plus-noise ratio (SINR) of UE_1 and UE_2 after SIC can be respectively expressed as

$$SINR_1 = \frac{h_1 r_1^{(\beta-1)\alpha}}{h_2 r_2^{(\beta-1)\alpha} + I + \sigma^2}, \quad SINR_2 = \frac{h_2 r_2^{(\beta-1)\alpha}}{I + \sigma^2},$$

where $I = \sum_{j \in \Phi} g_j r_{j,0}^{-\alpha} P_j$ denotes the inter-cell interference received at BS_0. g_j and P_j are the Rayleigh fading gain of each interfering channel and the transmit power of UE_j

respectively. σ^2 is a constant denoting the power of additive noise. In this chapter, the performance of uplink NOMA with FPC is evaluated in two metrics: coverage probability and average achievable rate.

7.3.1 Coverage probability for NOMA with FPC

The coverage probability is defined as $\bar{F}_i(T) = \mathbb{P}[SINR_i > T]$. It represents the probability that the instantaneous SINR of UE_i is greater than a certain threshold T. The coverage probability is the complementary cumulative distribution function (CCDF) of a UE's SINR. By following the work in [3], the coverage probability of $SINR_1$ is evaluated as

$$\begin{aligned}
\bar{F}_1(T) &= \mathbb{P}[SINR_1 > T] \\
&= \mathbb{E}_{r_1}\Big[\mathbb{P}\Big[\frac{h_1 r_1^{(\beta-1)\alpha}}{h_2 r_2^{(\beta-1)\alpha} + I + \sigma^2} > T | r_1\Big]\Big] \\
&= \int_0^{R_1} \mathbb{P}\Big[h_1 > T r_1^{(1-\beta)\alpha}(h_2 r_2^{(\beta-1)\alpha} + I + \sigma^2) | r_1\Big] f_{r_1}(r_1) dr_1 \\
&\overset{(a)}{=} \int_0^{R_1} \exp(-T r_1^{(1-\beta)\alpha}(h_2 r_2^{(\beta-1)\alpha} + I + \sigma^2)) \frac{2r_1}{R_1^2} dr_1 \\
&= \int_0^{R_1} \mathcal{L}_I(T r_1^{(1-\beta)\alpha}) \exp(-T r_1^{(1-\beta)\alpha}\sigma^2) \\
&\qquad \cdot \underbrace{\mathbb{E}_{h_2,r_2}[e^{-h_2 r_2^{(\beta-1)\alpha} r_1^{(1-\beta)\alpha} T}]}_{Q_1} \frac{2r_1}{R_1^2} dr_1,
\end{aligned} \tag{7.1}$$

where (a) uses $h_1 \sim \exp(1)$ and $f_{r_1}(r_1) = \frac{2r_1}{R_1^2}, r_1 \in (0, R_1)$. $\mathcal{L}_I(s) = \mathbb{E}_I[e^{-sI}]$ is the Laplace transform of random variable I evaluated on s. The full expression of $\mathcal{L}_I(s)$ is given by

$$\begin{aligned}
\mathcal{L}_I(s) &= \mathbb{E}_{\Phi,g_j,P_j}\Big[\exp(-s\sum_{j\in\Phi} g_j r_{j,0}^{-\alpha}P_j)\Big] \\
&= \mathbb{E}_{\Phi}\Big[\prod_{j\in\Phi}\mathbb{E}_{g_j,P_j}[\exp(-sg_j r_{j,0}^{-\alpha}P_j)]\Big] \\
&\overset{(a)}{=} \exp\Big(-2\pi\lambda\mathbb{E}_{g,P}[\int_R^{\infty}\big(1-\exp(-sgv^{-\alpha}P)]\big)vdv\Big) \\
&\overset{(b)}{\approx} \exp\Big(-2\pi\lambda\mathbb{E}_{g,P}[\int_R^{\infty}-\sum_{n=1}^{N}\frac{(-sPgv^{-\alpha})^n}{n!}vdv]\Big) \\
&= \exp\Big(2\pi\lambda\sum_{n=1}^{N}\frac{1}{n!}\mathbb{E}[P^n]\mathbb{E}[g^n](-s)^n\int_R^{\infty}v^{1-n\alpha}dv\Big). \qquad (7.2)
\end{aligned}$$

In the above derivations, (a) uses the probability generating functional (PGFL) of PPP [9], which states that $\mathbb{E}[\prod_{x\in\Phi}f(x)] = \exp(-\lambda\int_{\mathbb{R}^2}(1-f(x))dx)$. (b) uses Taylor series for e^x at 0, which is $e^x = \sum_{n=1}^{\infty}\frac{x^n}{n!}$, to approximate the expression of integration. Instead of using ∞ in Taylor series, a finite number N is used for approximation in Taylor series to tradeoff the computational complexity and accuracy. As N increases, the accuracy of the approximation increases. The two expectation and one integration in the last step of (7.2) are calculated in the following. $\mathbb{E}[g^n] = n$ as $g \sim \exp(1)$. $\int_R^{\infty}v^{1-n\alpha}dv = \frac{R^{2-n\alpha}}{n\alpha-2}$. $\mathbb{E}[P^n]$ is given below as

$$\begin{aligned}
\mathbb{E}[P^n] &= \int_0^R l^{n\beta\alpha}f_l(l)dl \\
&= \int_0^R l^{n\beta\alpha}\frac{2l}{R^2}dl \\
&= \frac{2R^{n\beta\alpha}}{n\beta\alpha+2}.
\end{aligned}$$

Consequently, the closed form approximation of $\mathcal{L}_I(s)$ can be derived.

$$\mathcal{L}_I(s) \approx \exp\Big(2\pi\lambda\sum_{n=1}^{N}\frac{2R^{2+n\beta\alpha-n\alpha}}{(n\beta\alpha+2)(n\alpha-2)(n-1)!}(-s)^n\Big), \qquad (7.3)$$

which is a linear combination of exponential functions of s. When $N = 1$, the complexity can be significantly reduced as (7.3) can be further simplified to

$$\mathcal{L}_I(s) \overset{N=1}{\approx} \exp\Big(- 4\pi\lambda s \frac{R^{2+(\beta-1)\alpha}}{(\beta\alpha+2)(\alpha-2)}\Big). \tag{7.4}$$

This is a single exponential function of s. The impact of N on the accuracy of approximation will be investigated in the performance study, based on which one can see that $N = 1$ is sufficient to achieve a good accuracy under the concerned scenario. Another factor Q_1 can be expressed as follows:

$$\begin{aligned} Q_1 &= \mathbb{E}_{r_2}\Big[\frac{1}{1+T\big(\frac{r_1}{r_2}\big)^{(1-\beta)\alpha}}\Big] \\ &= \int_{R_2}^{R} \frac{1}{1+T\big(\frac{r_1}{r_2}\big)^{(1-\beta)\alpha}} f_{r_2}(r_2) dr_2 \\ &= \frac{1}{R^2-R_2^2}\int_{R_2^2}^{R^2} \frac{1}{1+T\Big(\frac{r_1^{(1-\beta)\alpha}}{x^{\frac{(1-\beta)\alpha}{2}}}\Big)} dx. \end{aligned} \tag{7.5}$$

Here again uses the fact that $h_2 \sim \exp(1)$ and in last step it uses $x = r_2^2$. By substituting $s = Tr_1^{(1-\beta)\alpha}$ back into (7.3) and combining it with (7.5), one can get the complete expression of $\bar{F}_1(T)$ as

$$\begin{aligned} \bar{F}_1(T) &= \int_{r_1=0}^{R_1} \mathcal{L}_I(Tr_1^{(1-\beta)\alpha}) \exp(-Tr_1^{(1-\beta)\alpha}\sigma^2) \\ &\quad \cdot \frac{1}{R^2-R_2^2}\int_{x=R_2^2}^{R^2} \frac{1}{1+T\Big(\frac{r_1^{(1-\beta)\alpha}}{x^{\frac{(1-\beta)\alpha}{2}}}\Big)} \frac{2r_1}{R_1^2} dx dr_1 \\ &= \frac{1}{R_1^2(R^2-R_2^2)}\int_{y=0}^{R_1^2} \mathcal{L}_I(Ty^{\frac{(1-\beta)\alpha}{2}}) \exp(-Ty^{\frac{(1-\beta)\alpha}{2}}\sigma^2) \\ &\quad \cdot \int_{x=R_2^2}^{R^2} \frac{1}{1+T\Big(\frac{y}{x}\Big)^{\frac{(1-\beta)\alpha}{2}}} dx dy. \end{aligned} \tag{7.6}$$

In last step it uses $y = r_1^2$. The calculation of (7.6) involves two tiers of integration, which can be computed conveniently by using software tools like MATLAB.

Similar to the coverage probability of UE_1, the coverage probability of UE_2 can be derived as

$$\begin{aligned}
\bar{F}_2(T) &= \mathbb{P}[SINR_2 > T] \\
&= \mathbb{E}_{r_2}\Big[\mathbb{P}\Big[\frac{h_2 r_2^{(\beta-1)\alpha}}{I+\sigma^2} > T|r_2\Big]\Big] \\
&= \int_{R_2}^{R} \mathbb{P}\Big[h_2 > T r_2^{(1-\beta)\alpha}(I+\sigma^2)|r_2\Big] f_{r_2}(r_2) dr_2 \\
&= \int_{R_2}^{R} \exp(-T r_2^{(1-\beta)\alpha}(I+\sigma^2)) \frac{2r_2}{R^2-R_2^2} dr_2 \\
&= \frac{1}{R^2-R_2^2} \int_{R_2^2}^{R^2} \mathcal{L}_I(T x^{\frac{(1-\beta)\alpha}{2}}) \exp(-T x^{\frac{(1-\beta)\alpha}{2}} \sigma^2) dx, \qquad (7.7)
\end{aligned}$$

where $\mathcal{L}_I(s)$ is given in (7.3).

7.3.2 Coverage probability for OMA with FPC

To make a comparison between NOMA and conventional OMA, i.e., OFDMA in this study, the coverage probability of each UE when using OMA with FPC is presented in this section. For a fair comparison with NOMA, the bandwidth of each sub-band is equally partitioned between UE_1 and UE_2 for OMA. Since the bandwidth of each sub-band is normalized to 1, the resource allocated to each UE is $\frac{1}{2}$. It is assumed that the transmit powers of UE_1 and UE_2 are the same as in NOMA. The SINRs of UE_1 and UE_2 when using OMA with FPC are $SINR_1^{OMA}$ and $SINR_2^{OMA}$ respectively.

$$\begin{aligned}
SINR_1^{OMA} &= \frac{h_1 r_1^{(\beta-1)\alpha}}{\frac{1}{2}(I+\sigma^2)}, \\
SINR_2^{OMA} &= \frac{h_2 r_2^{(\beta-1)\alpha}}{\frac{1}{2}(I+\sigma^2)}.
\end{aligned}$$

The coverage probability when using OMA with FPC is denoted as $\bar{F}_i^{OMA}(T) = \mathbb{P}[SINR_i^{OMA} > T]$ and it can be derived by following the same process in NOMA. Thus

the final expressions are provided in the following by skipping the derivation details.

$$\begin{aligned}\bar{F}_1^{OMA}(T) &= \mathbb{P}[SINR_1^{OMA} > T] \\ &= \frac{1}{R_1^2}\int_0^{R_1^2} \mathcal{L}_I(\frac{T}{2}x^{\frac{(1-\beta)\alpha}{2}})e^{-\frac{T}{2}\sigma^2 x^{\frac{(1-\beta)\alpha}{2}}}dx, \qquad (7.8)\\ \bar{F}_2^{OMA}(T) &= \mathbb{P}[SINR_2^{OMA} > T] \\ &= \frac{1}{R^2 - R_2^2}\int_{R_2^2}^{R^2} \mathcal{L}_I(\frac{T}{2}x^{\frac{(1-\beta)\alpha}{2}})e^{-\frac{T}{2}\sigma^2 x^{\frac{(1-\beta)\alpha}{2}}}dx. \qquad (7.9)\end{aligned}$$

7.3.3 Average achievable data rates

Based on the coverage probability, one can compute the average achievable rates of UE_1 and UE_2 for both NOMA and OMA scenarios by using Shannon capacity formula, i.e. $\ln(1 + SINR)$. SINR distribution shows the system coverage performance while the achievable data rates can better tell the system spectrum efficiency. Notice that the average achievable rate given here is in the unit of nats/Hz (1 bit = ln(2) =0.693 nats). Denoted by τ_i the average achievable rate of UE_i when using NOMA, $i \in \{1, 2\}$, the method of computing τ_i can be found in [3] as

$$\begin{aligned}\tau_i &= \mathbb{E}[ln(1 + SINR_i)] \\ &\overset{(a)}{=} \int_0^{\infty} \mathbb{P}[\ln(1 + SINR_i) > t]dt \\ &= \int_0^{\infty} \bar{F}_i(e^t - 1)dt, \qquad (7.10)\end{aligned}$$

where (a) follows $\mathbb{E}[X] = \int_{t>0} \mathbb{P}(X > t)dt$ for a positive random variable X. Denoted by τ_i^{OMA}, the average achievable rate of UE_i when using OMA can be computed in the same way as above. Notice that when using OMA, UE_i can only use half of the resources in each sub-band.

$$\tau_i^{OMA} = \frac{1}{2}\int_0^{\infty} \bar{F}_i^{OMA}(e^t - 1)dt. \qquad (7.11)$$

7.4 Numerical Evaluation

In this section, the analytical results are first validated by simulations. The impact of control parameter N on the accuracy of the derivation approximation are discussed. Afterward the performance of NOMA with FPC is compared with the performance of OFDMA with FPC. The following parameter values are used in performance evaluation, $R = 100$, $R_1 = 20$ and $R_2 = 80$. The target SNR with full path-loss compensation, i.e., $\frac{r^{(\beta-1)\alpha}}{\sigma^2} \overset{\beta=1}{=} \frac{1}{\sigma^2}$, is 20 dB unless otherwise specified. The path-loss exponent α is set as 3.78.

Figure 7.2 shows the comparison between the analytical results and simulations. One can see that with Taylor series approximation parameter N set at 1, 3, and 5, the analytical results get closer and closer to the simulation results. $N = 1$ is sufficient to provide an accurate approximation when β is less than 0.8. Recall that in (7.2) $\exp(Q_2)$ is approximated to its Taylor series at 0 where $Q_2 = -sgv^{-\alpha}P$. This approximation is tight when the value of Q_2 is close to 0. By looking into the composition of $Q_2 = -gT(\frac{r_1}{r_{0,j}})^{\alpha}(\frac{l}{r_1})^{\beta\alpha}$, one can find that with a smaller β the value of Q_2 is closer to 0 and a higher accuracy is achieved. To make the received powers of NOMA UEs more distinguishable, a smaller value of β is preferred. Thus $N = 1$ is sufficient to provide an accurate analytical result when applying FPC in NOMA. Since the analytical results and Simulation results always match each other very well, only the analytical results are presented in the rest figures.

Figure 7.3 compares the coverage probability of NOMA with that of OFDMA. By comparing Figure 7.3(a) and Figure 7.3(b), one can observe that the gap between the coverage probabilities of UE_1 and UE_2 increases as the value of β decreases, which indicates that a smaller value of β does make the received power more distinguishable between UE_1 and UE_2. Moreover, one can see that the coverage probability of NOMA is always worse than that of OFDMA as NOMA introduces extra NOMA interference between UE_1 and UE_2. NOMA UEs are also subject to more inter-cell interference from other cells than OFDMA UEs as in other cells each co-channel sub-band serves two UEs when NOMA is used.

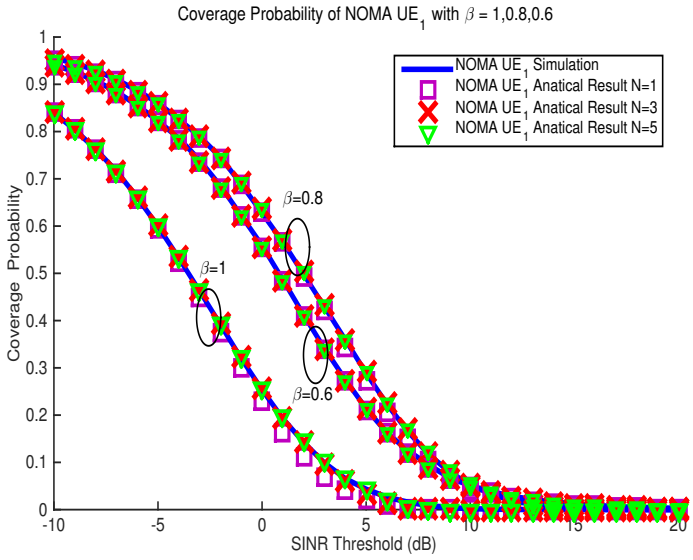

NOMA UE_1

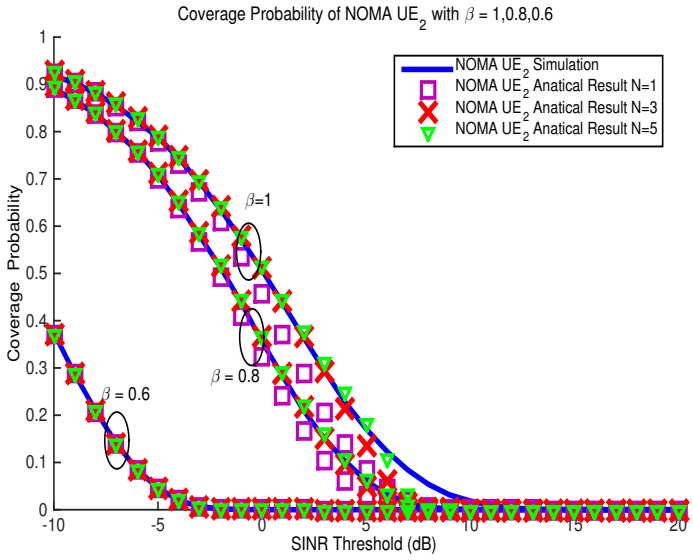

NOMA UE_2

Fig. 7.2: Coverage probability for NOMA UE_1 and UE_2

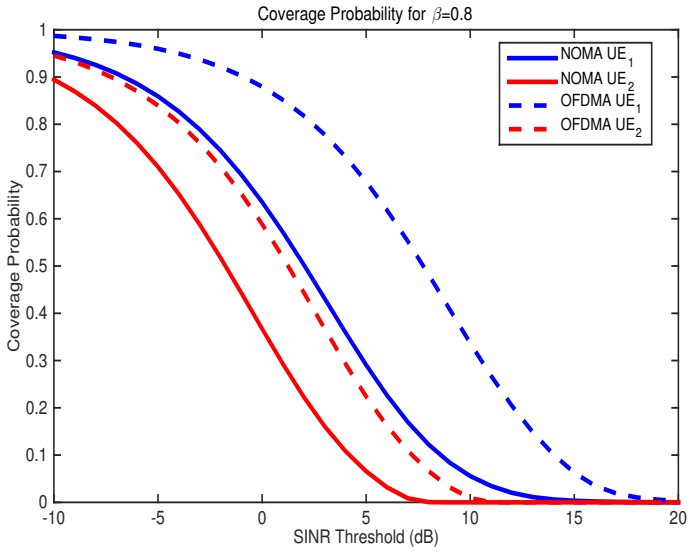

$\beta = 0.8$

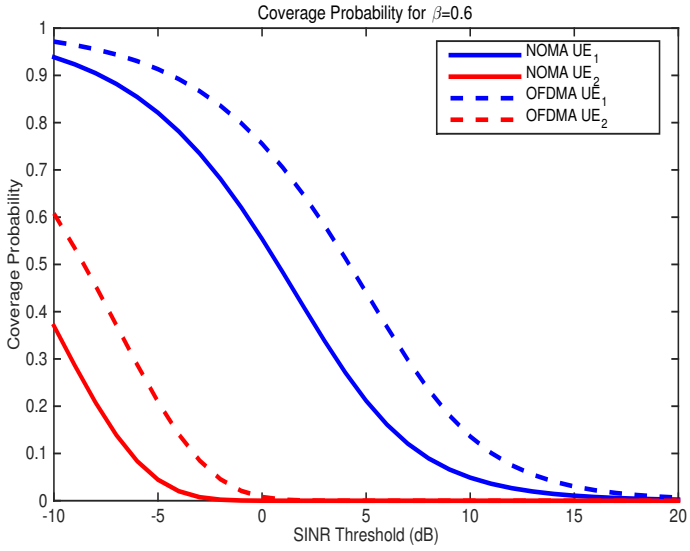

$\beta = 0.6$

Fig. 7.3: Coverage probability for NOMA when $\beta = 0.8, 0.6$

Figure 7.4 compares the sum achievable rate between NOMA and OFDMA with different β values. It can be observed that in the low SNR region, i.e., $\frac{1}{\sigma^2}$ is small, a higher β value can lead to a higher achievable sum rate. When SNR is low, the system is more towards noise limited. Thus a smaller β in the FPC algorithm decreases the UE transmit power and will make noise even more overwhelming, which in turn decreases the achievable data rate. In the high SNR region, i.e., $\frac{1}{\sigma^2}$ is high, the system turns to interference limited. $\beta = 0.7$ can support a higher achievable rate than $\beta = 0.9$. By decreasing the value of β at high SNR, the throughput gain from cell center users exceeds the throughput loss from cell edge users so that the overall sum rate increases. Furthermore, with a smaller β, the difference between the cell center user received power level and cell edge user received power level becomes bigger, making the composite signals from NOMA UEs more distinguishable at BS. However, if β is too small, the overall sum rate becomes smaller. This can be seen by comparing the results from $\beta = 0.5$ and $\beta = 0.7$. With a too small β in FPC, the received powers of both cell center users and cell edge users become quite low so that the impact of noise becomes visible again. It is also observed that the gain of NOMA over OFDMA is more remarkable at high SNR region.

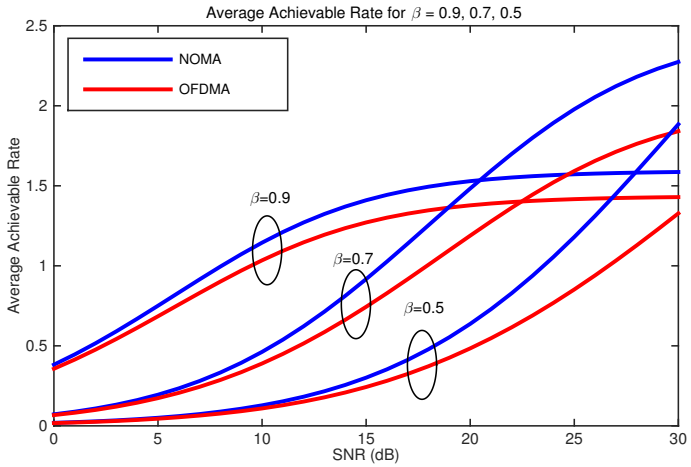

Fig. 7.4: Average Achievable Rate of NOMA and OFDMA, $\beta = 0.9, 0.7, 0.5$

In Figure 7.5 there is an optimal value of β for the average achievable rate under different SNR scenarios. Nevertheless, in uplink, it is not sufficient to determine the optimal value of β by only considering maximizing the sum rate. For instance, when SNR = 10 dB, the optimal value of β is 1 as shown in Figure 7.5. But $\beta = 1$ makes it difficult to split the composite received signal by SIC as the received power levels are the same for the two UEs in the same NOMA group when $\beta = 1$. The study in this chapter assumes a perfect SIC and there is no error propagation. If error propagation exists, the performance curves will be slightly different. Thus an appropriate metric to evaluate the diversity of arrived power is expected and the optimization of β by jointly considering both sum rate performance and arrived power diversity is an interesting problem.

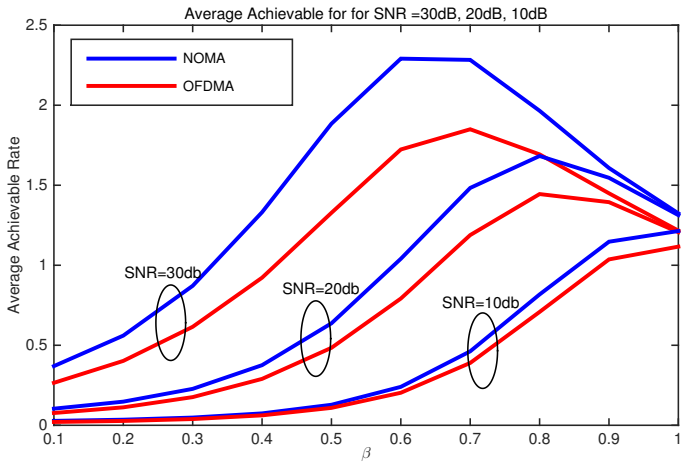

Fig. 7.5: Average Achievable Rate of NOMA and OFDMA, SNR=30 dB, 20 dB, 10 dB

7.5 Conclusion

In this chapter, the performance of uplink coverage probability and average achievable rate are evaluated by applying NOMA and fractional power control (FPC) together. FPC increases the diversity of the received power levels among cell center and cell edge users in order to gain a higher overall cell throughput. This nature also motivates the study to apply NOMA together with FPC so that cell edge and cell center users can be served as a NOMA group to further improve cell throughput. The study in this chapter shows that NOMA can achieve a much higher throughput than OMA by properly setting the fraction power control parameter. In the future work, it is expected to find or create an appropriate metric to evaluate the diversity of arrived power so that a joint optimization problem considering both system performance and diversity of arrived power can be formed and solved.

CHAPTER 8

Downlink and Uplink Non-Orthogonal Multiple Access in a Dense Wireless Network

In Chapter 6 & 7, stochastic geometry based analytical frameworks are developed for downlink and uplink NOMA respectively. However, the system models used in these two frameworks are different. For some research that jointly analyzes the performance of downlink and uplink NOMA system [72–74], a framework that is able to analyze the performance of both downlink and uplink NOMA on a single system model, is desired. Motivated by this fact, this chapter develops a complete multi-cell NOMA framework for analysis and performance evaluation on both uplink and downlink. Similar to the work presented in Chapter 6 & 7, the analytical framework developed in this chapter also take inter-cell interference into consideration, which is a crucial feature of a dense network. The downlink part of the content in this chapter is based on that in Chapter 6, however, with the following improvement.

1. SIC error propagation during the decoding process is considered in the framework. Moreover, outage probability is added in the analysis.

2. In Chapter 6, the members within a NOMA pair are randomly selected from all UEs. In this chapter, a selective pairing scheme is proposed and analyzed. The comparison between random pairing and selective pairing is also presented.

The outage probability is used more frequently in the papers related to NOMA. The detailed definition of outage probability and the advantage of using that will be clear in the later context. The uplink part of the content in this chapter is different from that in Chapter 7.

8.1 System Model

This chapter considers a dense multi-cell wireless system that supports NOMA on both downlink and uplink. Both BS and UE are equipped with one antenna. The set of BSs

denoted as Φ_b, are deployed in the Euclidean plane according to a PPP model with a density of λ_b. The system assumes a frequency reuse factor 1, hence the same frequency resources are used in all the cells. The radio resources are partitioned into a number of sub-bands and resources are allocated in the unit of sub-band. For notation simplicity, the bandwidth of each sub-band is normalized to 1 and the analysis of user performance focuses on a typical sub-band by assuming flat fading channels across sub-bands. The NOMA study in this paper assumes a group size of two. Existing results show that NOMA with more than two UEs may provide a better performance gain [66]. However, considering processing complexity for SIC receivers, especially when SIC error propagation is considered, 2-UE NOMA is actually more practical in reality [65]. UE locations are assumed to follow another PPP Φ_u with a density λ_u. Φ_u is independent on Φ_b. It is assumed that $\lambda_u >> \lambda_b$ so that a sufficient number of UEs can always be found to form a NOMA group in each cell. A UE is associated with the nearest BS and is located in the Voronoi cell of its associated BS. NOMA system performance is analyzed on both downlink and uplink.

8.1.1 Downlink NOMA System Model

The downlink NOMA system is shown in Figure 8.1. Without loss of generality, the analysis is performed in a typical cell denoted as BS_0. Based on Slivnyak's Theorem [75], due to the stationarity of Φ_b, the typical cell can reflect the spatially averaged performance of the entire system. Two different pairing schemes are investigated in the downlink NOMA system. The first scheme is based on random pairing, in which 2 UEs are randomly selected to form a NOMA group. The second scheme is based on selective pairing. The first UE has a signal-to-interference-plus-noise ratio (SINR) above threshold T_1 and the second UE has an SINR below threshold T_2, $T_2 \leq T_1$. In both pairing schemes, UE with a better normalized channel gain is denoted as UE_1 and UE with a worse normalized channel gain is denoted as UE_2. The meaning of normalized channel gain is the same as defined in Chapter 6 and will be addressed again later.

The power allocation strategy for downlink NOMA can be classified into two categories, namely fixed power allocation and dynamic power allocation [65]. In a fixed power allocation

scheme, the downlink power allocated to a UE is predefined and remains unchanged [15]. In contrast, a dynamic power allocation adapts power allocation based on instantaneous channel information [65]. In this chapter, the fixed power allocation strategy is adopted due to the fact that it can achieve a suboptimal performance without excessive signaling overhead required by dynamic power allocation strategy [76, 77]. P_b denotes the total transmit power on a sub-band. The powers allocated to UE_1 and UE_2 can be expressed as $P_1^d = \epsilon P_b$ and $P_2^d = (1-\epsilon)P_b$ respectively, where $\epsilon \in (0, 0.5)$ is a NOMA power control parameter.

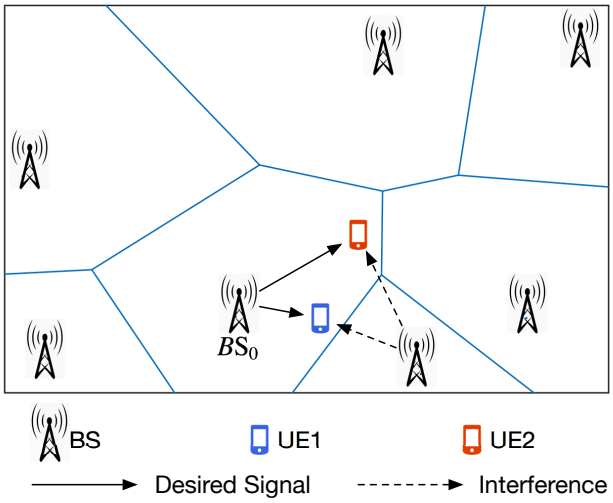

Fig. 8.1: The System model for downlink NOMA system. All the other cells generate inter-cell interference to UEs under analysis though only interference from one BS is noted on the graph to make graph succinct.

The transmitted signals to UE_1 and UE_2 are expressed as x_1 and x_2 respectively, with $\mathbb{E}[|x_i|^2] = 1$. Since UE_1 and UE_2 form a NOMA group, x_1 and x_2 are encoded as the composite signal at the BS [15],

$$x = \sqrt{P_1^d}x_1 + \sqrt{P_2^d}x_2. \tag{8.1}$$

Thus the received signal at $UE_i,\ i \in \{1,2\}$, can be represented as

$$y_i = \sqrt{h_i r_i^{-\alpha}} x + n_i, \tag{8.2}$$

where n_i denotes the additive noise plus inter-cell interference. As UE_1 has a better channel condition, UE_1 first decodes x_2 and removes it from the received composite signal y_1, based on which UE_1 can further decode x_1. UE_2 directly decodes x_2 by treating x_1 as interference. In reality, SIC decoding in the first step may not be successful and thus the error is carried over to the next level decoding, which is called SIC error propagation. The achievable rates of UE_1 and UE_2 on each sub-band in a downlink NOMA by considering SIC error are given as

$$\tau_1^d = \log_2\left(1 + \frac{h_1 r_1^{-\alpha} P_1^d}{I_1 + \beta h_1 r_1^{-\alpha} P_2^d}\right) = \log_2\left(1 + \frac{c_1 P_1^d}{\beta c_1 P_2^d + 1}\right), \tag{8.3}$$

and

$$\tau_2^d = \log_2\left(1 + \frac{h_2 r_2^{-\alpha} P_2^d}{I_2 + h_2 r_2^{-\alpha} P_1^d}\right) = \log_2\left(1 + \frac{c_2 P_2^d}{c_2 P_1^d + 1}\right). \tag{8.4}$$

h_i is the Rayleigh fading gain between BS_0 and UE_i and it follows an exponential distribution with mean 1, $i \in \{1,2\}$. It is assumed that all $h_i, \forall i$ are i.i.d. and are reciprocal on uplink and downlink. r_i is the distance between UE_i to BS_0. α is the path-loss exponent. $I_i = \sum_{j \in \Phi_b \setminus BS_0} g_{i,j} R_{i,j}^{-\alpha} P_b$ is the cumulative downlink inter-cell interference from all other BSs to UE_i, where $g_{i,j}$ is the Rayleigh fading gain from BS_j, $j \in \Phi_b \setminus BS_0$, to UE_i and it also follows an exponential distribution with mean 1. $\Phi_b \setminus BS_0$ represents the set of all BSs excluding BS_0. It is assumed that all $\{g_{i,j}\}$ are i.i.d. and independent on $\Phi_b \setminus BS_0$. $R_{i,j}$ is the distance from interfering BS_j to UE_i. The normalized channel gain $c_i = \frac{h_i r_i^{-\alpha}}{I_i}$ is defined as the complete channel gain including path-loss and fast fading normalized by inter-cell interference. $\beta \in [0,1]$ denotes the fraction of NOMA interference due to SIC error propagation [69]. Noise can be safely neglected in a dense interference-limited wireless system.

8.1.2 Uplink NOMA System Model

In the uplink, inter-cell interference comes from all the UEs in other cells sharing the same sub-band, as shown in Figure 8.2. When modeling inter-cell interference, it is assumed that the system is fully loaded and all the cells perform a 2-UE uplink NOMA with the same power control scheme. The locations of two UEs that form a NOMA group in each cell are randomly selected among UEs associated with that cell. For instance, there are N UEs in a single cell ($N >> 2$ as $\lambda_u >> \lambda_b$) and 2 out of N UEs in this cell can be randomly selected to form a NOMA group on the sub-band under consideration. One of these two UEs is treated as UE_1 and the other one is treated as UE_2. The locations of UE_1s in each cell form a distribution Φ_1 and the locations of UE_2s in each cell form a distribution Φ_2. Both Φ_1 and Φ_2 depend on Φ_b. However, as validated in many existing work [11, 78], Φ_1 and Φ_2 can be approximated as PPP with respective densities $\lambda_1 = \lambda_b$ and $\lambda_2 = \lambda_b$. The accuracy of this approximation can be validated by simulation results later. In the uplink, a receiver BS normally has much more capable hardware and advanced algorithms than a UE, so perfect SIC is assumed at BSs.

Distance-based proportional power control has been widely applied, in which the transmit power of UE_i is inversely proportional to distance, i.e., $P_0 * r_i^{\alpha}$. P_0 is the target received power and is set the same for all UEs. As the channel model consists of path-loss and Rayleigh fading, the actual received power at BS_0 is $P_0 * h_i$. Within a 2-UE NOMA group, UE with the higher Rayleigh fading gain is denoted as UE_1 and UE with the smaller Rayleigh fading gain is denoted as UE_2, $h_1 > h_2$. In this power control scheme, the diversity of the received power only depends on Rayleigh fading and all the UEs have the same averaged received power. Nevertheless, this level of difference on the received powers by using distance-based proportional power control may not be sufficient enough to distinguish UEs within the same NOMA group [63]. In Chapter 7, FPC is leveraged to address this problem. In this chapter, another scheme is proposed for this problem.

In this chapter, a revised power back-off scheme is used for uplink power control. The original power back-off scheme was proposed in [63]. In the revised version, a back-off step

ρ, $\rho \in (0, 1]$ is defined, and the transmit power of UE_2 is set as $P_2^u = \rho * P_0 * r_2^\alpha$. No back-off is applied to UE_1. Thus its power is set as $P_1^u = P_0 * r_1^\alpha$. The received powers of UE_1 and UE_2 are $P_0 * h_1$ and $\rho * P_0 * h_2$ respectively. Since $h_1 > h_2$, the received powers are more distinctive with $\rho < 1$. Notice that the original scheme in [63] applies back-off to the UE that has a longer transmit distance to save power. Due to the independence between path-loss and Rayleigh fading, in [63] the decoding order can be decided only when the UE that has a longer transmit distance also has a smaller Rayleigh fading gain, which may not be true in reality. In the revised scheme proposed here, UE_1 is always decoded first because back-off is applied based on the fading channel gain. Since a dense network is considered, the extreme case that the transmit power may exceed the UE's hardware capacity is not taken into account in this chapter.

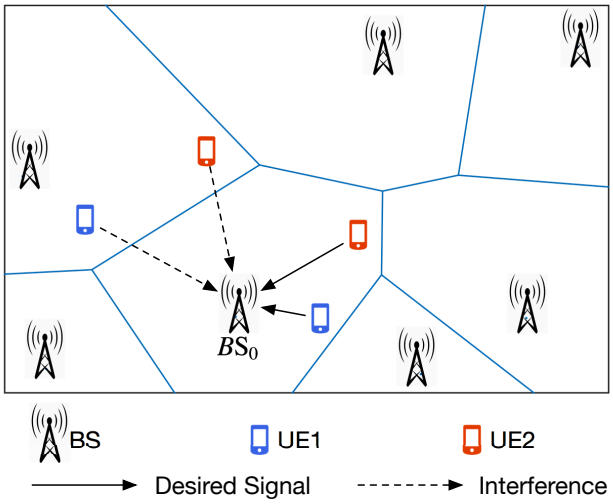

Fig. 8.2: The System model for uplink NOMA system. All the UEs in other cells using the same sub-band generate inter-cell interference to BS_0. Only interference from one cell is noted to make graph succinct.

Uplink NOMA allows 2 UEs to transmit on the same sub-band. The received signal at BS_0 using revised power back-off scheme is expressed as

$$y_0 = \sqrt{P_0 h_1} x_1 + \sqrt{\rho P_0 h_2} x_2 + w, \tag{8.5}$$

where w denotes the additive noise plus inter-cell interference. With SIC at BS, x_1 is decoded first by treating x_2 as interference. Afterwards, x_1 is removed from y_0 and then x_2 can be decoded. It is assumed that x_1 is always decoded first in this paper. Otherwise, the rate of UE_2 is extremely low. As a result, the achievable per sub-band rate of each UE in uplink NOMA are given as

$$\tau_1^u = \log_2\Big(1 + \frac{h_1}{\rho h_2 + I_{0,1} + I_{0,2} + \frac{\sigma^2}{P_0}}\Big), \tag{8.6}$$

$$\tau_2^u = \log_2\Big(1 + \frac{\rho h_2}{I_{0,1} + I_{0,2} + \frac{\sigma^2}{P_0}}\Big). \tag{8.7}$$

In the above equations, $I_{0,1} = \sum_{j\in\Phi_1/UE_1} g_{1,j} R_{1,j}^{-\alpha} P_{1,j}^u$ and $I_{0,2} = \sum_{j\in\Phi_2/UE_2} g_{2,j} R_{2,j}^{-\alpha} P_{2,j}^u$ are accumulated inter-cell interference from Φ_1/UE_1 and Φ_2/UE_2 respectively. $g_{1,j}$, $R_{1,j}$, $g_{2,j}$ and $R_{2,j}$ are the corresponding Rayleigh fading gain and interfering distance. $P_{1,j}^u = r_{1,j}^{\alpha}$ and $P_{2,j}^u = \rho * r_{2,j}^{\alpha}$ represent the respective UE transmit powers in Φ_1/UE_1 and Φ_2/UE_2 divided by P_0. $r_{1,j}$ and $r_{2,j}$ are the corresponding transmit distances. Notice that $P_{2,j}^u$ has a back-off step ρ. σ^2 denotes noise power which is constant and additive. $\frac{\sigma^2}{P_0}$ is the inverse of uplink arrived signal-to-noise ratio (SNR). The key notations used in this paper are listed in Table 8.1

8.2 Downlink NOMA system analysis

The performance of downlink NOMA system is analyzed in terms of outage probability and average achievable rate. The study on NOMA with the random pairing scheme is presented at first, then followed by the study on NOMA with the selective paring scheme.

8.2.1 Downlink NOMA with random pairing

The outage probability and average achievable rate for a downlink NOMA system with random pairing are analyzed in this subsection. To facilitate the derivation, the cumulative distribution function (CDF) of the normalized channel gain for a randomly selected UE is

Table 8.1: List of Key Notations

$\Phi_b(\Phi_u)$	PPP constituted by BSs (UEs)
$\lambda_b(\lambda_u)$	Density of BSs (UEs)
Φ_i/UE_i	PPP constituted by UE_is in other cells
λ_i	Density of UE_is in each cell
T_i	Selecting threshold for UE_i
P_b	Transmit power of BS on a sub-band
ϵ	Downlink NOMA power control parameter
P_i^d	Downlink NOMA transmit power allocated to UE_i
h_i	Rayleigh fading gain between BS_0 and UE_i
r_i	Distance between BS_0 and UE_i
α	Path-loss exponent
c_i	Normalized channel gain
I_i	Cumulative inter-cell interference received at UE_i
β	Fraction of remaining NOMA interference
P_i^u	Transmit power of UE_1
P_0	Target received power at BS
ρ	Back-off step for P_2^u
$I_{0,i}$	Cumulative inter-cell interference from Φ_i
σ^2	Noise power

first presented.

CDF of normalized channel gain for a randomly selected UE

The normalized channel gain of a randomly selected UE is $c = \frac{hr^{-\alpha}}{I}$. The CDF of c is given in Chapter 6 as

$$F_c(C) = 1 - \frac{1}{1 + (CP_b)^{\frac{2}{\alpha}} \int_{(CP_b)^{-\frac{2}{\alpha}}}^{\infty} \frac{1}{1+u^{\frac{\alpha}{2}}} du}. \tag{8.8}$$

For a special case with $\alpha = 4$, (8.8) can be further simplified to

$$F_c(C) \overset{\alpha=4}{=} 1 - \frac{1}{1 + \sqrt{CP_b}(\frac{\pi}{2} - \arctan(\frac{1}{\sqrt{CP_b}}))}. \tag{8.9}$$

Outage performance of NOMA with random pairing

In this subsection, the outage probabilities of UE_1 and UE_2 are derived as well as the overall outage probability in a 2-UE downlink NOMA case. The analysis extends the

previous work in Chapter 6 with the following major improvements. First, the imperfect SIC is considered in the analytical while in Chapter 6 a perfect SIC is assumed. Second, in this chapter, the performance of each UE is evaluated in terms of outage probability while in Chapter 6 the distribution of the post-process signal-to-interference ratio (SIR) is studied. Also, the overall NOMA system performance is provided, which is not considered in Chapter 6.

Two UEs are randomly selected among all UEs associated with the typical BS and are marked as UE_a and UE_b. The normalized channel gains of UE_a and UE_b are denoted as c_a and c_b. Rank the channel gains and let $UE_1 = \{UE_i | UE_i \in \{UE_a, UE_b\}, c_i = \max(c_a, c_b)\}$ and $UE_2 = \{UE_i | UE_i \in \{UE_a, UE_b\}, c_i = \min(c_a, c_b)\}$. Let $z = \max(x, y)$ and $w = \min(x, y)$. The CDF of z and w can be expressed as $F_z(z) = F_{xy}(z, z)$ and $F_w(w) = F_x(w) + F_y(w) - F_{xy}(w, w)$ [67]. Thus CDFs of c_1 and c_2 can be derived in the following.

$$\begin{aligned} F_{c_1}(C) &= F_{c_a c_b}(C, C) \\ &= F_c(C)^2, \end{aligned} \tag{8.10}$$

$$\begin{aligned} F_{c_2}(C) &= F_{c_a}(C) + F_{c_b}(C) - F_{c_a c_b}(C, C) \\ &= 2F_c(C) - F_c(C)^2, \end{aligned} \tag{8.11}$$

as $\{c_a, c_b\}$ are i.i.d. and $F_c(C)$ is given in (8.8).

The outage probability is defined as the probability that τ_i^k, $k \in \{d, u\}$, fails to meet the defined quality of service (QoS) requirement, which is defined as the target data rate $\bar{\tau}_i$ in this chapter. The outage probability for UE_1 and UE_2 are derived respectively at first, and then the outage probability for the overall system is provided.

For UE_1, the rate for UE_1 to decode UE_2's message $\tau_{1\to 2}^d$ must be greater than the QoS requirement of UE_2 $\bar{\tau}_2$ so that it is able to remove UE_2's signal from interference. Thus

the outage probability of UE_1 can be evaluated as follows:

$$\begin{aligned} p_1^d(\bar{\tau_1}, \bar{\tau_2}) &= 1 - \mathbb{P}[\tau_1^d > \bar{\tau_1}, \tau_{1\to 2}^d > \bar{\tau_2}] \\ &= 1 - \mathbb{P}[\frac{c_1 P_1^d}{\beta c_1 P_2^d + 1} > \gamma_1, \frac{c_1 P_2^d}{c_1 P_1^d + 1} > \gamma_2] \\ &= 1 - \mathbb{P}[c_1(P_1^d - \gamma_1 \beta P_2^d) > \gamma_1, c_1(P_2^d - \gamma_2 P_1^d) > \gamma_2] \\ &= \begin{cases} 1, & \text{if } \gamma_1 \geq \frac{P_1^d}{\beta P_2^d} \text{ or } \gamma_2 \geq \frac{P_2^d}{P_1^d}; \\ F_{c_1}\big(\max(\theta_1, \theta_2)\big), & \text{otherwise.} \end{cases} \end{aligned} \tag{8.12}$$

$\gamma_1 = 2^{\bar{\tau_1}} - 1$, $\gamma_2 = 2^{\bar{\tau_2}} - 1$, $\theta_1 = \frac{\gamma_1}{P_1^d - \gamma_1 \beta P_2^d}$, and $\theta_2 = \frac{\gamma_2}{P_2^d - \gamma_2 P_1^d}$ are used to simplify the expression. $F_{c_1}(C)$ is given in (8.10). The outage probability of UE_2 is given as

$$\begin{aligned} p_2^d(\bar{\tau_2}) &= 1 - \mathbb{P}[\tau_2^d > \bar{\tau_2}] \\ &= 1 - \mathbb{P}\Big[\frac{c_2 P_2^d}{c_2 P_1^d + 1} > \gamma_2\Big] \\ &= 1 - \mathbb{P}[c_c(P_2^d - \gamma_2 P_1^d) > \gamma_2] \\ &= \begin{cases} 1, & \text{if } \gamma_2 \geq \frac{P_2^d}{P_1^d}; \\ F_{c_2}(\theta_2), & \text{otherwise.} \end{cases} \end{aligned} \tag{8.13}$$

In addition to the individual UE outage probability, the overall outage probability of NOMA UEs is given as

$$\begin{aligned} & p_{total}^d(\bar{\tau_1}, \bar{\tau_2}) \\ &= \begin{cases} 1, & \text{if } \gamma_1 \geq \frac{P_1^d}{\beta P_2^d} \text{ or } \gamma_2 \geq \frac{P_2^d}{P_1^d}; \\ F_{c_2}(\theta_2), & \text{if } \gamma_1 < \frac{P_1^d}{\beta P_2^d},\ \gamma_2 < \frac{P_2^d}{P_1^d},\ \theta_2 > \theta_1; \\ F_c(\theta_1)^2 + 2F_c(\theta_2) - 2F_c(\theta_1)F_c(\theta_2), & \text{otherwise.} \end{cases} \end{aligned} \tag{8.14}$$

The detailed derivation of (8.14) is provided in Appendix 8.A. By comparing (8.12) and (8.13) one can observe that $p_2^d(\bar{\tau_2})$ is only affected by $\bar{\tau_2}$. However, $p_1^d(\bar{\tau_1}, \bar{\tau_2})$ is affected by both $\bar{\tau_1}$ and $\bar{\tau_2}$. This is due to the fact that UE_1 needs to decode x_2 at first in order to

decode its own message x_1. Therefore, failing to decode x_2 also causes outage at UE_1. Also one can see that the outage probability always equals 1 if $\bar{\tau_1}$ or $\bar{\tau_2}$ is not set appropriately. After selecting reasonable values for $\bar{\tau_1}$ and $\bar{\tau_2}$, $p_1^d(\bar{\tau_1}, \bar{\tau_2})$ is only determined by either $\bar{\tau_1}$ or $\bar{\tau_2}$, whereas $p_{total}^d(\bar{\tau_1}, \bar{\tau_2})$ is affected by both $\bar{\tau_1}$ and $\bar{\tau_2}$ simultaneously as shown in (8.14).

Average Achievable Rate of NOMA with Random Pairing

It is assumed that each UE can reach Shannon bound for their instantaneous SIR. Notice that $\tau_{1\to 2}^d > \tau_2^d$ is always true as $c_1 > c_2$. Therefore, the average achievable rate of UE_1 can be given as

$$\begin{aligned}\tau_{1,avg}^d &= \mathbb{E}[\log_2(1 + \frac{h_1 r_1^{-\alpha} P_1^d}{I_1 + \beta h_1 r_1^{-\alpha} P_2^d})] \\ &= \mathbb{E}[\log_2(1 + (\beta P_2^d + P_1^d)c_1)] - \mathbb{E}[\log_2(1 + \beta P_2^d c_1)]. \end{aligned} \tag{8.15}$$

The first expectation in (8.15) can be computed as

$$\begin{aligned}&\mathbb{E}[\log_2(1 + (\beta P_2^d + P_1^d)c_1)] \\ &\overset{(a)}{=} \int_{t>0} \mathbb{P}[\log_2(1 + (\beta P_2^d + P_1^d)c_1) > t]dt \\ &= \int_{t>0} (1 - F_{c_1}(\frac{2^t - 1}{\beta P_2^d + P_1^d}))dt, \end{aligned} \tag{8.16}$$

where (a) is met as $\mathbb{E}[X] = \int_{t>0} \mathbb{P}(X > t)dt$ for a positive random variable X. By setting $P_1^d = 0$ in (8.16), the second expectation in (8.15) can be acquired. Then the complete result of $\tau_{1,avg}^d$ is

$$\tau_{1,avg}^d = \int_{t>0} F_{c_1}(\frac{2^t - 1}{\beta P_2^d}) - F_{c_1}(\frac{2^t - 1}{\beta P_2^d + P_1^d})dt. \tag{8.17}$$

By following the same way given above, the average achievable rate of UE_2 is

$$\begin{aligned}\tau_{2,avg}^{d} &= \mathbb{E}[\log_2(1+\frac{h_2 r_2^{-\alpha} P_2^d}{I_2 + h_2 r_2^{-\alpha} P_1^d})] \\ &= \mathbb{E}[\log_2(1+(P_1^d+P_2^d)c_2)] - \mathbb{E}[\log_2(1+P_1^d c_2)] \\ &= \int_{t>0} F_{c_2}(\frac{2^t-1}{P_1^d}) - F_{c_2}(\frac{2^t-1}{P_2^d+P_1^d})dt. \end{aligned} \tag{8.18}$$

The framework developed here can also be applied to more general order based pairing schemes [79]. For instance, the performance of pairing UE_v and UE_w that are selected from M UEs, $1 \leq v \leq w \leq M$, can be derived by following the same approach.

8.2.2 Downlink NOMA with Selective Pairing

The previous analysis is based on random pairing for the two UEs in a NOMA group. The results in [79] show that the performance gain of NOMA can be further enlarged by selecting NOMA UEs deliberately. In this subsection, the analytical results when using selective pairing scheme is provided. Instead of selecting UEs based on the order of their channel gain like what is applied in [79], selective pairing scheme selects UEs based on the actual channel gain values. More specifically, UE whose normalized channel gain is above a pre-determined threshold T_1 can be selected as $UE_{1,s}$ and UE whose normalized channel gain is below another threshold T_2 ($T_2 \leq T_1$), is selected as $UE_{2,s}$.

Outage Probability with Selective Pairing

Denoted by $c_{1,s}$ the normalized channel gain of $UE_{1,s}$, the CDF of $c_{1,s}$ is calculated as

$$\begin{aligned} F_{c_{1,s}}(C) &= \mathbb{P}[c_{1,s} < C] = \mathbb{P}[c < C | c > T_1] \\ &\overset{(a)}{=} \begin{cases} 0, & \text{if } C < T_1; \\ \frac{\mathbb{P}[c<C, c>T_1]}{\mathbb{P}[c>T_1]}, & \text{otherwise.} \end{cases} \\ &= \begin{cases} 0, & \text{if } C < T_1; \\ \frac{F_c(C)-F_c(T_1)}{1-F_c(T_1)}, & \text{otherwise.} \end{cases} \end{aligned} \tag{8.19}$$

In (a) Bayes' rule is applied. Similarly, the CDF of $UE_{2,s}$'s normalized channel gain is calculated as

$$\begin{aligned} F_{c_{2,s}}(C) &= \mathbb{P}[c_{2,s} < C] = \mathbb{P}[c < C | c < T_2] \\ &= \begin{cases} 1, & \text{if } C > T_2; \\ \frac{\mathbb{P}[c<C]}{\mathbb{P}[c<T_2]}, & \text{otherwise.} \end{cases} \\ &= \begin{cases} 1, & \text{if } C > T_2; \\ \frac{F_c(C)}{F_c(T_2)}, & \text{otherwise.} \end{cases} \end{aligned} \tag{8.20}$$

By substituting $F_{c_1}(C)$ in (8.12) with $F_{c_{1,s}}(C)$ and substituting $F_{c_2}(C)$ in (8.13) by $F_{c_{2,s}}(C)$, the outage probabilities of $UE_{1,s}$ and $UE_{2,s}$ respectively become

$$\begin{aligned} p^d_{1,s}(\bar{\tau_1}, \bar{\tau_2}) &= 1 - \mathbb{P}[\tau_{1,s} > \bar{\tau_1}, \tau_{1,s\to 2} > \bar{\tau_2}] \\ &= 1 - \mathbb{P}[\frac{c_{1,s}P_1^d}{\beta c_{1,s}P_2^d + 1} > \gamma_1, \frac{c_{1,s}P_2^d}{c_{1,s}P_1^d + 1} > \gamma_2] \\ &= \begin{cases} 1, & \text{if } \gamma_1 \geq \frac{P_1^d}{\beta P_2^d} \text{ or } \gamma_2 \geq \frac{P_2^d}{P_1^d}; \\ F_{c_{1,s}}\Big(\max(\theta_1, \theta_2)\Big), & \text{otherwise.} \end{cases} \\ &= \begin{cases} 1, & \text{if } \gamma_1 \geq \frac{P_1^d}{\beta P_2^d} \text{ or } \gamma_2 \geq \frac{P_2^d}{P_1^d}; \\ 0, & \text{if } \gamma_1 < \frac{P_1^d}{\beta P_2^d} \text{ and } \gamma_2 < \frac{P_2^d}{P_1^d} \text{ and } \max(\theta_1, \theta_2) < T_1; \\ \frac{F_c(\max(\theta_1,\theta_2)) - F_c(T_1)}{1 - F_c(T_1)}, & \text{otherwise.} \end{cases} \end{aligned} \tag{8.21}$$

$$\begin{aligned} p^d_{2,s}(\bar{\tau_2}) &= 1 - \mathbb{P}[\tau_{2,s} > \bar{\tau_2}] \\ &= \begin{cases} 1, & \text{if } \gamma_2 \geq \frac{P_2^d}{P_1^d}; \\ F_{c_{2,s}}(\theta_2), & \text{otherwise.} \end{cases} \\ &= \begin{cases} 1, & \text{if } \gamma_2 \geq \frac{P_2^d}{P_1^d} \text{ or } \theta_2 > T_2; \\ \frac{F_c(\theta_2)}{F_c(T_2)}, & \text{otherwise.} \end{cases} \end{aligned} \tag{8.22}$$

The definitions of $\tau_{1,s}$, $\tau_{1,s\to 2}$, and $\tau_{2,s}$ are the same as defined earlier on. As $p^d_{1,s}(\bar{\tau_1}, \bar{\tau_2})$ and $p^d_{2,s}(\bar{\tau_2})$ are independent, the total system outage probability with selective pairing is

$$\begin{aligned} p^d_{total,s}(\bar{\tau_1}, \bar{\tau_2}) &= 1 - \mathbb{P}[\tau_{1,s} > \bar{\tau_1}, \tau_{2,s} > \bar{\tau_2}] \\ &= 1 - \mathbb{P}[\tau_{1,s} > \bar{\tau_1}]\mathbb{P}[\tau_{2,s} > \bar{\tau_2}] \\ &= 1 - (1 - p^d_{2,s}(\bar{\tau_2}))\mathbb{P}[\tau_{1,s} > \bar{\tau_1}], \end{aligned} \tag{8.23}$$

where

$$\begin{aligned} \mathbb{P}[\tau_{1,s} > \bar{\tau_1}] &= \mathbb{P}\Big[\frac{c_{1,s}P_1^d}{\beta c_{1,s}P_2^d + 1} > \gamma_1\Big] \\ &= \begin{cases} 0, & \text{if } \gamma_1 \geq \frac{P_1^d}{\beta P_2^d}; \\ 1 - F_{c_{1,s}}(\theta_1), & \text{otherwise.} \end{cases} \end{aligned} \tag{8.24}$$

By summarizing the equations above, one can get the complete result of $p^d_{total,s}(\bar{\tau_1}, \bar{\tau_2})$ as

$$\begin{aligned} &p^d_{total,s}(\bar{\tau_1}, \bar{\tau_2}) = \\ &\begin{cases} 1, & \text{if } \gamma_1 \geq \frac{P_1^d}{\beta P_2^d} \text{ or } \gamma_2 \geq \frac{P_2^d}{P_1^d}; \\ F_{c_{1,s}}(\theta_1) + F_{c_{2,s}}(\theta_2) - F_{c_{1,s}}(\theta_1)F_{c_{2,s}}(\theta_2), & \text{otherwise.} \end{cases} \end{aligned} \tag{8.25}$$

By observing (8.21) and (8.22), one can see that $p^d_{1,s}(\bar{\tau_1}, \bar{\tau_2})$ and $p^d_{2,s}(\bar{\tau_2})$ are bounded by not only $\bar{\tau_i}$, but also T_i due to the reason that the normalized channel gain of UEs using selective pairing is bounded. Later numerical results will show that selective pairing in this way can be leveraged to determine the value of P_1^d and P_2^d so that the performance of all UEs is guaranteed to be better than that in OMA.

Average Achievable Rate With Selective Pairing

Substituting $F_{c_1}(C)$ in (8.17) with $F_{c_{1,s}}(C)$, the average achievable rate of $UE_{1,s}$ with selective pairing is

$$\begin{aligned}\tau^d_{1,s,avg} &= \int_{t>0} F_{c_{1,s}}(\frac{2^t-1}{\beta P_2^d}) - F_{c_{1,s}}(\frac{2^t-1}{\beta P_2^d + P_1^d})dt \\ &= \int_{\log_2(\beta P_2^d T_1+1)}^{\log_2((\beta P_2^d+P_1^d)T_1+1)} \frac{F_c(\frac{2^t-1}{\beta P_2^d}) - F_c(T_1)}{1-F_c(T_1)}dt \\ &+ \int_{\log_2((\beta P_2^d+P_1^d)T_1+1)}^{\infty} \frac{F_c(\frac{2^t-1}{\beta P_2^d}) - F_c(\frac{2^t-1}{\beta P_2^d+P_1^d})}{1-F_c(T_1)}dt. \end{aligned} \tag{8.26}$$

Similarly, substituting $F_{c_1}(C)$ in (8.18) with $F_{c_{1,s}}(C)$, the average achievable rate of $UE_{2,s}$ with selective pairing is

$$\begin{aligned}\tau^d_{2,s,avg} &= \int_{t>0} F_{c_{2,s}}(\frac{2^t-1}{P_1^d}) - F_{c_{2,s}}(\frac{2^t-1}{P_2^d + P_1^d})dt \\ &= \int_{0}^{\log_2(P_1^d T_2+1)} \frac{F_c(\frac{2^t-1}{P_1^d}) - F_c(\frac{2^t-1}{P_2^d+P_1^d})}{F_c(T_2)}dt \\ &+ \int_{\log_2(P_1^d T_2+1)}^{\log_2((P_1^d+P_2^d)T_2+1)} 1 - \frac{F_c(\frac{2^t-1}{P_2^d+P_1^d})}{F_c(T_2)}dt. \end{aligned} \tag{8.27}$$

8.2.3 NOMA Power Control with Selective Pairing

In [73] authors point out that a fixed power allocation based NOMA can not strictly meet the predefined QoS. For example, in a fixed power allocation based NOMA, the rate of a poor channel UE can be lower than that in OMA. However, selective pairing NOMA has the freedom to set the values of P_1^d and P_2^d so that the performance of all UEs can be better than that in OMA. Assuming a perfect SIC, the rate of $UE_{1,s}$ is $\tau_{1,s} = \log_2(1+c_{1,s}P_1^d)$ when using NOMA. $\tau^o_{1,s} = \frac{1}{2}\log_2(1+c_{1,s}P_b)$ is the rate when using OMA assuming the transmit power and resource are equally allocated to two UEs. In order to guarantee $\tau_{1,s} \geq \tau^o_{p,1}$, the following constraint needs to be met.

$$\log_2(1+c_{1,s}P_1^d) \geq \frac{1}{2}\log_2(1+c_{1,s}P_b),$$

which is equivalent to

$$P_1^d \geq \frac{\sqrt{1+c_{1,s}P_b}-1}{c_{1,s}}. \tag{8.28}$$

Since $c_{1,s} > T_1$, (8.28) is always true when $P_1^d > \frac{\sqrt{1+P_bT_1}-1}{T_1}$.

For $UE_{2,s}$, $\tau_{2,s} = \log_2(1+\frac{c_{2,s}P_2^d}{c_{2,s}P_1^d+1})$ and $\tau_{2,s}^o = \frac{1}{2}\log_2(1+c_{2,s}P_b)$. To make sure $\tau_{2,s} \geq \tau_{2,s}^o$, the following constraint needs to be met.

$$\log_2(1+\frac{c_{2,s}P_2^d}{c_{2,s}P_1^d+1}) \geq \frac{1}{2}\log_2(1+c_{2,s}P_b),$$

which is equivalent to

$$P_1^d \leq \frac{\sqrt{1+c_{2,s}P_b}-1}{c_{2,s}}. \tag{8.29}$$

Since $c_{2,s} < T_2$, (8.29) is always true when $P_1^d < \frac{\sqrt{1+P_bT_2}-1}{T_2}$. Recall that $T_1 \geq T_2$, both (8.28) and (8.29) can be satisfied simultaneously when setting $\frac{\sqrt{1+P_bT_1}-1}{T_1} < P_1^d < \frac{\sqrt{1+P_bT_2}-1}{T_2}$, i.e.,

$$\frac{\sqrt{1+P_bT_1}-1}{P_bT_1} < \epsilon < \frac{\sqrt{1+P_bT_2}-1}{P_bT_2}. \tag{8.30}$$

Once T_1 and T_2 are defined, the above constraint can give a pseudo-static value of ϵ, which does not need to be updated dynamically based on channel conditions, hence does not cause extra signaling overhead for NOMA downlink power allocation.

8.3 Uplink NOMA system analysis

8.3.1 Outage Probability for Uplink NOMA

To facilitate the derivation, in the following the Laplace transform of two interference terms $I_{0,1}$ and $I_{0,2}$ are provided at first, shown in equations (8.31) and (8.32).

$$\mathcal{L}_{I_{0,1}}(s) = \exp\Big(-\pi\lambda_1 s^{\frac{2}{\alpha}}\mathbb{E}[(P_1^u)^{\frac{2}{\alpha}}]\int_{s^{-\frac{2}{\alpha}}}^{\infty}\frac{1}{1+y^{\frac{\alpha}{2}}}dy\Big), \tag{8.31}$$

$$\mathcal{L}_{I_{0,2}}(s) = \exp\Big(-\pi\lambda_2 s^{\frac{2}{\alpha}}\mathbb{E}[(P_2^u)^{\frac{2}{\alpha}}]\int_{(\rho s)^{-\frac{2}{\alpha}}}^{\infty}\frac{1}{1+y^{\frac{\alpha}{2}}}dy\Big), \tag{8.32}$$

where $\mathbb{E}[(P_1^u)^{\frac{2}{\alpha}}] = \frac{1}{\pi\lambda_b}$ and $\mathbb{E}[(P_2^u)^{\frac{2}{\alpha}}] = \frac{1}{\pi\lambda_b}\rho^{\frac{2}{\alpha}}$. The detailed derivation is provided in Appendix 8.B. For a special case $\alpha = 4$, $I_{0,1}(s)$ and $I_{0,2}(s)$ can be further simplified to

$$\mathcal{L}_{I_{0,1}}(s) \overset{\alpha=4}{=} \exp\Big(-2\sqrt{s}\cdot arctan(\sqrt{s})\Big), \tag{8.33}$$

$$\mathcal{L}_{I_{0,2}}(s) \overset{\alpha=4}{=} \exp\Big(-2\sqrt{\rho s}\cdot arctan(\sqrt{\rho s})\Big). \tag{8.34}$$

After acquiring $\mathcal{L}_{I_{0,1}}(s)$ and $\mathcal{L}_{I_{0,2}}(s)$, one can compute the outage probability. Recall that $h_1 > h_2$, the complementary of the outage probability of UE_1 is given by

$$\begin{aligned}\bar{p}_1^u(\gamma_1) &= \mathbb{P}\Big[\log_2\Big(1+\frac{h_1}{\rho h_2 + I_{0,1} + I_{0,2} + \frac{\sigma^2}{P_0}}\Big) > \bar{\tau}_1\Big] \\ &= \mathbb{P}[h_1 > \max(h_2, \gamma_1(\rho h_2 + I_{0,1} + I_{0,2} + \frac{\sigma^2}{P_0}))].\end{aligned} \tag{8.35}$$

When $\gamma_1\rho \geq 1$, $\bar{p}_1^u(\bar{\tau}_1)$ becomes

$$\begin{aligned}\bar{p}_1^u(\gamma_1) &\overset{\gamma_1\rho>1}{=} \mathbb{P}[h_1 > \gamma_1(\rho h_2 + I_{0,1} + I_{0,2} + \frac{\sigma^2}{P_0})] \\ &= \mathbb{E}[\int_{h_2=0}^{\infty}\int_{h_1=\gamma_1(\rho h_2+I_{0,1}+I_{0,2}+\frac{\sigma^2}{P_0})}^{\infty} f_{h_1h_2}(h_1,h_2)dh_1dh_2] \\ &= \frac{2}{1+\gamma_1\rho}e^{-\frac{\gamma_1\sigma^2}{P_0}}\mathcal{L}_{I_{0,1}}(\gamma_1)\mathcal{L}_{I_{0,2}}(\gamma_1).\end{aligned} \tag{8.36}$$

In last step $f_{h_1h_2}(h_1,h_2) = 2e^{-h_1-h_2}$ is used, based on order statistics [68]. $\mathcal{L}_{I_{0,1}}(s)$ and $\mathcal{L}_{I_{0,2}}(s)$ are given in (8.31) and (8.32) respectively.

When $\gamma_1\rho < 1$,

$$\begin{aligned}
\bar{p}_1^u(\gamma_1) &\overset{\gamma_1\rho<1}{=} \mathbb{P}\Big[h_1 > h_2, h_2 > \frac{\gamma_1(I_{0,1}+I_{0,2}+\frac{\sigma^2}{P_0})}{1-\gamma_1\rho}\Big] \\
&+ \mathbb{P}\Big[h_1 > \gamma_1(\rho h_2 + I_{0,1} + I_{0,2} + \frac{\sigma^2}{P_0}), h_2 < \frac{\gamma_1(I_{0,1}+I_{0,2}+\frac{\sigma^2}{P_0})}{1-\gamma_1\rho}\Big] \\
&= \mathbb{E}\Big[\int_{h_2=\frac{\gamma_1(I_{0,1}+I_{0,2}+\frac{\sigma^2}{P_0})}{1-\gamma_1\rho}}^{\infty} \int_{h_1>h_2} f_{h_1h_2}(h_1,h_2)dh_1dh_2 \\
&+ \int_{h_2=0}^{\frac{\gamma_1(I_{0,1}+I_{0,2}+\frac{\sigma^2}{P_0})}{1-\gamma_1\rho}} \int_{h_1>\gamma_1(\rho h_2+I_{0,1}+I_{0,2}+\frac{\sigma^2}{P_0})} f_{h_1h_2}(h_1,h_2)dh_1dh_2\Big] \\
&= \frac{\gamma_1\rho-1}{1+\gamma_1\rho}\mathcal{L}_{I_{0,1}}(\frac{2\gamma_1}{1-\gamma_1\rho})\mathcal{L}_{I_{0,2}}(\frac{2\gamma_1}{1-\gamma_1\rho})e^{-\frac{2\gamma_1\sigma^2}{(1-\gamma_1\rho)P_0}} \\
&+ \frac{2}{1+\gamma_1\rho}\mathcal{L}_{I_{0,1}}(\gamma_1)\mathcal{L}_{I_{0,2}}(\gamma_1)e^{-\frac{\gamma_1\sigma^2}{P_0}}.
\end{aligned} \tag{8.37}$$

By summarizing (8.36) (8.37) and using $p_1^u(\gamma_1) = 1 - \bar{p}_1^u(\gamma_1)$, one can get the outage probability of UE_1 as

$$p_1^u(\gamma_1) = \begin{cases} 1 - \frac{2}{1+\gamma_1\rho}e^{-\frac{\gamma_1\sigma^2}{P_0}}\mathcal{L}_{I_{0,1}}(\gamma_1)\mathcal{L}_{I_{0,2}}(\gamma_1), & \text{if } \gamma_1\rho \geq 1; \\ 1 - \frac{\gamma_1\rho-1}{1+\gamma_1\rho}\mathcal{L}_{I_{0,1}}(\frac{2\gamma_1}{1-\gamma_1\rho})\mathcal{L}_{I_{0,2}}(\frac{2\gamma_1}{1-\gamma_1\rho})e^{-\frac{2\gamma_1\sigma^2}{(1-\gamma_1\rho)P_0}} \\ \quad -\frac{2}{1+\gamma_1\rho}\mathcal{L}_{I_{0,1}}(\gamma_1)\mathcal{L}_{I_{0,2}}(\gamma_1)e^{-\frac{\gamma_1\sigma^2}{P_0}}, & \text{if } \gamma_1\rho < 1. \end{cases} \tag{8.38}$$

To decode UE_2's message, UE_1's message must be decoded successfully first. After UE_1's message is removed from the composed signal, UE_2's message can be decoded.

Therefore, the complementary of the outage probability of UE_2 can be expressed as

$$\begin{aligned}\bar{p}_2^u(\gamma_1,\gamma_2) &= \mathbb{P}\Big[\log_2(1+\frac{h_1}{\rho h_2+I_{0,1}+I_{0,2}+\frac{\sigma^2}{P_0}})>\bar{\tau_1},\\ &\qquad \log_2(1+\frac{\rho h_2}{I_{0,1}+I_{0,2}+\frac{\sigma^2}{P_0}})>\bar{\tau_2}\Big]\\ &= \mathbb{P}[h_1>\max(h_2,\gamma_1(\rho h_2+I_{0,1}+I_{0,2}+\frac{\sigma^2}{P_0})),\\ &\qquad h_2>\frac{\gamma_2}{\rho}(I_{0,1}+I_{0,2}+\frac{\sigma^2}{P_0})]. \end{aligned} \tag{8.39}$$

When $\gamma_1\rho\geq 1$, $\bar{p}_2^u(\gamma_1,\gamma_2)$ is

$$\begin{aligned}\bar{p}_2^u(\gamma_1,\gamma_2) &= \mathbb{P}[h_1>\gamma_1(\rho h_2+I_{0,1}+I_{0,2}+\frac{\sigma^2}{P_0}),\\ &\qquad h_2>\frac{\gamma_2}{\rho}(I_{0,1}+I_{0,2}+\frac{\sigma^2}{P_0})]\\ &= \mathbb{E}\Big[\int_{h_2=\frac{\gamma_2}{\rho}(I_{0,1}+I_{0,2}+\frac{\sigma^2}{P_0})}\int_{h_1=\gamma_1(\rho h_2+I_{0,1}+I_{0,2}+\frac{\sigma^2}{P_0})}\\ &\qquad f_{h_1h_2}(h_1,h_2)dh_1dh_2\Big]\\ &= \frac{2}{1+\gamma_1\rho}\mathcal{L}_{I_{0,1}}(A)\mathcal{L}_{I_{0,2}}(A)e^{-\frac{A\sigma^2}{P_0}}. \end{aligned} \tag{8.40}$$

$A=\gamma_1+\frac{\gamma_2}{\rho}+\gamma_1\gamma_2$. When $\gamma_1\rho<1$ and $\frac{\gamma_1}{1-\gamma_1\rho}>\frac{\gamma_2}{\rho}$,

$$\begin{aligned}\bar{p}_2^u(\gamma_1,\gamma_2) &= \mathbb{P}[h_2>\frac{\gamma_1}{1-\gamma_1\rho},h_1>h_2]\\ &\quad+\mathbb{P}[\frac{\gamma_2}{\rho}(I_{0,1}+I_{0,2}+\frac{\sigma^2}{P_0})<h_2<\frac{\gamma_1}{1-\gamma_1\rho}(I_{0,1}+I_{0,2}+\frac{\sigma^2}{P_0}),\\ &\qquad h_1>\gamma_1(\rho h_2+I_{0,1}+I_{0,2}+\frac{\sigma^2}{P_0})]\\ &= \frac{\gamma_1\rho-1}{\gamma_1\rho+1}\mathcal{L}_{I_{0,1}}(\frac{2\gamma_1}{1-\gamma_1\rho})\mathcal{L}_{I_{0,2}}(\frac{2\gamma_1}{1-\gamma_1\rho})e^{-\frac{2\gamma_1\sigma^2}{(1-\gamma_1\rho)P_0}}\\ &\quad+\frac{2}{1+\gamma_1\rho}\mathcal{L}_{I_{0,1}}(A)\mathcal{L}_{I_{0,2}}(A)e^{-\frac{A\sigma^2}{P_0}} \end{aligned} \tag{8.41}$$

Finally, when $\gamma_1\rho < 1$ and $\frac{\gamma_1}{1-\gamma_1\rho} < \frac{\gamma_2}{\rho}$,

$$\begin{aligned}\bar{p}_2^u(\gamma_1,\gamma_2) &= \mathbb{P}[h_2 > \frac{\gamma_2}{\rho}(I_{0,1}+I_{0,2}+\frac{\sigma^2}{P_0}), h_1 > h_2] \\ &= \mathcal{L}_{I_{0,1}}(\frac{2\gamma_2}{\rho})\mathcal{L}_{I_{0,2}}(\frac{2\gamma_2}{\rho})e^{-\frac{2\gamma_2\sigma^2}{\rho P_0}}. \end{aligned} \tag{8.42}$$

Summarizing (8.40) (8.41) (8.42) and using $p_2^u(\gamma_1,\gamma_2) = 1 - \bar{p}_2^u(\gamma_1,\gamma_2)$, one can obtain the outage probability of UE_2 as

$$p_2^u(\gamma_1,\gamma_2) = \begin{cases} 1 - \frac{2}{1+\gamma_1\rho}\mathcal{L}_{I_{0,1}}(A)\mathcal{L}_{I_{0,2}}(A)e^{-\frac{A\sigma^2}{P_0}}, & \text{if } \gamma_1\rho \geq 1; \\ 1 - \frac{\gamma_1\rho-1}{\gamma_1\rho+1}\mathcal{L}_{I_{0,1}}(\frac{2\gamma_1}{1-\gamma_1\rho})\mathcal{L}_{I_{0,2}}(\frac{2\gamma_1}{1-\gamma_1\rho})e^{-\frac{2\gamma_1\sigma^2}{(1-\gamma_1\rho)P_0}} \\ \quad -\frac{2}{1+\gamma_1\rho}\mathcal{L}_{I_{0,1}}(A)\mathcal{L}_{I_{0,2}}(A)e^{-\frac{A\sigma^2}{P_0}}, \text{if } \gamma_1\rho < 1, \frac{\gamma_1}{1-\gamma_1\rho} \geq \frac{\gamma_2}{\rho}; \\ 1 - \mathcal{L}_{I_{0,1}}(\frac{2\gamma_2}{\rho})\mathcal{L}_{I_{0,2}}(\frac{2\gamma_2}{\rho})e^{-\frac{2\gamma_2\sigma^2}{\rho P_0}}, \text{if } \gamma_1\rho < 1, \frac{\gamma_1}{1-\gamma_1\rho} < \frac{\gamma_2}{\rho}. \end{cases} \tag{8.43}$$

When $\alpha = 4$, both $p_1^u(\gamma_1)$ and $p_2^u(\gamma_1,\gamma_2)$ can be expressed in closed forms. Unlike downlink NOMA system, in uplink NOMA system the outage probability of UE_1 (good channel UE) is only affected by its own target rate $\bar{\tau}_1$. Whereas the outage probability of UE_2 (poor channel UE) is affected by both $\bar{\tau}_1$ and $\bar{\tau}_2$ due to the fact that a BS needs to decode the message from UE_1 at first. More details about the relationship between outage probability and target rate are discussed in numerical results section.

8.3.2 Average Achievable Rate for Uplink NOMA

The average achievable rate $\tau^u_{1,avg}$ for uplink NOMA UE_1 can be expressed in form of outage probability as given below.

$$\begin{aligned}\tau^u_{1,avg} &= \mathbb{E}\Big[\log_2\big(1+\frac{h_1}{h_2\rho+I_{0,1}+I_{0,2}+\frac{\sigma^2}{P_0}}\big)\Big]\\ &\overset{(a)}{=} \int_{t>0}\mathbb{P}\Big[\frac{h_1}{h_2\rho+I_{0,1}+I_{0,2}+\frac{\sigma^2}{P_0}}>2^t-1\Big]dt\\ &= \int_{t>0}\bar{p}^u_1(2^t-1)dt,\end{aligned} \tag{8.44}$$

where in (a) $\mathbb{E}[X]=\int_{t>0}\mathbb{P}(X>t)dt$ is used. Similarly the average achievable rate $\tau^u_{2,avg}$ for uplink NOMA UE_2 is derived as

$$\begin{aligned}\tau^u_{2,avg} &= \mathbb{E}\Big[\log_2\big(1+\frac{h_2\rho}{I_{0,1}+I_{0,2}+\frac{\sigma^2}{P_0}}\big)\Big]\\ &= \int_{t>0}\mathbb{P}\Big[\frac{h_2\rho}{I_{0,1}+I_{0,2}+\frac{\sigma^2}{P_0}}>2^t-1\Big]dt\\ &= \int_{t>0}\bar{p}^u_2(0,2^t-1)dt.\end{aligned} \tag{8.45}$$

8.4 Numerical Evaluation

In this section, system performance is numerically evaluated based on both analytical models and simulations. For all the results, the density of BS is set as $\lambda_b = 10^{-3}/m^2$ (corresponding to a hexagon grid with a radius 6.2 m) and path-loss exponent $\alpha = 4$. The bandwidth of one sub-band is normalized to 1. As a comparison to NOMA, OMA results from simulations are also presented. For a fair comparison to NOMA, OMA gives each of the two UEs in the NOMA group half unit of the resource. For the downlink OMA, BS transmits with half of its full power to each UE on its dedicated resource. For the uplink OMA, each UE transmits on its dedicated resource subject to the uplink proportional power control.

8.4.1 Downlink NOMA Performance Results

BS power P_b is also normalized to 1 and the power control parameter ϵ for downlink NOMA is set to 0.2 unless otherwise mentioned.

Figure 8.3 shows UE_1 outage probability $p_1^d(\bar{\tau_1}, \bar{\tau_2})$, UE_2 outage probability $p_2^d(\bar{\tau_2})$, and overall system outage probability $p_{total}^d(\bar{\tau_1}, \bar{\tau_2})$ vs. different target rates $\bar{\tau_1}$ and $\bar{\tau_2}$. Figure 8.3(a) presents the impact of $\bar{\tau_1}$ on the outage probability when $\bar{\tau_2}$ is fixed at 0.2 bits/s/sub-band. Figure 8.3(b) fixes $\bar{\tau_1}$ at 0.1 bits/s/sub-band to demonstrate the impact of $\bar{\tau_2}$. β is set to 0, i.e., perfect SIC, in both cases. From the figure one can see the analytical results match the simulation results very well, which validates the accuracy of the analysis.

In Figure 8.3(a), $p_1^d(\bar{\tau_1}, \bar{\tau_2})$ remains constant when $\bar{\tau_1}$ is below 0.06, due to the fact that UE_1 needs to decode the signal intended to UE_2 first before it can decode the signal for itself. When $\bar{\tau_1}$ is below 0.06, the outage is always caused by failing to decode x_2. This outcome can also be explained by looking into the definition of $p_1^d(\bar{\tau_1}, \bar{\tau_2})$. Recall that in (8.12) $p_1^d(\bar{\tau_1}, \bar{\tau_2}) = 1 - \mathbb{P}[\tau_1^d > \bar{\tau_1}, \tau_{1\to 2}^d > \bar{\tau_2}]$, which is a function of both $\bar{\tau_1}$ and $\bar{\tau_2}$. Given a fixed $\bar{\tau_2}$, $\tau_{1\to 2}^d > \bar{\tau_2}$ can guarantee $\tau_1^d > \bar{\tau_1}$ when $\bar{\tau_1}$ is small and $p_1^d(\bar{\tau_1}, \bar{\tau_2})$ can be rewritten to $p_1^d(\bar{\tau_1}, \bar{\tau_2}) = 1 - \mathbb{P}[\tau_{1\to 2}^d > \bar{\tau_2}]$, which is not a function of $\bar{\tau_1}$ anymore and thus keeps a constant when $\bar{\tau_1}$ is small. The curve of $p_{total}^d(\bar{\tau_1}, \bar{\tau_2})$ overlaps with $p_2^d(\bar{\tau_2})$ when $\bar{\tau_1}$ is small due to a similar reason declared above. Recall that in (8.47) $p_{total}^d(\bar{\tau_1}, \bar{\tau_2}) = 1 - \mathbb{P}[\tau_1^d > \bar{\tau_1}, \tau_2^d > \bar{\tau_2}]$, which can be rewritten to $p_{total}^d(\bar{\tau_1}, \bar{\tau_2}) = 1 - \mathbb{P}[\tau_2^d > \bar{\tau_2}]$ when $\bar{\tau_1}$ is small. Therefore, $p_{total}^d(\bar{\tau_1}, \bar{\tau_2}) = p_2^d(\bar{\tau_2})$ and thus their curves completely overlap with each other when $\bar{\tau_1}$ is small. $p_2^d(\bar{\tau_2})$ is a flat line in Figure 8.3(a) as $\bar{\tau_2}$ is fixed and it is not influenced by $\bar{\tau_1}$.

Figure 8.3(b) in turn fixes $\bar{\tau_1}$ at 0.1 bits/s/sub-band to investigate the impact of $\bar{\tau_2}$. One can observe that $p_1^d(\bar{\tau_1}, \bar{\tau_2})$ remains constant at first and then increases in the same way as in Figure 8.3(a), due to a similar reason that makes $p_1^d(\bar{\tau_1}, \bar{\tau_2})$ constant in Figure 8.3(a). When $\bar{\tau_2}$ is small, $p_1^d(\bar{\tau_1}, \bar{\tau_2})$ can be rewritten as $1 - \mathbb{P}[\tau_1^d > \bar{\tau_1}]$, which is not affected by $\bar{\tau_2}$. As $\bar{\tau_2}$ goes up, both $\bar{\tau_1}$ and $\bar{\tau_2}$ will impact $p_1^d(\bar{\tau_1}, \bar{\tau_2})$ and $p_1^d(\bar{\tau_1}, \bar{\tau_2})$ starts to increase along with $\bar{\tau_2}$. $p_2^d(\bar{\tau_2})$ completely overlaps with $p_{total}^d(\bar{\tau_1}, \bar{\tau_2})$ after $\bar{\tau_2}$ exceeds a certain value, which is consistent with the result in (8.14). When $\bar{\tau_2}$ satisfies $\gamma_2 < \frac{P_2^d}{P_1^d}$ and $\theta_2 > \theta_1$ (both

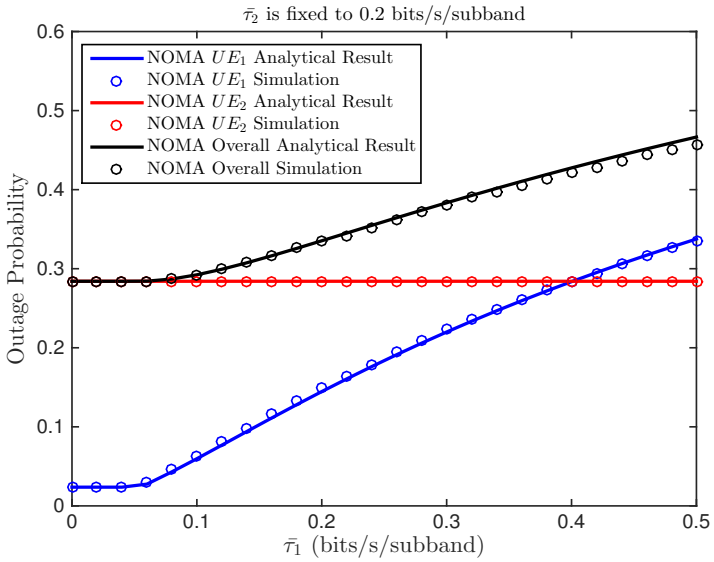

(a) Outage probability for random pairing NOMA when $\bar{\tau}_2$ is fixed to 0.2 bits/s/sub-band.

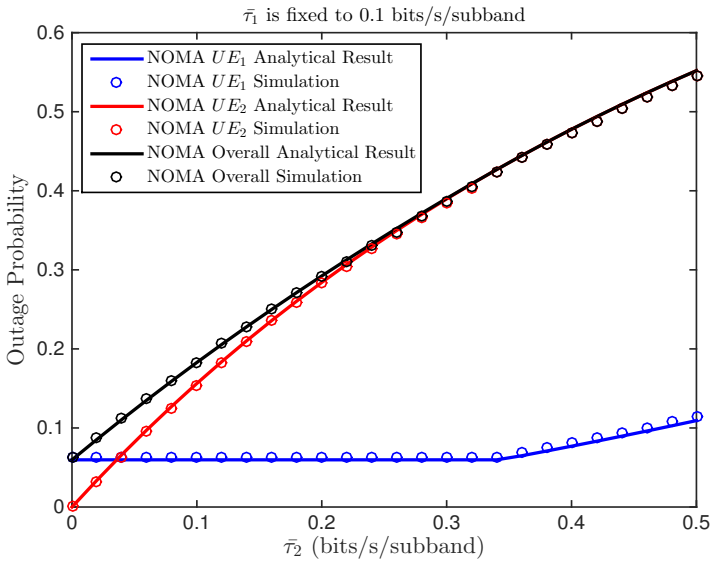

(b) Outage probability for random pairing NOMA when $\bar{\tau}_1$ is fixed to 0.1 bits/s/sub-band.

Fig. 8.3: Downlink outage probability for random pairing NOMA.

γ_2 and θ_2 are functions of $\bar{\tau_2}$), $p^d_{total}(\bar{\tau_1}, \bar{\tau_2})$ becomes a function of $\bar{\tau_2}$. By comparing Figure 8.3(a) and Figure 8.3(b), one can discover that for a given $\bar{\tau_2}$, $\bar{\tau_1}$ does not affect $p^d_1(\bar{\tau_1}, \bar{\tau_2})$ or $p^d_{total}(\bar{\tau_1}, \bar{\tau_2})$ within a certain range of $\bar{\tau_1}$. However, $\bar{\tau_2}$ always affects the outage probability regardless of the value of $\bar{\tau_1}$.

Figure 8.4 compares the outage performance between random pairing NOMA and OMA. Only analytical numerical results are presented as simulation results always match the analytical results very well on the downlink.

In Figure 8.4(a) one can observe that with a smaller value of ϵ, which means a smaller transmit power is allocated to UE_1, $p^d_1(\bar{\tau_1}, \bar{\tau_2})$ is always higher than the OMA outage probability. Even with $\epsilon = 0.5$, $p^d_1(\bar{\tau_1}, \bar{\tau_2})$ is still higher than the OMA outage probability when $\bar{\tau_1}$ is relatively small. This is due to the fact that UE_1 needs to decode x_2 at first and outage occurs regardless of the $\bar{\tau_1}$ value if x_2 fails to be decoded. Also one can observe that the lower bound of $p^d_1(\bar{\tau_1}, \bar{\tau_2})$, which is determined by successfully decoding x_2, goes up along with ϵ. This is because more transmit power allocated to UE_1 also means less power allocated to UE_2 and thus it is more difficult for UE_1 to decode x_2. Therefore, increasing ϵ does not necessarily help improve $p^d_1(\bar{\tau_1}, \bar{\tau_2})$.

In Figure 8.4(b), one can observe that $p^d_2(\bar{\tau_2})$ decreases with a smaller ϵ, i.e., more transmit power is allocated to UE_2. From Figure 8.4, one can conclude that $p^d_2(\bar{\tau_2})$ is always improved when more power is allocated to UE_2. However, for UE_1, $p^d_1(\bar{\tau_1}, \bar{\tau_2})$ is affected by both $\bar{\tau_1}$ and $\bar{\tau_2}$. More allocated power to UE_1 can result in an even worse outage probability for UE_1.

In Figure 8.5 the impact of imperfect SIC on NOMA is investigated. The impact of imperfect SIC is crucial on the average achievable rate of NOMA. When $\beta = 0.06$, i.e., 6% inter-user NOMA interference fails to be eliminated, the gain of NOMA completely vanishes in the presented cases. One can observe that with a greater ϵ, which indicates more power is allocated to UE_1, the gain of NOMA over OMA is higher. So a greater ϵ makes it more resistant to the impact of imperfect SIC. However, when $\epsilon < 0.1$, even with a perfect SIC, NOMA does not show any gain over OMA.

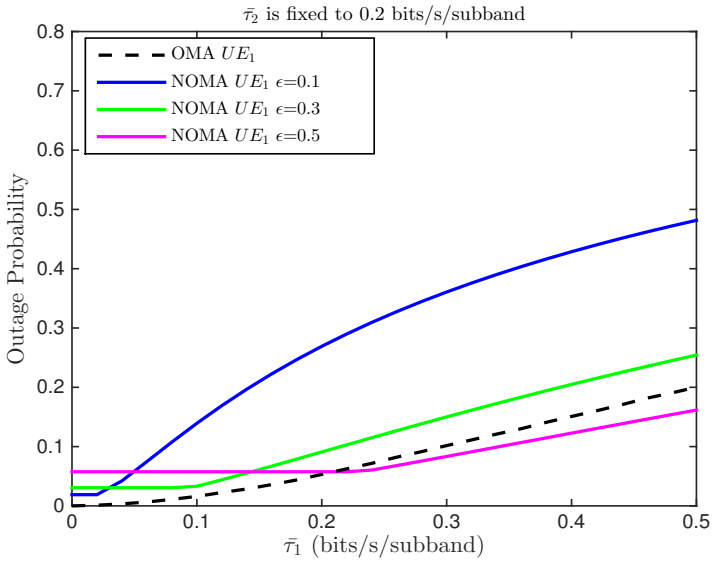

(a) Outage probability of UE_1. $\bar{\tau}_2$ is fixed to 0.2 bits/s/sub-band.

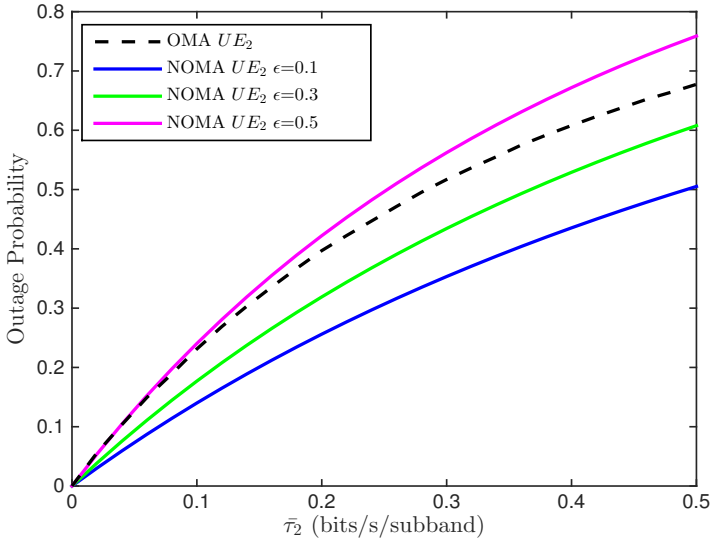

(b) Outage probability of UE_2.

Fig. 8.4: Downlink outage probability comparison between random pairing NOMA and OMA.

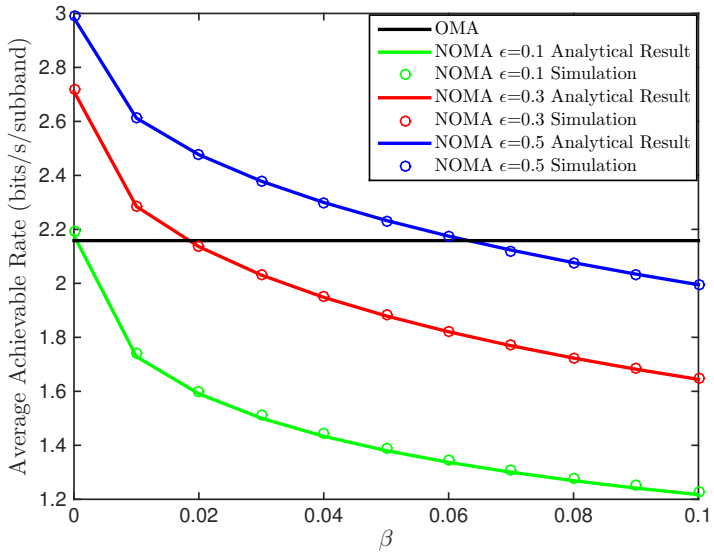

Fig. 8.5: Average achievable rate of downlink NOMA UEs (sum of $\tau^d_{1,avg}$ and $\tau^d_{2,avg}$) with imperfect SIC.

Figure 8.6 and Figure 8.7 present the performance of downlink NOMA with selective pairing. The thresholds are set as $T_1 = 3$ dB and $T_2 = 0$ dB respectively. Figure 8.6 shows how $\bar{\tau_1}$ and $\bar{\tau_2}$ impact the outage probability. In Figure 8.6(a), the outage probability of UE_1 can be as low as 0 and the overall outage probability is the same as $p^d_{2,s}(\bar{\tau_2})$ when $p^d_{1,s}(\bar{\tau_1}, \bar{\tau_2})$ is 0, since the channel gain of UE_1 in selective pairing has a lower bound $c_{1,s} > T_1$. By looking into (8.21), one can see that given a fixed $\bar{\tau_2}$ selective pairing can have zero outage for $\bar{\tau_1}$ that satisfies $\max(\theta_1, \theta_2) < T_1$. Similarly, in Fig. 8.6(b), $p^d_{1,s}(\bar{\tau_1}, \bar{\tau_2})$ also has zero outage when $\bar{\tau_2} < 1.1$ bits/s/sub-band for a fixed $\bar{\tau_1}$. $p^d_{2,s}(\bar{\tau_2})$ has an upper bound, which is due to the channel threshold $c_{2,s} < T_2$. By summarizing Figure 8.6(a) and Figure 8.6(b), one can conclude that zero outage is possible for selective pairing by choosing $\bar{\tau_1}$ and $\bar{\tau_1}$ deliberately while outage always has a non-zero probability for the random pairing case.

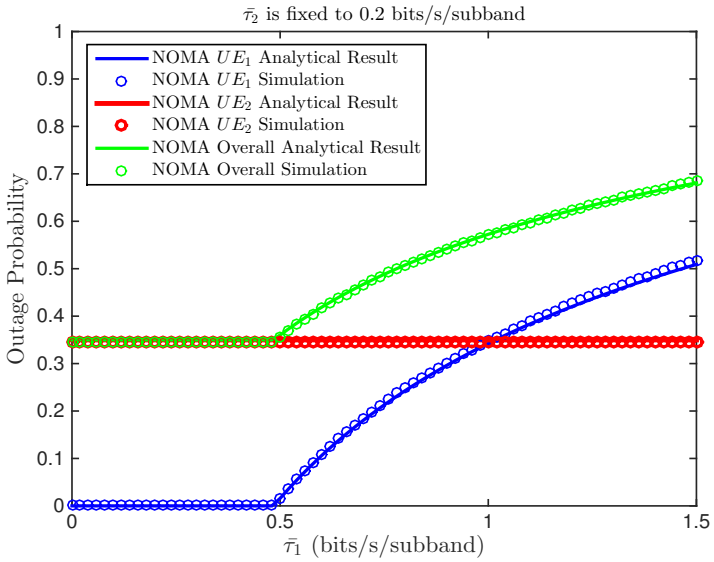

(a) Outage probability of UE_1. $\bar{\tau}_2$ is fixed to 0.2 bits/s/sub-band.

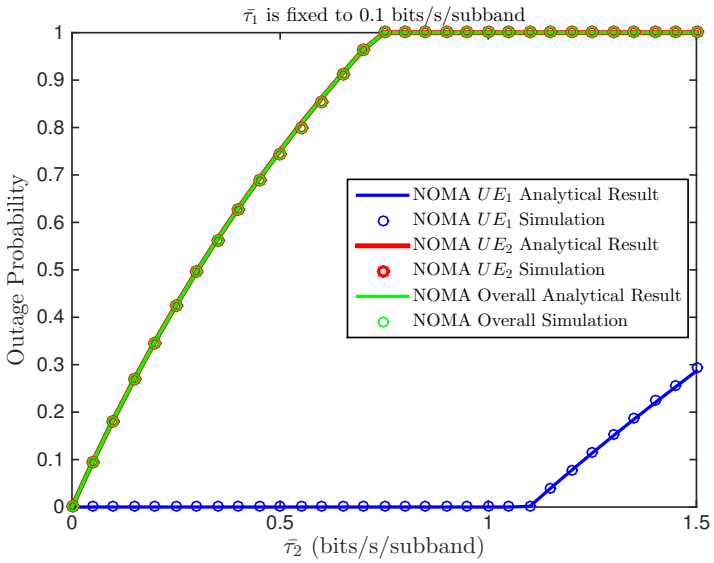

(b) Outage probability of UE_2. $\bar{\tau}_1$ is fixed to 0.1 bits/s/sub-band.

Fig. 8.6: Downlink outage probability for selective pairing NOMA.

Figure 8.7 compares the outage performance between selective pairing NOMA and OMA. In Figure 8.7(a), one can find that by setting ϵ properly, the outage probability of UE_1 in selective pairing NOMA can always be lower than that in OMA. However, such a value of ϵ does not exist for random pairing NOMA, as shown in Figure 8.4(a). By observing Figure 8.7(a) and Figure 8.7(b) together, one can find that when setting $\epsilon = 0.4$, which satisfies (8.30), both UE_1 and UE_2 can have better outage performance than using OMA. Therefore, for selective pairing NOMA, performance gain over OMA can be guaranteed with a simple fixed power allocation scheme, whereas dynamic power allocation is required to achieve such a performance gain in random pairing NOMA [73].

Figure 8.8 compares the performance of selective pairing NOMA and random pairing NOMA. It is not fair to compare them by the absolute achievable rate as they each select different UEs for NOMA, i.e., UEs in random pairing NOMA are selected randomly whereas UEs in selective pairing NOMA are selected based on thresholds. Therefore, the comparison between two NOMA pairing schemes is made on the gain of average achievable rate over OMA, i.e., the difference of achievable rate obtained by NOMA and OMA for the same group of UEs. T_2 is fixed at 0 dB and the impact of T_1 is of interest. By increasing T_1, the performance of selective pairing can be further improved. This outcome is consistent with the conclusion drawn in [79], which states that the performance gain of NOMA over OMA can be further enlarged by selecting UEs whose channel conditions are more distinctive. Although it improves the performance of selective pairing, increasing T_1 also makes it harder to find a qualified UE_1. In practice, there is a trade-off between the performance of a selected pair and the number of pairs that can be selected. Another observation one can obtain from Figure 8.8 is that allocating more transmit power to UE_1 can boost the total rate and selective pairing NOMA can benefit more from that than random pairing NOMA.

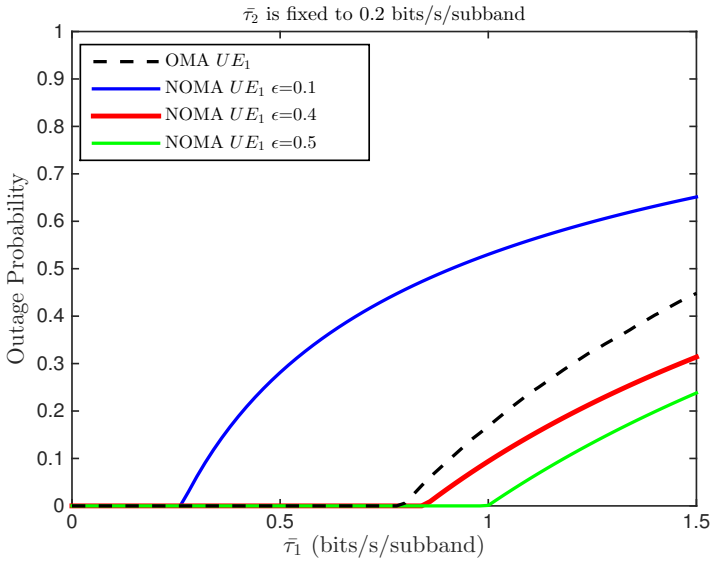

(a) Outage probability of UE_1. $\bar{\tau}_2$ is fixed to 0.2 bits/s/sub-band.

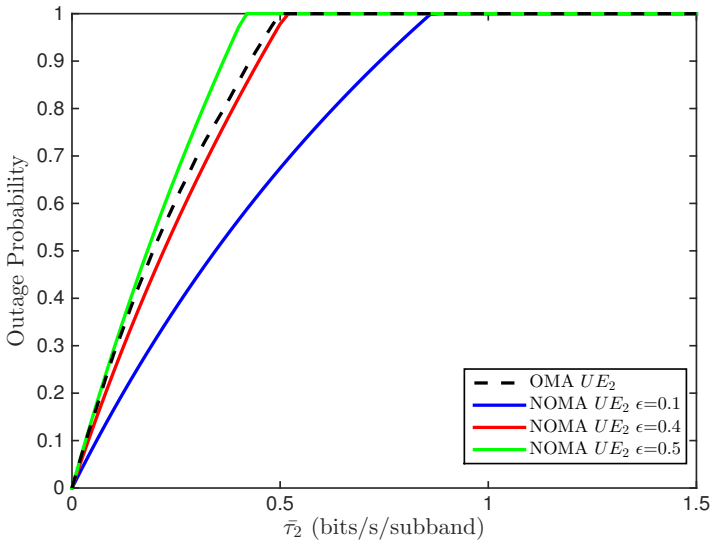

(b) Outage probability of UE_2.

Fig. 8.7: Downlink outage probability comparison between selective pairing NOMA and OMA.

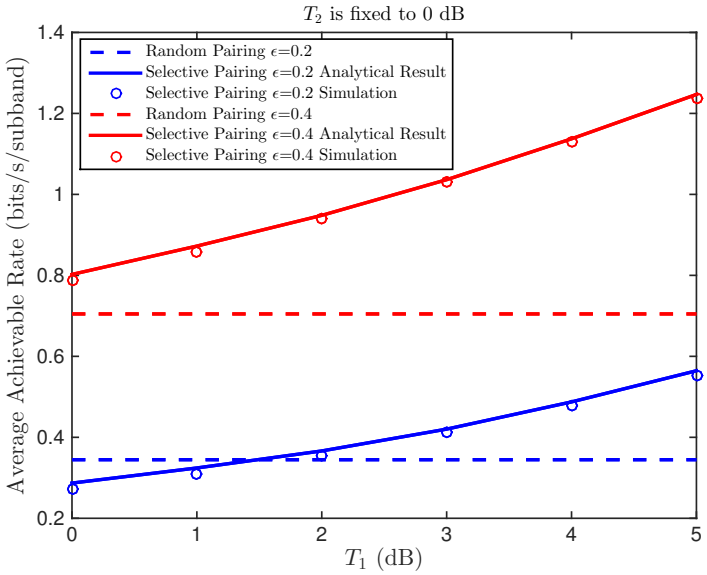

Fig. 8.8: Comparison of downlink average achievable rate gain over OMA between random pairing NOMA and selective paring NOMA.

8.4.2 Up NOMA Performance Results

Figure 8.9 compares the uplink outage probability between NOMA with different back-off steps ρ and OMA. The arrived SNR $\frac{P_0}{\sigma^2}$ is set to 30 dB. It is assumed that the OMA UE under comparison uses the same power as its NOMA counterpart. Each OMA UE is allocated half of the sub-band resource and its interference plus noise becomes $\frac{1}{2}(P_0 I_{0,1} + P_0 I_{0,2} + \sigma^2)$. The small gap between the simulation and the analytical results comes from the assumption that Φ_1 and Φ_2 are approximated to PPPs, which in reality are not. Figure 8.9(a) shows that for UE_1, the outage probability of NOMA outperforms OMA when ρ is small, as a smaller ρ results in less inter-user interference from UE_2 in the same cell and also less inter-cell interference from UE_2s in other cells ($I_{0,2}$). The outage probability of UE_2 is given in Figure 8.9(b). UE_2's outage performance degrades as ρ gets small. Although a smaller ρ decreases the inter-cell interference to UE_2, the loss due to a lower transmit power is more significant. Figure 8.9(b) also shows that increasing $\bar{\tau_1}$ can increase the outage probability of UE_2. In uplink NOMA, BS needs to decode the message intended to UE_1 first. Increasing $\bar{\tau_1}$ results in a higher outage for UE_1, which consequently impacts UE_2 signal decoding.

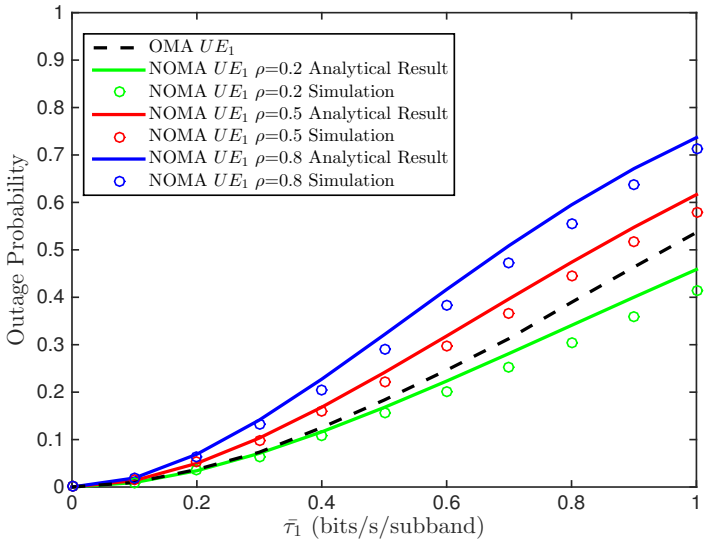

(a) Outage probability of UE_1.

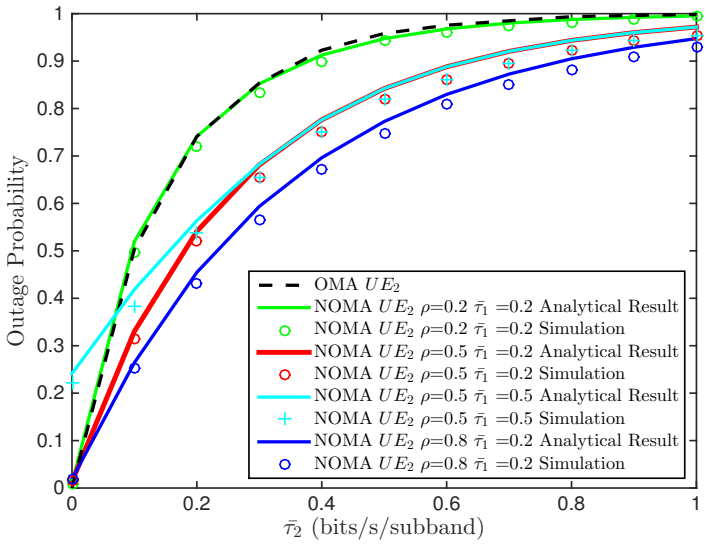

(b) Outage probability of UE_2.

Fig. 8.9: Uplink outage probability comparison between NOMA and OMA.

Figure 8.10 compares the average achievable rates of UE_1 and UE_2 with different ρ values. One can observe that the average achievable rate goes up along with the arrived SNR level. However, after the arrived SNR level reaches a certain value, this gain disappears due to the fact that the uplink system turns into interference limited. Again the slight gap between simulation and analytical results comes from approximating the UE distribution as a PPP.

Figure 8.11 presents the comparison between uplink NOMA and OMA on the average achievable rate. Clearly the sum rate of NOMA outperforms OMA for all SNR scenarios. And the gain of NOMA over OMA is more significant when the value of ρ is small, which means the gain of UE_1 is much more significant than the loss of UE_2. However, in Figure 8.10, it shows that the gap between the rates of UE_1 and UE_2 also goes up as the value of ρ gets small, leading to poorer fairness. Thus when selecting the value of ρ, both sum rate and fairness need to be evaluated.

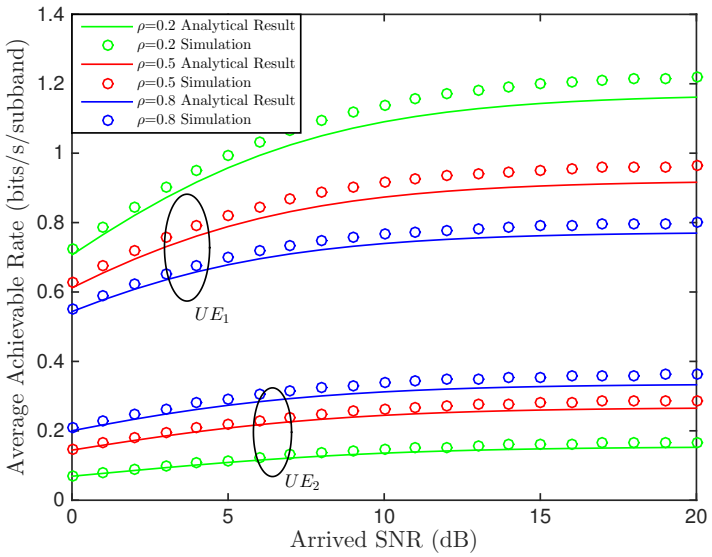

Fig. 8.10: Uplink average achievable rate of NOMA vs. different arrived SNR.

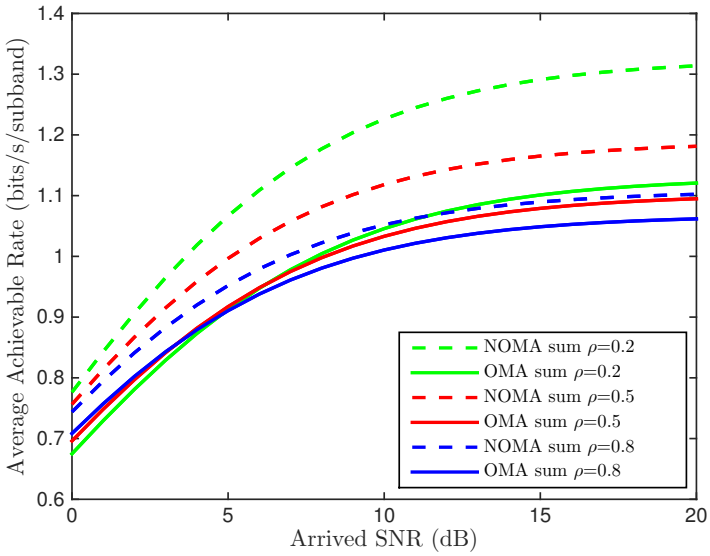

Fig. 8.11: Uplink average achievable rate comparison between NOMA and OMA.

8.5 Conclusion

In this chapter, an analytical framework is developed to analyze NOMA downlink and uplink system performance. Analytical results are derived by using stochastic geometry approach in a dense wireless network environment. For the downlink NOMA system, two different pairing schemes, namely random pairing and selective pairing, are investigated. The study shows that selective pairing can offer a better performance gain over OMA than the random pairing scheme. Moreover, selective pairing NOMA is able to use a fixed power allocation scheme to achieve the prominent performance gain, which can only be realized by a dynamic power allocation in order based NOMA scheme. Analytical results of uplink NOMA are derived with the same system model for the downlink scenario and a revised back-off uplink power control scheme is used. The study shows that increasing arrived SNR does not bring significant performance gain once the arrived SNR reaches a certain level. This chapter systematically investigates outage probability and achievable data rates for both uplink and downlink NOMA in a dense wireless network with various system settings.

Appendix

8.A

The overall outage probability of NOMA UEs is defined as

$$p^d_{total}(\bar{\tau_1}, \bar{\tau_2}) = 1 - \mathbb{P}[\tau^d_1 > \bar{\tau_1}, \tau^d_{1\to 2} > \bar{\tau_2}, \tau^d_2 > \bar{\tau_2}]. \tag{8.46}$$

Notice that $\tau^d_{1\to 2} > \bar{\tau_2}$ is always true when $\tau^d_2 > \bar{\tau_2}$ due to $c_1 > c_2$. Therefor (8.46) can be simplified to $p^d_{total}(\bar{\tau_1}, \bar{\tau_2}) = 1 - \mathbb{P}[\tau^d_1 > \bar{\tau_1}, \tau^d_2 > \bar{\tau_2}]$. The derivation proceeds as

$$\begin{aligned} p^d_{total}(\bar{\tau_1}, \bar{\tau_2}) &= 1 - \mathbb{P}[\tau^d_1 > \bar{\tau_1}, \tau^d_2 > \bar{\tau_2}] \\ &= 1 - \mathbb{P}\Big[\frac{c_1 P^d_1}{\beta c_1 P^d_2 + 1} > \gamma_1, \frac{c_2 P^d_2}{c_2 P^d_1 + 1} > \gamma_2\Big] \\ &= \begin{cases} 1, & \text{if } \gamma_1 \geq \frac{P^d_1}{\beta P^d_2} \text{ or } \gamma_2 \geq \frac{P^d_2}{P^d_1}; \\ 1 - \mathbb{P}[c_1 > \theta_1, c_2 > \theta_2], & \text{otherwise.} \end{cases} \end{aligned} \tag{8.47}$$

As $c_1 > c_2$, $\mathbb{P}[c_1 > \theta_1, c_2 > \theta_2]$ can be simplified to $\mathbb{P}[c_2 > \theta_2] = 1 - F_{c_2}(\theta_2)$ when $\theta_1 < \theta_2$. When $\theta_1 \geq \theta_2$, $\mathbb{P}[c_1 > \theta_1, c_2 > \theta_2]$ can be derived as

$$\begin{aligned} \mathbb{P}[c_1 > \theta_1, c_2 > \theta_2] &= \int_{c_1=\theta_1}^{\infty} \int_{c_2=\theta_2}^{c_1} f_{c_1 c_2}(c_1, c_2) dc_1 dc_2 \\ &= \int_{c_1=\theta_1}^{\infty} \int_{c_2=\theta_2}^{c_1} 2 f_c(c_1) f_c(c_2) dc_1 dc_2 \\ &= 1 - F_c(\theta_1)^2 - 2F_c(\theta_2) + 2F_c(\theta_1)F_c(\theta_2), \end{aligned} \tag{8.48}$$

where $f_{c_1 c_2}(c_1, c_2)$ is the joint probability density function (PDF) of c_1 and c_2, and it can be acquired by using the knowledge of order statistics as $f_{c_1 c_2}(c_1, c_2) = 2 f_c(c_1) f_c(c_2)$ [68]. By summarizing the results above, the complete expression of $p^d_{total}(\bar{\tau_1}, \bar{\tau_2})$ is acquired.

8.B

The Laplace transform of $I_{0,1}$, $\mathcal{L}_{I_{0,1}} = \mathbb{E}_{I_{0,1}}[e^{-sI_{0,1}}]$, is given as

$$\begin{aligned}
\mathcal{L}_{I_{0,1}}(s) &= \mathbb{E}\Big[\exp(-\mathbb{1}(P^u_{1,j}R^{-\alpha}_{1,j} < 1)\sum_{j\in\Phi_1/UE_1} sP^u_{1,j}g_{1,j}R^{-\alpha}_{1,j})\Big] \\
&= \mathbb{E}\Big[\prod_{j\in\Phi_1/UE_1} \exp\big(-\mathbb{1}(P^u_{1,j}R^{-\alpha}_{1,j} < 1)sP^u_{1,j}g_{1,j}R^{-\alpha}_{1,j}\big)\Big] \\
&\overset{(a)}{=} \exp\Big(-2\pi\lambda_1\mathbb{E}\big[\int_{(P^u_1)^{\frac{1}{\alpha}}}^{\infty}(1-e^{-sP^u_1 gx^{-\alpha}})xdx\big]\Big) \\
&\overset{(b)}{=} \exp\Big(-2\pi\lambda_1\mathbb{E}\big[\int_{(P^u_1)^{\frac{1}{\alpha}}}^{\infty}\frac{1}{1+\frac{x^\alpha}{sP^u_1}}xdx\big]\Big) \\
&\overset{(c)}{=} \exp\Big(-\pi\lambda_1\mathbb{E}\big[\int_{s^{-\frac{2}{\alpha}}}^{\infty}\frac{1}{1+y^{\frac{\alpha}{2}}}(sP^u_1)^{\frac{2}{\alpha}}dy\big]\Big) \\
&= \exp\Big(-\pi\lambda_1 s^{\frac{2}{\alpha}}\mathbb{E}[(P^u_1)^{\frac{2}{\alpha}}]\int_{s^{-\frac{2}{\alpha}}}^{\infty}\frac{1}{1+y^{\frac{\alpha}{2}}}dy\Big).
\end{aligned} \tag{8.49}$$

$\mathbb{1}(\cdot)$ is an indicator function that equals 1 when the condition in the parentheses is satisfied and equals 0 otherwise. The condition $P^u_{1,j}R^{-\alpha}_{1,j} < 1$ defined here reflects the fact that $P^u_{1,j} = r^\alpha_{1,j}$ and $r_{1,j} < R_{1,j}$ since all UEs are associated to the nearest BS. (a) follows from the probability generating functional (PGFL) of PPP [75], which states that $\mathbb{E}[\prod_{x\in\Phi} f(x)] = \exp(-\lambda\int_{\mathbb{R}^2}(1-f(x))dx)$. (b) follows from $g \sim \exp(1)$ and (c) is acquired by using $y = \frac{x^2}{(sP^u_1)^{\frac{2}{\alpha}}}$. By using the PDF of the distance between a UE and its associated BS given ealier, $\mathbb{E}[(P^u_1)^{\frac{2}{\alpha}}]$ can be computed as

$$\begin{aligned}
\mathbb{E}[(P^u_1)^{\frac{2}{\alpha}}] &= \int_0^\infty (r^\alpha)^{\frac{2}{\alpha}} f_r(r)dr \\
&= \int_0^\infty r^2 \cdot 2\pi\lambda_b r e^{-\pi\lambda_b r^2}dr = \frac{1}{\pi\lambda_b}.
\end{aligned} \tag{8.50}$$

Notice that the value of $\mathbb{E}[(P_1^u)^{\frac{2}{\alpha}}]$ is not affected by α. $\mathcal{L}_{I_{0,2}}(s)$ can be derived in a similar way.

$$\begin{aligned}\mathcal{L}_{I_{0,2}}(s) &= \mathbb{E}\Big[\exp(-\mathbb{1}(P_{2,j}^u R_{2,j}^{-\alpha} < \rho) \sum_{j\in\Phi_2/UE_2} sP_{2,j}^u g_{2,j} R_{2,j}^{-\alpha})\Big] \\ &= \exp\Big(-\pi\lambda_2 s^{\frac{2}{\alpha}}\mathbb{E}[(P_2^u)^{\frac{2}{\alpha}}]\int_{(\rho s)^{-\frac{2}{\alpha}}}^{\infty}\frac{1}{1+y^{\frac{\alpha}{2}}}dy\Big), \end{aligned} \tag{8.51}$$

where $\mathbb{E}[(P_2^u)^{\frac{2}{\alpha}}] = \frac{1}{\pi\lambda_b}\rho^{\frac{2}{\alpha}}$.

CHAPTER 9

Dynamic Power Splitting Between Information and Power Transfer in Non-orthogonal Multiple Access

This chapter proposes a dynamic power splitting scheme in a non-orthogonal multiple access (NOMA) based 5G system with simultaneous wireless information and power transfer (SWIPT). With the proposed scheme UEs can harvest the maximum amount of energy while still achieve the same data rate as that achieved in the traditional orthogonal multiple access (OMA) schemes. Theoretical analysis is conducted on the stochastic characteristics of power splitting scheme in NOMA and the optimal energy harvesting policy under the constraint of user data rates is provided. The average amount of harvested energy is derived. All the analytical results are presented in succinct closed forms or pseudo-closed forms and validated by simulations. Numerical results demonstrate that with the proposed scheme users with good channels can benefit from SWIPT on both energy harvesting and data rate satisfaction while users with poor channels can benefit on data rate satisfaction.

9.1 Introduction

Recently simultaneous wireless information and power transfer (SWIPT) [80] technology, which can extend the lifetime of batteries of devices by harvesting energy from radio frequency (RF) signals, is considered a promising technology for 5G communications to support power limited Internet of Things (IoT) type devices. Two practical energy harvesting mechanisms for SWIPT are introduced in the seminal work [80], namely time switching (TS) scheme and power splitting (PS) scheme. This chapter focuses on the PS scheme. Particularly, it is assumed that all user equipments (UEs) are equipped with co-located energy harvesting and information decoding processing units. By using the PS scheme, a received signal is split into two separate signal streams. One stream is sent to the energy harvesting unit and the other one is sent to the information decoding unit.

NOMA with SWIPT has attracted extensive research attention lately. In [81] authors proposed a cooperative downlink NOMA system and the relay power is harvested by using SWIPT. Authors in [82] studied an uplink NOMA system, where the user transmit power is harvested exclusively from downlink base station (BS) RF transmissions. In [50], authors investigated the application of SWIPT in a novel cooperative NOMA system, in which good channel NOMA users act as energy harvesting relays to help poor channel NOMA users.

The focus of this chapter is to analyze the maximum amount of energy that can be harvested in a NOMA system under the constraint that the user quality of service (QoS) is satisfied. More specifically, the gain of NOMA with SWIPT over OMA is investigated in terms of harvested energy given that both NOMA and OMA achieve the same user data rates. Towards that end, this chapter proposes a dynamic power splitting scheme for a downlink NOMA system in which NOMA UEs harvest energy from the received RF signals by using a PS scheme. With the proposed scheme UEs can harvest the maximum amount of energy while still achieve the same data rates as what can be achieved in the traditional OMA schemes. Due to the dynamic and opportunistic characteristic of wireless channels and UE locations, the ratio of the received power that can be used for UE energy harvesting is a random variable, which can be analyzed through its cumulative distribution function (CDF). Thus the closed form expression of the CDF of power splitting coefficient is derived, which reflects the percentage of the received power that can be harvested. The power splitting coefficient is dynamically tuned to achieve the maximum harvested energy given that the data rate constraints are met. All the analytical results are validated by simulations. Numerical results demonstrate that with the proposed scheme UEs with good channels can benefit from SWIPT on both energy harvesting and data rate satisfaction while users with poor channels can benefit on data rate satisfaction, all compared with the results from traditional OMA schemes.

9.2 System Model

This chapter considers downlink NOMA transmission in a single cell scenario. BS is located at the center of a disk with a radius R and all UEs are uniformly distributed within

the disc. It is assumed that both BS and UEs are equipped with a single antenna. NOMA study in this chapter assumes the size of the NOMA group is two, as initially specified in 3GPP LTE Advanced. Selective user pairing scheme proposed in Chapter 8 is applied in this work. More specifically, two UEs within a NOMA group are selected among all UEs based on their instantaneous channel gains. Denoting the good channel UE and poor channel UE as UE_1 and UE_2 respectively, a UE can be selected as UE_1 if its channel gain is above threshold T_1 and can be selected as UE_2 if its channel gain is below threshold T_2. $T_1 \geq T_2$ ensures that the channel gain of UE_1 is always greater than UE_2 so that SIC at the receiving side can achieve a good performance. A fixed power allocation strategy is used as it can avoid an excessive signaling overhead required by dynamic power allocation strategies but still achieves a suboptimal performance [76, 77]. P_0 denotes the total transmit power allocated to a NOMA group. ϵP_0 denotes the power allocated to UE_1 and $(1-\epsilon)P_0$ is the power allocated to UE_2, where $\epsilon \in (0, 0.5)$ is a NOMA power control parameter.

9.2.1 Channel Model

The channel model used in this chapter consists of large scale path-loss and Rayleigh fading. The channel gain between BS and a randomly chosen UE can be expressed as $C = \frac{h}{1+r^\alpha}$, where h denotes the Rayleigh fading gain and follows an exponential distribution with mean 1, r denotes the transmission distance, and α is the path-loss exponent. A bounded path-loss model is applied here to ensure that the path loss is always larger than one for any transmission distance [83]. As UEs are uniformly distributed in the coverage of the BS, the probability density function (PDF) of r is $f_r(x) = \frac{2x}{R^2}$, $x \in [0, R]$. By leveraging the PDFs of both h and r, the CDF of channel gain C is given in [83] as

$$F_C(x) = \frac{2}{R^2} \int_0^R (1 - e^{-(1+y^\alpha)x}) y dy. \tag{9.1}$$

The closed form expression of (9.1) for a general α is difficult to acquire. For the special case $\alpha = 2$, the closed form of (9.1) can be found as

$$F_C(x) \overset{\alpha=2}{=} 1 - \frac{e^{-x}}{R^2 x} + \frac{e^{-(1+R^2)x}}{R^2 x}. \tag{9.2}$$

A tight approximation of (9.1) for a general value of α is derived in [15] by applying Gaussian-Chebyshev quadrature. In this chapter $\alpha = 2$ is assumed to facilitate the mathematical analysis and closed form derivation.

9.2.2 Downlink NOMA System

According to the principle of PD-NOMA [56], the transmitted NOMA signal at BS is expressed as

$$x = \sqrt{\epsilon P_0} x_1 + \sqrt{(1-\epsilon) P_0} x_2, \tag{9.3}$$

where x_i is the message intended to UE_i with $\mathbb{E}[|x_i|^2] = 1$, $i \in \{1, 2\}$. It is assumed that all UEs are equipped with rechargeable functionality so that they can harvest energy from the surrounding electromagnetic waves. Power splitting is applied between wireless information transmission and power transfer so that both information transmission and energy harvesting can be fulfilled from a received RF signal [80]. More specifically, a received signal at each UE is divided into two separate signal streams, one is used for energy harvesting and the other one is used for information decoding. Thus the received signal at UE_i for the information decoding is

$$y_i = \sqrt{(1-\beta_i) c_i} x + n, \tag{9.4}$$

where n denotes the additive white Gaussian noise (AWGN) at UE_i with a variance σ^2 (assuming all UEs experience the same noise power). $\beta_i \in [0, 1)$ is the power splitting coefficient which is used to determine the ratio of received power used for energy harvesting. c_i is the channel gain of UE_i. As the channel gain of UE_1 (UE_2) is above (below) threshold

T_1 (T_2), the CDF of c_i can be expressed in terms of $F_C(x)$ as

$$\begin{aligned} F_{c_1}(x) &= \mathbb{P}[c_1 < x] = \mathbb{P}[C < x | C \geq T_1] \\ &= \begin{cases} 0, & \text{if } x < T_1; \\ \frac{F_C(x) - F_C(T_1)}{1 - F_C(T_1)}, & \text{otherwise.} \end{cases} \end{aligned} \tag{9.5}$$

$$\begin{aligned} F_{c_2}(x) &= \mathbb{P}[c_2 < x] = \mathbb{P}[C < x | C \leq T_2] \\ &= \begin{cases} 0, & \text{if } x < 0; \\ 1, & \text{if } x \geq T_2; \\ \frac{F_C(x)}{F_C(T_2)}, & \text{otherwise.} \end{cases} \end{aligned} \tag{9.6}$$

Successive interference cancellation (SIC) [52] is utilized at UE_1 to extract intended message. Since UE_1 denotes the good channel UE within a NOMA group, UE_1 decodes x_2 first and removes the decoded message from the composite received signal y_1, based on which UE_1 can further decode its own message x_1. Therefore, the rates of UE_1 from decoding x_2 and x_1 are respectively given by

$$\tau_{1 \to 2} = \log_2 \Big(1 + \frac{(1 - \beta_1)(1 - \epsilon) c_1}{(1 - \beta_1) \epsilon c_1 + \frac{1}{\rho}} \Big), \tag{9.7}$$

and

$$\tau_1 = \log_2 \Big(1 + (1 - \beta_1) \epsilon c_1 \rho \Big), \tag{9.8}$$

where $\rho = \frac{P_0}{\sigma^2}$ is the transmitting signal-to-noise ratio (SNR) at the BS. Different with UE_1, UE_2 directly decodes x_2 by treating x_1 as interference. Thus the rate of UE_2 to decode x_2 is

$$\tau_2 = \log_2 \Big(1 + \frac{(1 - \beta_2)(1 - \epsilon) c_2}{(1 - \beta_2) \epsilon c_2 + \frac{1}{\rho}} \Big). \tag{9.9}$$

On the other hand, the rate of UE_i in an OMA system (assuming the transmit power and radio resource are equally allocated to UE_1 and UE_2) is

$$\tau_i^o = \frac{1}{2}\log_2(1+\frac{\frac{1}{2}c_iP_0}{\frac{1}{2}\sigma^2}) = \frac{1}{2}\log_2(1+c_i\rho). \tag{9.10}$$

9.2.3 Power Control Parameter

Since selective pairing scheme is applied in this work, the performance of each UE (without energy harvesting) can be guaranteed to be better than that in OMA if setting power control parameter ϵ properly. To guarantee the rate of UE_1 in NOMA is no less than that in OMA, i.e., $\tau_1 \geq \tau_1^o$, the following condition needs to be met.

$$\begin{aligned} &\log_2(1+\epsilon c_1\rho) \geq \frac{1}{2}\log_2(1+c_1\rho), \\ &\Rightarrow \epsilon \geq \frac{1}{\sqrt{1+c_1\rho}+1}. \end{aligned} \tag{9.11}$$

Similarly, for UE_2, ϵ needs to satisfy $\tau_2 \geq \tau_2^o$. Thus the following condition needs to be met.

$$\begin{aligned} &\log_2\left(1+\frac{(1-\epsilon)c_2}{\epsilon c_2+\frac{1}{\rho}}\right) \geq \frac{1}{2}\log_2(1+c_2\rho), \\ &\Rightarrow \epsilon \leq \frac{1}{\sqrt{1+c_2\rho}+1}. \end{aligned} \tag{9.12}$$

Since $c_1 \geq T_1$, $c_2 \leq T_2$, and $T_2 < T_1$ as predefined conditions for NOMA grouping, (9.11) and (9.12) can be satisfied simultaneously by setting

$$\epsilon = \frac{a}{\sqrt{1+T_1\rho}+1} + \frac{1-a}{\sqrt{1+T_2\rho}+1}, \tag{9.13}$$

where $a \in [0,1]$ is a tuning parameter to make sure $\epsilon \in [\frac{1}{\sqrt{1+T_1\rho}+1}, \frac{1}{\sqrt{1+T_2\rho}+1}]$. Selecting ϵ that satisfies $\epsilon \leq \frac{1}{\sqrt{1+T_2\rho}+1} < 0.5$ can ensure that more transmission power is allocated to the weak user UE_2, as what has been done in most existing NOMA schemes.

9.3 Dynamic Power Splitting Analysis

In this chapter, a dynamic power splitting scheme is proposed for a NOMA system with SWIPT. With the proposed scheme UEs can harvest the maximum amount of energy while still achieve the same data rates as what can be achieved in an OMA system. In this section, the analysis of the power splitting coefficient β_i, which is a key parameter in the proposed scheme to help achieve the maximum energy harvesting, is provided at first. The average amount of harvested energy is derived afterward.

9.3.1 Dynamic Power Splitting

β_i is used to determine the ratio of received power that can be used for energy harvesting. In the proposed power splitting scheme, β_i is a variable that can be dynamically tuned to harvest the maximum amount of energy under the condition that the data rate performance of NOMA is the same as OMA, i.e., $\tau_i = \tau_i^o, \forall\, i$. As β_i changes statistically, the CDF of β_i, which reflects the statistical distribution of the power used for energy harvesting, is derived at first.

To guarantee that UE_2 in a NOMA with SWIPT system achieves at least the same data rate as in an OMA system, the selection of β_2 value needs to meet the constraint $\tau_2 \geq \tau_2^o$. As τ_2 is a monotonic function of β_2, β_2 that maximizes the harvested energy can be determined by setting $\tau_2 = \tau_2^o$. Solving the equation results in the following expression of β_2:

$$\begin{aligned} &\log_2\left(1 + \frac{(1-\beta_2)(1-\epsilon)c_2}{(1-\beta_2)\epsilon c_2 + \frac{1}{\rho}}\right) = \frac{1}{2}\log_2(1 + c_2\rho), \\ &\Rightarrow \beta_2 = 1 - \frac{1}{1 + (1-\epsilon)\sqrt{1 + c_2\rho} - \epsilon(1 + c_2\rho)}. \end{aligned} \tag{9.14}$$

From (9.14) one can see that β_2 is a function of channel condition c_2, transmitting SNR ρ, and power control parameter ϵ. The amount of energy that can be harvested at UE_2 is affected by these parameters altogether. As $\beta_2 \in [0, 1)$ is given, the right side of (9.14)

needs to satisfy

$$0 \leq 1 - \frac{1}{1 + (1-\epsilon)\sqrt{1 + c_2\rho} - \epsilon(1 + c_2\rho)} < 1,$$
$$\Rightarrow c_2 \leq \frac{1 - 2\epsilon}{\rho\epsilon^2}. \tag{9.15}$$

Since $\frac{1-2\epsilon}{\rho\epsilon^2}$ is a monotonic decreasing function on ϵ and $\epsilon <= \frac{1}{\sqrt{1+T_2\rho}+1}$, the minimum value of $\frac{1-2\epsilon}{\rho\epsilon^2}$ is T_2. Given $c_2 \leq T_2$, constraint (9.15) is always satisfied. Further based on (9.14), the CDF of β_2 can be derived as

$$\begin{aligned} F_{\beta_2}(x) &= \mathbb{P}\Big[1 - \frac{1}{1 + (1-\epsilon)\sqrt{1 + c_2\rho} - \epsilon(1 + c_2\rho)} < x\Big] \\ &= \mathbb{P}\Big[\big(\sqrt{1 + c_2\rho} - \frac{1-\epsilon}{2\epsilon}\big)^2 > \big(\frac{1-\epsilon}{2\epsilon}\big)^2 - \frac{x}{\epsilon(1-x)}\Big]. \end{aligned} \tag{9.16}$$

By observing (9.16) one can find $F_{\beta_2}(x) = 1$ if

$$\begin{aligned} &\big(\frac{1-\epsilon}{2\epsilon}\big)^2 - \frac{x}{\epsilon(1-x)} < 0 \\ &\Rightarrow x > \Big(\frac{1-\epsilon}{1+\epsilon}\Big)^2, \end{aligned} \tag{9.17}$$

which says that β_2 is upper bounded by $\big(\frac{1-\epsilon}{1+\epsilon}\big)^2$. For $x \leq \big(\frac{1-\epsilon}{1+\epsilon}\big)^2$, (9.16) can be further proceeded to

$$\begin{aligned} &= \mathbb{P}\Big[\sqrt{1 + c_2\rho} - \frac{1-\epsilon}{2\epsilon} > \sqrt{\big(\frac{1-\epsilon}{2\epsilon}\big)^2 - \frac{x}{\epsilon(1-x)}}\Big] \\ &+ \mathbb{P}\Big[\sqrt{1 + c_2\rho} - \frac{1-\epsilon}{2\epsilon} < -\sqrt{\big(\frac{1-\epsilon}{2\epsilon}\big)^2 - \frac{x}{\epsilon(1-x)}}\Big] \\ &= 1 - F_{c_2}\Big(\frac{1}{\rho}\Big(\frac{1-\epsilon}{2\epsilon} + \sqrt{\big(\frac{1-\epsilon}{2\epsilon}\big)^2 - \frac{x}{\epsilon(1-x)}}\Big)^2 - \frac{1}{\rho}\Big) \\ &+ F_{c_2}\Big(\frac{1}{\rho}\Big(\frac{1-\epsilon}{2\epsilon} - \sqrt{\big(\frac{1-\epsilon}{2\epsilon}\big)^2 - \frac{x}{\epsilon(1-x)}}\Big)^2 - \frac{1}{\rho}\Big), \end{aligned} \tag{9.18}$$

where $F_{c_2}(x)$ is given in (9.6). In summary, the full expression of $F_{\beta_2}(x)$ is

$$F_{\beta_2}(x) = \begin{cases} 1, \quad \text{if } x > \left(\frac{1-\epsilon}{1+\epsilon}\right)^2; \\ 1 - F_{c_2}\left(\frac{1}{\rho}\left(\frac{1-\epsilon}{2\epsilon} + \sqrt{\left(\frac{1-\epsilon}{2\epsilon}\right)^2 - \frac{x}{\epsilon(1-x)}}\ \right)^2 - \frac{1}{\rho}\right) \\ +F_{c_2}\left(\frac{1}{\rho}\left(\frac{1-\epsilon}{2\epsilon} - \sqrt{\left(\frac{1-\epsilon}{2\epsilon}\right)^2 - \frac{x}{\epsilon(1-x)}}\ \right)^2 - \frac{1}{\rho}\right), \text{otherwise.} \end{cases} \tag{9.19}$$

Different from UE_2, which only needs to decode x_2, UE_1 needs to decode x_2 first in order to decode its own message x_1. Therefor, β_1 that maximizes the harvested energy can be formulated as

$$\underset{\beta_1}{\text{maximize}} \quad \beta_1 \tag{9.20a}$$

$$\text{subject to} \quad \tau_{1\to 2} \geq \tau_2, \tag{9.20b}$$

$$\tau_1 \geq \tau_1^o. \tag{9.20c}$$

Note that τ_2 in (9.20b) is set to $\tau_2 = \tau_2^o$ to enable energy harvesting at UE_2. Hence constraint (9.20b) can be modified to $\tau_{1\to 2} \geq \tau_2^o$. Furthermore, it is proved that $\tau_{1\to 2} \geq \tau_2^o$ always holds when $\tau_1 \geq \tau_1^o$ in appendix 9.A. Therefore, constraint (9.20b) is eliminated and one can research β_1 to maximize the harvested energy by equivalently solving the equation $\tau_1 = \tau_1^o$, which gives

$$\log_2\left(1 + (1-\beta_1)\epsilon c_1 \rho\right) = \frac{1}{2}\log_2(1 + c_1\rho),$$
$$\beta_1 = 1 - \frac{\sqrt{1 + c_1\rho} - 1}{c_1 \epsilon \rho}. \tag{9.21}$$

As $\beta_1 \in [0,1)$, the right side of (9.21) needs to be greater than 0, which means the following constraint needs to be satisfied:

$$\begin{aligned} & 1 - \frac{\sqrt{1+c_1\rho}-1}{c_1\epsilon\rho} \geq 0 \\ & \Rightarrow c_1 \geq \frac{1-2\epsilon}{\rho\epsilon^2}. \end{aligned} \tag{9.22}$$

$\frac{1-2\epsilon}{\rho\epsilon^2}$ is present in (9.15). Since $c_1 \geq T_1$ and $\frac{1-2\epsilon}{\rho\epsilon^2} \leq T_1$ when $\epsilon \in [\frac{1}{\sqrt{1+T_1\rho}+1}, \frac{1}{\sqrt{1+T_2\rho}+1}]$, (9.22) is always satisfied. The PDF of β_1 can be derived as

$$\begin{aligned} F_{\beta_1}(x) &= \mathbb{P}[\bar{\beta_1} < x] \\ &= \mathbb{P}\Big[1 - \frac{\sqrt{1+c_1\rho}-1}{c_1\epsilon\rho} < x\Big] \\ &= \mathbb{P}\Big[c_1 < \frac{1-2\epsilon+2\epsilon x}{(1-x)^2\epsilon^2\rho}\Big] \\ &= F_{c_1}\Big(\frac{1-2\epsilon+2\epsilon x}{(1-x)^2\epsilon^2\rho}\Big), \end{aligned} \tag{9.23}$$

where $F_{c_1}(x)$ is provided in (9.5).

9.3.2 Average Maximum Harvested Energy

Average maximum harvested power is an important metric to evaluate the amount of energy that can be harvested. Based on (9.4), the average maximum energy (normalized to the transmission block duration) harvested by UE_i is

$$E_i = \zeta P_0 \mathbb{E}[c_i\beta_i], \tag{9.24}$$

where $\zeta \in [0,1]$ is the energy harvesting coefficient denoting the conversion efficiency from RF signal to harvested energy. For the convenience of analysis, it is assumed that $\zeta = 1$. The energy harvested from AWGN is considered negligible. Simplified linear energy harvesting model is applied here to provide insights on how much energy can be harvested under the proposed scheme. It is worth pointing out that non-linear energy harvesting model [84]

can be more precise in modeling the power-in-power-out relationship in the current wireless charging technologies, which is not the study focus of this chapter. The average maximum harvested power for UE_1 and UE_2 are expressed as

$$E_1 = \zeta P_0 \cdot \left(T_1 - l1 + \int_{T_1}^{\infty} \frac{1 - F_C(t)}{1 - F_C(T_1)} dt - \int_{l_1}^{\infty} \frac{1 - F_C(G_1(t))}{1 - F_C(T_1)} dt \right), \tag{9.25}$$

$$E_2 = \zeta P_0 \cdot \left(\int_0^{T_2} \left(1 - \frac{F_C(t)}{F_C(T_2)} \right) dt - \int_0^{l_2} \left(1 - \frac{F_C(\frac{G_2(t)^2 - 1}{\rho})}{F_C(T_2)} \right) dt \right), \tag{9.26}$$

where

$$\begin{aligned} G_1(t) &= \frac{(\epsilon\rho t + 1)^2 - 1}{\rho}, \\ G_2(t) &= \frac{(1-\epsilon)t + \sqrt{(1-\epsilon)^2 t^2 + 4(\frac{1}{\rho} + t)(\frac{1}{\rho} + \epsilon t)}}{\frac{2}{\rho} + 2\epsilon t}, \\ l_1 &= \frac{\sigma^2(\sqrt{1 + T_1\rho} - 1)}{\epsilon}, \\ l_2 &= \frac{T_2}{1 + (1-\epsilon)\sqrt{1 + T_2\rho} - \epsilon(1 + T_2\rho)}. \end{aligned}$$

The details of the derivation can be found in appendix 9.B.

9.4 Numerical Evaluation

In this section, system performance is numerically evaluated based on both mathematical analysis and simulations. The radius of the cell R is set to 10 m and transmit SNR ρ is 30 dB unless otherwise specified. Thresholds for NOMA group user selection are set as $T_1 = -27$ dB and $T_2 = -30$ dB. The tuning parameter a, which is used to tune power control parameter ϵ from $\frac{1}{\sqrt{1+T_1\rho}+1}$ to $\frac{1}{\sqrt{1+T_2\rho}+1}$, is fixed at 0.5 unless otherwise specified.

In Figure 9.1 CDFs of β_1 and β_2 from both analysis and simulations are plotted. By comparing Figure 9.1(a) and Figure 9.1(b) one can see that the distribution of β_1 is almost uniform within the range $(0, 1)$; in contrast, β_2 is bounded in a narrow range, which is consistent to our derived result in (9.19). This observation, on one hand, indicates that dynamic scheme is necessary for UE_1 to harvest as much energy as possible while guaranteeing QoS (data rate) requirement. On the other hand, a static scheme may be enough for UE_2 to harvest approximately the same amount of energy as what a dynamic scheme can do. However, a static scheme cannot guarantee the data rate and hence may cause outages, i.e., data rate fails to meet a minimum requirement. More comparisons between a dynamic scheme and a static scheme is an interesting topic and it is left for future work. When allocating more transmit power to UE_1, e.g., changing a from 1 to 0, the CDF of β_1 is shifted towards right meanwhile the CDF of β_2 is shifted towards left. This observation follows the intuition that UEs being allocated more transmit power can harvest more energy. Also, both β_1 and β_2 can have a lower bound, indicating that there is a minimum ratio of the received power can be harvested under the proposed scheme. These lower bound values are affected by a. Therefore, a can be used to control the fairness of the harvested energy between two NOMA UEs.

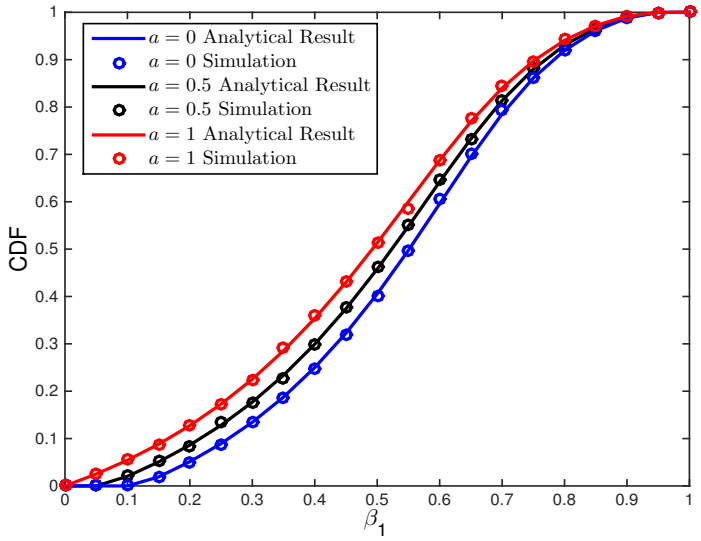

(a)

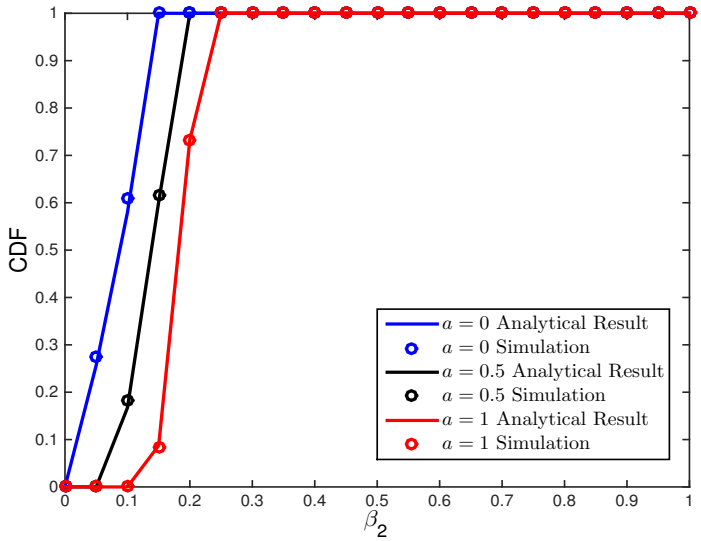

(b)

Fig. 9.1: CDFs of β_1 and β_2 with different values of tuning parameter a.

Figure 9.2 presents the analytical results of average harvested energy and demonstrates the relationship between the harvested energy and transmit SNR ρ. It is assumed that AWGN is invariant and ρ changes with the transmitting power P_0. The power control parameter ϵ used for each ρ is different due to the fact that the range of ϵ is affected by ρ, as shown in (9.13), whereas the tuning parameter a is fixed at 0.5 to ensure the fairness between UE_1 and UE_2. From the figure, one can see the average harvested energy increases linearly along with the transmitting power for both UE_1 and UE_2. However, the energy harvested at UE_2 is smaller than that at UE_1 by almost 3 orders of magnitude, which indicates that applying SWIPT to UEs with a good channel condition is more beneficial than applying that to UEs with a poor channel condition.

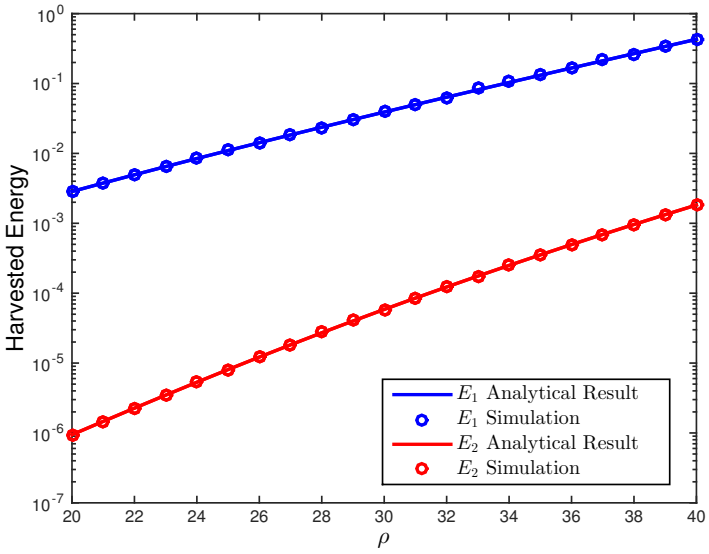

Fig. 9.2: Average harvested energy vs. transmit SNR ρ.

Figure 9.3 investigates the impact of cell size R on the average harvested energy. One can see that the harvested energy at UE_1 decreases almost exponentially along with the cell size. This observation shows that it is more attractive to apply energy harvesting in a densely deployed network within which the size of each cell is small. However, a single cell scenario model may not be able to provide accurate results for a densely deployed network because densely deployed network tends to be interference limited and inter-cell interference needs to be considered deliberately. Although a multi-cell framework is developed in Chapter 8, it is not directly applicable to analyze some technologies such as SWIPT presented in this chapter. The future work is to extend the content presented in this chapter to a densely deployed network and explicitly take the impact of inter-cell interference into consideration.

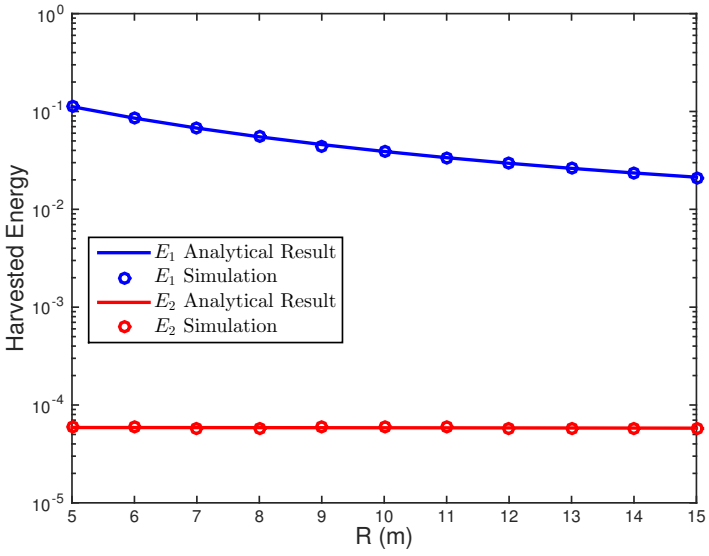

Fig. 9.3: Average harvested energy vs. cell size R.

9.5 Conclusion

In this chapter, a new dynamic power splitting scheme is proposed for downlink NOMA system with SWIPT. With the proposed scheme, UEs can harvest the maximum amount of energy while still achieve the same data rate as what can be achieved in the traditional OMA schemes. The performance of the proposed scheme is evaluated by the CDF of power splitting coefficient and the average harvested energy. Analytical results are derived to provide insights and validated by simulations. Numerical results demonstrate that with the proposed scheme users with good channels can benefit from SWIPT on both energy harvesting and data rate satisfaction while users with poor channels can benefit on data rate satisfaction. The future work of the content in this chapter is to take the dense deployment into consideration, where interference from other cells can be another dominant factor to impact the proposed scheme.

Appendix

9.A

This appendix proves that $\tau_{1\to 2} > \tau_2^o$ always hold when $\tau_1 > \tau_1^o$. The condition $\tau_1 > \tau_1^o$ is the same as

$$\begin{aligned} &\log_2(1+(1-\beta_1)\epsilon c_1\rho) > \frac{1}{2}\log_2(1+c_1\rho), \\ \Rightarrow \qquad &c_1 > \frac{1-2\epsilon(1-\beta_1)}{(1-\beta_1)^2\epsilon^2\rho}, \end{aligned} \tag{9.27}$$

and the condition $\tau_{1\to 2} > \tau_2^o$ is the same as

$$\begin{aligned} &\log_2\left(1+\frac{(1-\beta_1)(1-\epsilon)c_1}{(1-\beta_1)\epsilon c_1+\frac{1}{\rho}}\right) > \frac{1}{2}\log_2(1+c_2\rho), \\ \Rightarrow \qquad &c_1 > \frac{\sqrt{1+c_2\rho}-1}{\rho(1-\beta_1)(1-\epsilon\sqrt{1+c_2\rho})}. \end{aligned} \tag{9.28}$$

Therefore, the original proof is equivalent to the following proof.

$$\begin{aligned} &\frac{1-2\epsilon(1-\beta_1)}{(1-\beta_1)^2\epsilon^2\rho} \geq \frac{\sqrt{1+c_2\rho}-1}{\rho(1-\beta_1)(1-\epsilon\sqrt{1+c_2\rho})}, \\ \Rightarrow \qquad &1-\beta_1 \leq \frac{1-\epsilon\sqrt{1+c_2\rho}}{\epsilon(2-\epsilon-\epsilon\sqrt{1+c_2\rho})}. \end{aligned} \tag{9.29}$$

As $\beta_1 \in [0,1]$, (9.29) is always true if

$$\frac{1-\epsilon\sqrt{1+c_2\rho}}{\epsilon(2-\epsilon-\epsilon\sqrt{1+c_2\rho})} \geq 1. \tag{9.30}$$

By solving the quadratic inequality above in term of ϵ, one can see that (9.30) is true when $\epsilon \leq \frac{1}{\sqrt{1+c_2\rho}+1}$. Since $c_2 \leq T_2$ and $\epsilon \leq \frac{1}{\sqrt{1+T_2\rho}+1}$, constraint (9.29) always holds the selected power control parameter ϵ is in the range derived above. By summarizing the derivations above, one can conclude that $\tau_{1\to 2} > \tau_2^o$ always hold when $\tau_1 > \tau_1^o$. □

9.B

As the expression of $\bar{\beta}_1$ is given in (9.21), the average maximum harvested energy of UE_1 is

$$\begin{aligned}
E_1 &= \zeta P_0\Big(\mathbb{E}[c_1] - \mathbb{E}[\frac{\sqrt{1+c_1\rho}-1}{\epsilon\rho}]\Big) \\
&\overset{(a)}{=} \zeta P_0\Big(\int_0^\infty \mathbb{P}[c_1 > t]dt - \int_0^\infty \mathbb{P}[c_1 > \frac{(\epsilon\rho t+1)^2-1}{\rho}]dt\Big) \\
&= \zeta P_0\Big(\int_0^\infty \big(1 - F_{c_1}(t)\big)dt - \int_0^\infty \big(1 - F_{c_1}(G_1(t))\big)dt\Big) \\
&\overset{(b)}{=} \zeta P_0\Big(T_1 - l1 + \int_{T_1}^\infty \Big(1 - \frac{F_C(t) - F_C(T_1)}{1 - F_C(T_1)}\Big)dt \\
&\qquad - \int_{l_1}^\infty \Big(1 - \frac{F_C(G_1(t)) - F_C(T_1)}{1 - F_C(T_1)}\Big)dt\Big),
\end{aligned}$$

where (a) is met as $\mathbb{E}[X] = \int_{t>0} \mathbb{P}(X > t)dt$ for a positive random variable X and (b) uses the CDF of c_1 in (9.5). E_2 is derived in the same approach as E_1.

CHAPTER 10

Dense Cellular Network Analysis with LoS/NLoS Propagation and Bounded Path-loss Model

This chapter developed a framework to analyze the coverage probability in the dense wireless networks. The study is based on channel models that incorporate line-of-sight (LoS)/non-line-of-sight (NLoS) propagation and use the bounded path-loss model (BPM). Further by using the dominant base station (BS) based approach the conditional distributions of inter-cell interference in the dense network is derived. Compared with the existing works where the interference is normally characterized by its Laplace transform, the dominant BS-based approximation together with the BPM and LoS/NLoS channel models is more convenient and also more accurate to evaluate new 5G wireless technologies such as radio frequency (RF) energy harvesting and simultaneous information and energy transfer (SWIPT). The numerical results show that the developed analytical model achieves high accuracy for studying the performance of dense cellular networks.

10.1 Introduction

Ultra-dense networks (UDNs) are envisaged as a key technology for 5G wireless systems to achieve high capacity [1]. In order to evaluate the system-level performance of a UDN, accurate and tractable analytical models are actively pursued and explored. Stochastic geometry tools have been widely used to achieve tractable yet accurate analytical results in wireless cellular networks. For instance, a powerful stochastic geometry framework is provided in [3], in which the coverage probability and average achievable rate are derived by assuming a channel model comprised of single slope path-loss and Rayleigh fading.

Although the single-slope path-loss model is able to provide reliable results for sparse networks, it is not accurate enough for networks with very high densities. Therefore, new channel model research has attracted extensive attention. Authors of [85] extended the

work in [3] to a multi-slops path-loss model where paths with different distance ranges are subject to different path-loss exponents. The mathematical results in [85] showed that the signal-to-interference-plus-noise ratio (SINR) varies along with network density and the optimal density that maximizes SINR exists. In [86] authors proposed a model where the path-loss exponent changes as a function of the distance between the base station (BS) and user. In addition to modifying path-loss model, [87] and [88] also considered varying small scale fading models for LoS and NLoS propagations.

In most of the previous works using stochastic geometry model, inter-cell interference is characterized by its Laplace transform, which is normally denoted as $\mathcal{L}_I(s)$. Although $\mathcal{L}_I(s)$ is sufficient to evaluate metrics such as SINR, coverage probability, and average achievable rate [3, 85–88], the distribution of interference is specifically needed to evaluate some new metrics in 5G systems. For instance, in order to derive the joint probability for successfully received information and power in SWIPT [89] and the joint coverage probability in an energy harvesting network [90], the probability distribution of interference is needed. In [89], the cumulative distribution function (CDF) of interference is acquired by deriving $\mathcal{L}^{-1}\big(\frac{\mathcal{L}_I(s)}{s}\big)$, which is the inverse Laplace transform of $\frac{\mathcal{L}_I(s)}{s}$. However, $\mathcal{L}^{-1}\big(\frac{\mathcal{L}_I(s)}{s}\big)$ is only computable for simple scenarios in which only NLoS propagation is considered and the interference source can be arbitrarily close to the receiver. Dominant BS-based approach is adopted in [90] to provide tractable results. The study in [90] only considered NLoS propagation and used unbounded path-loss model (UPM). Despite its simplicity, UPM cannot accurately characterize the channel power gain in dense networks [91]. In particular, UPM artificially increases the received power when the transmit distance is less than 1 m, which is not a practical condition. Therefore, bounded path-loss models (BPMs) are deemed desirable for dense networks, where the transmission distance tends to be small, to generate more realistic results.

To address the problems mentioned above, this chapter develops an analytical model for dense cellular networks based on the dominant BS-based approach. Specifically, LoS/NLoS propagation is taken into consideration and BPMs are applied in the analysis. The con-

ditional interference distributions are derived, which can be applied in the more general mathematical analysis. Before the content of this chapter is published in [92], the accuracy of the dominant BS-based approach under dense scenarios is not investigated by any existing work. The numerical results demonstrate that the developed analytical model is accurate in a wide range of network densities.

10.2 System Model

This chapter considers a downlink cellular network where the locations of BSs are modeled as a homogeneous Poisson Point Process (PPP) $\Phi = \{b_i\}$, $i \in \{0, 1, ...\}$, of an intensity λ on the Euclidean plane. b_i denotes the location of the ith BS. To simplify the expression, throughout this chapter b_i is also used to represent the ith BS. All BSs are assumed to be equipped with a single antenna and transmit at a fixed power P. A heavy load scenario is considered, which means all the BSs are fully loaded at any given time. It is assumed that each user is also equipped with a single antenna and the user locations follow a stationary point process that is independent of Φ. Closest BS association rule is considered in this work, i.e., each user is associated with the geographically closest BS. The system assumes a frequency reuse factor 1, hence the same frequency resources are used in all the cells. The radio resources are partitioned into a number of sub-bands and resources are allocated in the unit of sub-band. For notational simplicity, the bandwidth of each sub-band is normalized to 1. The analysis of user performance focuses on a typical sub-band by assuming flat fading channels across sub-bands. Without loss of generality, the analysis presented in this chapter is for a typical user located at the origin of the plane as the statistics seen from a PPP is independent of the test location according to Slivnyak's Theorem [75].

It's assumed that a path from a BS to a user can be either a LoS or an NLoS path independent of other BS paths and also regardless of its operation mode (serving path or interfering path). Distance-dependent LoS/NLoS probability function $p_L(r_i)/p_N(r_i)$ is considered in this chapter, i.e., the probability that the ith BS experiences a LoS propagation depends on the distance from b_i to the user, which is denoted as $r_i \triangleq ||b_i||$. The probability

function adopted in the ITU-R UMi model [93] is used here,

$$p_{_L}(r_i) = \min(\frac{18}{r_i}, 1)(1 - e^{-\frac{r_i}{36}}) + e^{-\frac{r_i}{36}}, \tag{10.1}$$

$p_{_N}(r_i) = 1 - p_{_L}(r_i)$. The channel gain can be expressed as $l(r_i)g_i$, where $l(r_i)$ denotes the path-loss between b_i and the typical user, g_i denotes the corresponding channel power fading gain from small scale fading. BPM is adopted for $l(r_i)$. The path-loss functions for LoS and NLoS scenarios are respectively expressed as

$$l(r_i) \triangleq \begin{cases} l_{_L}(r_i) = (1 + r_i^{\alpha_{_L}})^{-1}, & \text{if } b_i \text{ is in LoS,} \\ l_{_N}(r_i) = (1 + r_i^{\alpha_{_N}})^{-1}, & \text{if } b_i \text{ is in NLoS;} \end{cases} \tag{10.2}$$

where $\alpha_{_L}$ and $\alpha_{_N}$ are path-loss exponents for LoS and NLoS respectively with $\alpha_{_N} > \alpha_{_L} > 2$. The BPM used here is a typical one widely applied in the existing works [91]. Other BPMs such as $(1+r)^{-\alpha}$ and $\min(1, r^{-\alpha})$ can also be adopted to the analysis in this chapter readily. It is assumed that the small scale fading is Nakagami-m distributed for LoS and Rayleigh distributed for NLoS. Hence the channel fading gain can be expressed as

$$g_i \triangleq \begin{cases} g_{_{L,i}} \sim \Gamma(m_i, \frac{1}{m_i}), & \text{if } b_i \text{ is in LoS,} \\ g_{_{N,i}} \sim \exp(1), & \text{if } b_i \text{ is in NLoS;} \end{cases} \tag{10.3}$$

where $\Gamma(m, \frac{1}{m})$ denotes the Gamma distribution with shape m and scale $\frac{1}{m}$; $\exp(1)$ denotes the exponential distribution with mean 1. Note that the exponential distribution is a special case of Gamma distribution with $m = 1$. The CDF of $g_{_{L,i}}$ is given by

$$F_{g_{_{L,i}}}(x) \triangleq \frac{\gamma(m_i, m_i x)}{\Gamma(m_i)}, \tag{10.4}$$

where $\Gamma(S) = \int_0^\infty t^{s-1}e^{-t}dt$ is the gamma function and $\gamma(s,x) = \int_0^x t^{s-1}e^{-t}dt$ is the lower incomplete gamma function. When m_i is an integer, (10.4) can be rewritten as

$$F_{g_{L,i}}(x) \overset{m_i \in \mathbb{Z}^+}{=} 1 - e^{-m_i x} \sum_{k=0}^{m_i-1} \frac{(m_i x)^k}{k!}. \tag{10.5}$$

In this chapter, it is assumed that m_i is always rounded to the closest integer to provide a good approximation of Rician distribution [88]. Therefore, (10.4) and (10.5) are used interchangeably to facilitate the derivation. The CDF of $g_{N,i}$ is given by

$$F_{g_{N,i}}(x) \triangleq 1 - \exp(-x). \tag{10.6}$$

It is assumed that the fading gains of all the channels are i.i.d. with the same parameter, i.e., $m_i = m$, $\forall i$. Here the subscript of the parameter is retained to facilitate the derivation in the later context.

Without loss of generality, BSs are ordered based on their distance to the typical user in ascending order with 0-indexing. b_0 is the associated BS, b_1 is the closest interfering BS, b_2 is the second closest interfering BS, and henceforth. The SINR of the typical user is given by

$$SINR = \frac{P g_0 l(r_0)}{P\sum_{i=1}^{\infty} I_i + \sigma^2} = \frac{S}{\sum_{i=1}^{\infty} I_i + \rho}, \tag{10.7}$$

where σ^2 is a constant corresponding to noise power and $\rho = \frac{\sigma^2}{P}$ is the inverse of transmit signal-to-noise ratio (SNR). $S = g_0 l(r_0)$ denotes the desired signal from b_0. $P\sum_{i=1}^{\infty} I_i$ is the summation of all inter-cell interference and $I_i = g_i l(r_i)$ denotes the interference from b_i normalized by transmit power P.

10.3 Coverage Probability

The coverage probability is defined as $p_{cov}(T) = \mathbb{P}[SINR > T]$, which can be considered as the probability that the received SINR at the typical user is greater than a certain threshold T. Other interpretations of the coverage probability can be found in [3]. To analyze the coverage probability, $\sum_{i=1}^{\infty} I_i$ in (10.7) needs to be characterized. In most of

existing works, $\sum_{i=1}^{\infty} I_i$ is characterized through its Laplace transform [3, 88], which may be unwieldy under some scenario. Dominant BS-based approach is useful when the exact analysis is hard to acquire or too complicated [90]. By using dominant BS-based approach, $\sum_{i=1}^{\infty} I_i$ is approximated by the interference from the closest interfering BS (b_1) plus the conditional mean of the rest terms. Through this way the exact stochastic characteristics of interference, i.e., CDF and probability density function (PDF), are accessible. The dominant BS-based approximation can be mathematically expressed as

$$\begin{aligned}\sum_{i=1}^{\infty} I_i &\approx I_1 + \mathbb{E}[\sum_{i=2}^{\infty} I_i | r_1] \\ &\approx I_1 + \mathbb{E}[\sum_{i=2}^{\infty} I_i | r_1 = \bar{r}_1]. \end{aligned} \tag{10.8}$$

When only NLoS propagation is considered and UPM is adopted, $\mathbb{E}[\sum_{i=2}^{\infty} I_i | r_1]$ after first approximation can be expressed as a function of r_1 in a closed form [90]. However, the closed form expression may be not available under other channel models such as LoS/NLoS and BPM, as shown in Appendix 10.A. Therefore, in this chapter $\mathbb{E}[\sum_{i=2}^{\infty} I_i | r_1]$ is further approximated to a constant $\mathbb{E}[\sum_{i=2}^{\infty} I_i | r_1 = \bar{r}_1]$ where $\bar{r}_1 = \mathbb{E}[r_1]$. $\mathbb{E}[\sum_{i=2}^{\infty} I_i | r_1 = \bar{r}_1]$ is computed in Appendix 10.A and the numerical results in numerical results section validate the accuracy of the approximation here.

The approximated coverage probability is

$$p_{cov}(T) \approx \mathbb{P}\Big[\frac{S}{I_1 + C} > T\Big], \tag{10.9}$$

where $C = \mathbb{E}[\sum_{i=2}^{\infty} I_i | r_1 = \bar{r}_1] + \rho$ is introduced here to simplify the expression. To compute (10.9), the complementary cumulative distribution function (CCDF) of desired signal S and

the PDF of I_1 are desired. The CDF of I_i conditioned on r_i can be derived as

$$\begin{aligned} F_{I_i|r_i}(x) &= \mathbb{P}[g_i l(r_i) < x | r_i] \\ &\overset{(a)}{=} p_{_L}(r_i)\mathbb{P}[g_{L,i} < x l_{_L}(r_i)^{-1}] + p_{_N}(r_i)\mathbb{P}[g_{N,i} < x l_{_N}(r_i)^{-1}] \\ &\overset{(b)}{=} p_{_L}(r_i)\frac{\gamma(m_i, m_i x l_{_L}(r_i)^{-1})}{\Gamma(m_i)} + p_{_N}(r_i)(1 - e^{(-x l_{_N}(r_i)^{-1}))}. \end{aligned} \tag{10.10}$$

(a) follows from replacing $l(r_i)$ and g_i by their counterparts in (10.2) and (10.3) as I_i can be either LoS or NLoS. $p_{_L}(r_i)$ is given in (10.1). (b) uses CDFs of $g_{_{L,i}}$ and $g_{_{N,i}}$, which are given in (10.4) and (10.6). By taking the derivative of (10.10), PDF of I_i conditioned on r_i can be obtained as

$$f_{I_i|r_i}(x) = p_{_L}(r_i)\eta(m_i, l_{_L}(r_i), x) + p_{_N}(r_i)\eta(1, l_{_N}(r_i), x), \tag{10.11}$$

where $\eta(m, l(r), x) = \frac{(ml(r)^{-1})^m x^{m-1}}{\Gamma(m_i)} \exp(-ml(r)^{-1}x)$.

The CCDF of S conditioned on r_0 can be derived in a similar way to the CDF of I_i in (10.10). The only difference is that the CDF of $g_{L,i}$ in (10.5) instead of in (10.4) is used to facilitate the derivation.

$$\begin{aligned} \bar{F}_{S|r_0}(x) &= 1 - \mathbb{P}[g_0 l(r_0) < x | r_0] \\ &= p_{_L}(r_0)\mathbb{P}[g_{L,0} > x l_{_L}(r_0)] + p_{_N}(r_0)\mathbb{P}[g_{N,0} > x l_{_N}(r_0)] \\ &= p_{_L}(r_0)\theta(m_0, l_{_L}(r_0), x) + p_{_N}(r_0)\theta(1, l_{_N}(r_0), x), \end{aligned} \tag{10.12}$$

where $\theta(m, l(r), x) = \exp(-mxl(r)^{-1}) \sum_{k=0}^{m-1} \frac{(mxl(r)^{-1})^k}{k!}$.

Conditioned on r_0 and r_1, the approximated coverage probability in (10.9) can be rewritten as

$$\mathbb{P}\Big[\frac{S}{I_1 + C} > T\Big] = \int_{r_0>0}\int_{r_1>r_0} \mathbb{P}[S > T(I_1 + C) | r_0, r_1] \\ f_{r_0,r_1}(r_0, r_1) dr_0 dr_1, \tag{10.13}$$

where $f_{r_0,r_1}(r_0,r_1) = (2\pi\lambda)^2 r_0 r_1 \exp(-\pi\lambda r_1^2)$ is the joint PDF of r_0 and r_1 derived in appendix 10.B. The conditional probability within (10.13) can be further expanded as

$$\begin{aligned}
&\mathbb{P}[S > T(I_1 + C)|r_0, r_1] \\
&= \int_{I_1>0} \mathbb{P}[S > T(I_1 + C)|I_1, r_0, r_1] f_{I_1|r_1}(I_1) dI_1 \\
&= p_{_L}(r_0) p_{_L}(r_1) \Xi(m_0, l_{_L}(r_0), m_1, l_{_L}(r_1)) + \\
&\quad p_{_L}(r_0) p_{_N}(r_1) \Xi(m_0, l_{_L}(r_0), 1, l_{_N}(r_1)) + \\
&\quad p_{_N}(r_0) p_{_L}(r_1) \Xi(1, l_{_N}(r_0), m_1, l_{_L}(r_1)) + \\
&\quad p_{_N}(r_0) p_{_N}(r_1) \Xi(1, l_{_N}(r_0), 1, l_{_N}(r_1)),
\end{aligned} \tag{10.14}$$

where

$$\Xi(m_0, l_{_L}(r_0), m_1, l_{_L}(r_1)) = \int_{I_1>0} \theta(m_0, l_{_L}(r_0), T(I_1 + C)) \eta(m_1, l_{_L}(r_1), I_1) dI_1,$$

and the last step of (10.14) uses the derived PDF and CCDF in (10.11) and (10.12). $\Xi(m_0, l_{_L}(r_0), m_1, l_{_L}(r_1))$ can be computed as

$$\begin{aligned}
\Xi(m_0, l_{_L}(r_0), m_1, l_{_L}(r_1)) &= \underbrace{\frac{(m_1 l_{_L}(r_1)^{-1})^{m_1}}{\Gamma(m_1)} e^{-m_o T C l_{_L}(r_0)^{-1}}}_{A} \\
&\quad \times \int_{I_1>0} \Big(e^{(-m_1 l_{_L}(r_1)^{-1} I_1 - m_0 T l_{_L}(r_0)^{-1} I_1)} \\
&\quad \times \sum_{k=0}^{m_0-1} \frac{(m_0 T (I_1 + C) l_{_L}(r_0)^{-1})^k}{k!} I_1^{m_1-1} \Big) dI_1 \\
&\overset{(a)}{=} A \sum_{k=0}^{m_0-1} \sum_{j=0}^{k} \frac{(m_0 T l_{_L}(r_0)^{-1})^k}{k!} \binom{k}{j} C^{k-j} \\
&\quad \times \int_{I_1>0} e^{(-m_1 l_{_L}(r_1)^{-1} I_1 - m_0 T l_{_L}(r_0)^{-1} I_1)} I_1^{j+m_1-1} dI_1 \\
&\overset{(b)}{=} A \sum_{k=0}^{m_0-1} \sum_{j=0}^{k} \binom{k}{j} \frac{(m_0 T l_{_L}(r_0)^{-1})^k \Gamma(j + m_1) C^{k-j}}{k! (m_1 l_{_L}(r_1)^{-1} + m_0 T l_{_L}(r_0)^{-1})^{j+m_1}}.
\end{aligned} \tag{10.15}$$

(a) follows from expanding $(I_1 + C)^k$ to $\sum_{j=0}^{k} \binom{k}{j} I_1^j C^{k-j}$ by using binomial theorem. In

(b) the integration is rearranged by using $\Gamma(S) = \int_0^\infty t^{s-1}e^{-t}dt$. Combining (10.14) and (10.15) with (10.13), the approximated coverage probability is completed. Although only the coverage probability is presented, the developed model can be readily extended to evaluate other metrics such as average achievable rate [3].

10.4 Numerical Evaluation

This section validates the analysis by simulation results. The parameters used in simulations are as follows: $\lambda = 10^{-2}BS/m^2$, $m = 10$, $\alpha_L = 3$, $\alpha_N = 4$, $\frac{1}{\rho} = 50\ dB$. In Figure 10.1 the coverage probability derived in (10.13) is compared with the special case that only LoS or only NLoS propagation is considered. All the simulation results match the analytical results tightly. The analytical results for specific cases can be acquired by modifying the parameters in (10.13). For instance, one can set $m = 1$, $\alpha_L = \alpha_N = 4$ for only NLoS propagation case. From Figure 10.1 one can observe that the coverage probability for the case of only NLoS propagation differs prominently from others. Based on this observation, one can conclude that taking LoS propagation into consideration is crucial to obtain realistic results for dense networks. Another observation is that the coverage probability only considering LoS propagation is very close to that considering LoS/NLoS propagation. This is due to the reason that LoS interference is dominant in a dense network and thus the impact of treating the NLoS signals as LoS signals is rather small. In Figure 10.1 another BPM is also considered, i.e., $l(r) = (1 + r)^{-\alpha}$. The results demonstrate that the coverage probability varies depending on the specific BPM used and the analytical result still matches simulation tightly.

Figure 10.2 presents the coverage probability curves with different network densities. When changing λ from 10^{-4} to 10^{-3}, the coverage is improved due to the shortened transmit distance. When altering λ from 10^{-3} to 1, the interference gradually dominates hence the coverage probability is degraded. The results in Figure 10.2 show that densification does not necessarily always benefit the network performance especially when the BS density is too high. Figure 10.2 also validates that the developed analytical model remains accurate in a wide range of λ.

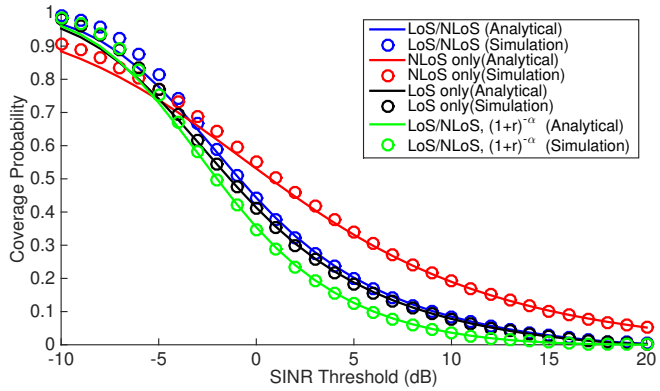

Fig. 10.1: Coverage probability with LoS/NLoS, LoS only and NLoS only propagation.

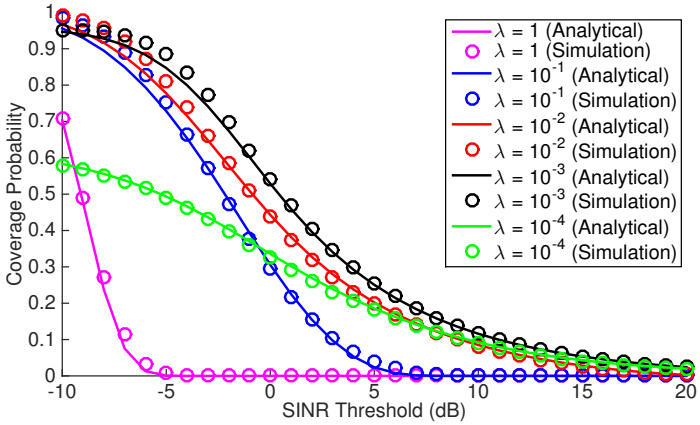

Fig. 10.2: Coverage probability with various network density.

10.5 Conclusion

In this chapter, the coverage probability in a dense network is derived using the stochastic geometry based analytical model. LoS/NLoS propagation is incorporated into channel model and BPM is considered to generate more realistic results for dense networks. Interference distribution can be derived so that it is generally applicable to analyze new technologies in 5G cellular systems. Future study of this framework can explore further simplification to improve tractability and take more 5G features into consideration such as heterogeneous network, millimeter wave, and energy harvesting.

Appendix

10.A

$\mathbb{E}[\sum_{i=2}^{\infty} I_i | r_1]$ is first derived as follows:

$$\mathbb{E}[\sum_{i=2}^{\infty} I_i | r_1] = \mathbb{E}[\sum_{i=2}^{\infty} g_i l(r_i) | r_1] \overset{(a)}{=} \mathbb{E}[\sum_{i=2}^{\infty} l(r_i) | r_1]$$
$$\overset{(b)}{=} 2\pi\lambda \int_{r_1}^{\infty} (P_{_L}(r) l_{_L}(r) + P_{_N}(r) l_{_N}(r)) r dr, \tag{10.16}$$

where (a) comes from the assumption that g_i is independent of $l(r_i)$ and $\mathbb{E}[g_i] = 1$ in both LoS and NLoS scenarios. (b) uses Campbell's theorem for the expectation of a sum over a point process [47, Ch. 4.1] with conversion from Cartesian to polar coordinates. The PDF of nth nearest BS is given in [47, Ch. 2.5] as

$$f_{r_n}(r) = \frac{2(\pi\lambda r^2)^n}{r(n-1)!} \exp(-\pi\lambda r^2). \tag{10.17}$$

The closest interfering BS (b_1) is the 2nd nearest BS and hence

$$\bar{r}_1 = \mathbb{E}[r_1] = \int_0^{\infty} r_1 \cdot 2\pi\lambda r_1^3 e^{-\pi\lambda r_1^2} dr_1 = \frac{1.3293}{\sqrt{\pi\lambda}}. \tag{10.18}$$

$\mathbb{E}[\sum_{i=2}^{\infty} I_i | r_1 = \bar{r}_1]$ is acquired via substituting r_1 in (10.16) by $\bar{r}_1$ above and computed by applying numerical integration.

10.B

The PDF of r_0, which is the distance from typical user to closest BS, is given in [1] as $f_{r_0}(x) = 2\pi\lambda x \exp(-\pi\lambda x^2)$.

By using the null probability of a 2-D PPP, the possibility that no BS is closer than r_1 and further than r_0 is $\mathbb{P}[r_1 > x | r_0] = \exp(-\pi\lambda(x^2 - r_0^2))$.

Therefore, the CDF of r_1 conditioned on r_0 is $F_{r_1|r_0}(x) = 1 - \exp(-\pi\lambda(r_1^2 - r_0^2))$ and the PDF can be found by taking derivative as $f_{r_1|r_0}(x) = 2\pi\lambda x \exp(\pi\lambda(r_0^2 - x^2))$.

Finally by using the chain rule of conditional probability, the joint probability of r_0 and r_1 is

$$f_{r_0,r_1}(r_0, r_1) = f_{r_0}(r_0) f_{r_1|r_0}(r_1) = (2\pi\lambda)^2 r_0 r_1 \exp(-\pi\lambda r_1^2).$$

CHAPTER 11

General Conclusion

In this dissertation, stochastic geometry based mathematical models are developed to analyze the performance of some key 5G mobile technologies. Some schemes are also proposed for 5G technologies and analyzed by using stochastic geometry tools. The specific 5G technologies focused in this dissertation are D2D, NOMA, and UDN.

The main contributions of this dissertation on each of these technologies are:

1. In D2D communication, two schemes are proposed to support underlaid D2D communication in 5G cellular networks. The performance of the proposed schemes is analyzed in a system modeled by PPP and also validated by simulations.

2. In NOMA research, analytical frameworks are developed to evaluate the performance of NOMA for both downlink and uplink 5G dense networks. Distinguished from the existing publications in NOMA, the framework developed in this dissertation is the first one that considers the dense cellular network model with strong inter-cell interference. In addition, the potential of applying SWIPT in a NOMA system is investigated.

3. In the research on UDN, a dominant BS-based approximation framework is developed to address the short-range propagation features UDN. By applying reasonable mathematical approximations, the tractability of the PPP model is preserved while the closed form solution is derived. The numerical results demonstrate that the developed analytical model is accurate in a wide range of network densities.

Most of the research in this dissertation considers a multi-cell scenario, except the research on NOMA with SWIPT in Chapter 9. The reason is that when doing analysis on topics such as energy harvesting and SWIPT, the distribution of the inter-cell interference is desired and this it is not available in the common PPP model. This obstacle is overcome in

the framework developed for UDNs in Chapter 10 by applying appropriate approximations. Therefore, the future work may consider expanding the work on NOMA with SWIPT in Chapter 9 to a multi-cell scenario by using the framework developed for UDNs in Chapter 10.

CURRICULUM VITAE

Zekun Zhang

Published Journal Articles

- Downlink and Uplink Non-Orthogonal Multiple Access in a Dense Wireless Network, Zekun Zhang, Haijian Sun, and Rose Qingyang Hu, *IEEE Journal on Selected Areas in Communications*, vol. 35, no. 12, pp. 2771 - 2784, Dec. 2017.

- Dense Cellular Network Analysis With LoS/NLoS Propagation and Bounded Path Loss Model, Zekun Zhang, and Rose Qingyang Hu, *IEEE Communications Letters*, vol. 22, no. 11, pp. 2386 - 2389, Nov. 2018.

- Challenges and Enabling Technologies in 5G Wearable Communications, Haijian Sun, Zekun Zhang, Rose Qingyang Hu, Yi Qian, *IEEE Vehicular Technology Magazine*, vol. 13, no. 3, pp. 100 - 109, June 2018.

- Joint Spectral Efficiency and Energy Efficiency in FFR based Wireless Heterogeneous Networks, Bei Xie, Zekun Zhang, Rose Qingyang Hu, Geng Wu, and Apostolos Papathanassiou, *IEEE Transactions on Vehicular Technology*, vol. 67, no. 9, pp. 8154-8168, May 2017.

Published Conference Papers

- D2D communication underlay uplink cellular network with fractional frequency reuse, Zekun Zhang, Rose Qingyang Hu, Yi Qian, Apostolos Papathanassiou, and Geng Wu, in *Proc. IEEE Int. Conf. on Design of Reliable CommunicationNetworks(DRCN)*, Mar. 2015.

- D2D Communication Underlay in Uplink Cellular Networks with Fractional Power Control and Fractional Frequency Reuse, Zekun Zhang, Rose Qingyang Hu, Yi Qian, and Apostolos Papathanassiou, in *Proc. IEEE Global Commun. Conf. (GLOBECOM)*, Dec. 2015.

- D2D communication underlay in uplink cellular networks with distance based power control, Zekun Zhang, Rose Qingyang Hu, and Yi Qian, in *Proc. IEEE Int. Conf. on Communications (ICC)*, May 2016.

- Stochastic Geometry Based Performance Study on 5G Non-Orthogonal Multiple Access Scheme, Zekun Zhang, Haijian Sun, Rose Qingyang Hu, and Yi Qian, in *Proc. IEEE Global Commun. Conf. (GLOBECOM)*, Dec. 2016.

- Uplink Non-Orthogonal Multiple Access with Fractional Power Control, Zekun Zhang and Rose Qingyang Hu, in *Proc. IEEE Wireless Commun. & Netw. Conf. (WCNC)*, Mar. 2017.

- Dynamic power splitting between information and power transfer in non-orthogonal multiple access, Rose Qingyang Hu and Zekun Zhang, in *Proc. IEEE Int. Conf. on Wireless Communications and Signal Processing (WCSP)*, Oct. 2017.

- Performance Study on Relay-Assisted Millimeter Wave Cellular Networks, Bei Xie, Zekun Zhang, and Rose Qingyang Hu, in Proceedings of *IEEE Veh. Technol. Conf. (VTC) Spring*, May 2016.

- Spectral Efficiency Analysis in Wireless Heterogeneous Networks, Bei Xie, Zekun Zhang, Rose Qingyang Hu, and Yi Qian, in Proceedings of IEEE ICC IEEE Int. Conf. on Communications (ICC), May 2016.

- Outage and Spectral Efficiency Study in Cooperative Wireless Heterogeneous Networks, Bei Xie, Zekun Zhang, Rose Qingyang Hu, and Yi Qian, in Proceedings of IEEE Int. Conf. on Communications (ICC), May 2017.

- Energy Efficient Relay-Assisted Cell Zooming in a Wireless Heterogeneous Network, Sidhant Chatterjee, Zekun Zhang, and Rose Qingyang Hu, in Proceedings of *IEEE Veh. Technol. Conf. (VTC) Spring*, Sept. 2017.

- Robust Beamforming Design in a NOMA Cognitive Radio Network Relying on SWIPT, Haijian Sun, Fuhui Zhou and Zekun Zhang, in Proceedings of IEEE Int. Conf. on Communications (ICC), May 2018.

- On-the-fly Uplink Training and Code Sequence Design for Cellular Networks, Zekun Zhang, Chenwei Wang, and Haralabos Papadopoulos, submitted to IEEE Int. Conf. on Communications (ICC), 2019.

Awards

- IEEE ICC 2016 Best Paper Award

- IEEE VTC 2016 Best Paper Award

- Outstanding Graduate Research Assistant for ECE Department 2016

- Outstanding Graduate Scholars for the College of Engineering 2016

REFERENCES

[1] J. G. Andrews, S. Buzzi, W. Choi, S. V. Hanly, A. Lozano, A. C. K. Soong, and J. C. Zhang, "What Will 5G Be?" *IEEE Journal on Selected Areas in Communications*, vol. 32, no. 6, pp. 1065–1082, Jun. 2014.

[2] A. D. Wyner, "Shannon-theoretic approach to a Gaussian cellular multiple-access channel," *IEEE Transactions on Information Theory*, vol. 40, no. 6, pp. 1713–1727, Nov. 1994.

[3] J. G. Andrews, F. Baccelli, and R. K. Ganti, "A tractable approach to coverage and rate in cellular networks," *IEEE Transactions on Communications*, vol. 59, no. 11, pp. 3122–3134, Nov. 2011.

[4] J. G. Andrews, A. K. Gupta, and H. S. Dhillon, "A primer on cellular network analysis using stochastic geometry," *arXiv:1604.03183 [cs, math]*, Apr. 2016.

[5] F. Baccelli, M. Klein, M. Lebourges, and S. Zuyev, "Stochastic geometry and architecture of communication networks," *Telecommunication Systems*, vol. 7, no. 1, pp. 209–227, Jun. 1997.

[6] Y. Li, F. Baccelli, H. S. Dhillon, and J. G. Andrews, "Statistical modeling and probabilistic analysis of cellular networks with determinantal point processes," *IEEE Transactions on Communications*, vol. 63, no. 9, pp. 3405–3422, 2015.

[7] M. Haenggi, "Mean interference in hard-core wireless networks," *IEEE Communications Letters*, vol. 15, no. 8, pp. 792–794, 2011.

[8] M. Haenggi, J. Andrews, F. Baccelli, O. Dousse, and M. Franceschetti, "Stochastic geometry and random graphs for the analysis and design of wireless networks," *IEEE Journal on Selected Areas in Communications*, vol. 27, no. 7, pp. 1029–1046, Sep. 2009.

[9] M. Haenggi, *Stochastic Geometry for Wireless Networks*. Cambridge: Cambridge University Press, 2012.

[10] Cisco, "Global mobile data traffic forecast update 20142019," *White Paper*, Feb. 2015.

[11] T. D. Novlan, H. S. Dhillon, and J. G. Andrews, "Analytical modeling of uplink cellular networks," *IEEE Transactions on Wireless Communications*, vol. 12, no. 6, pp. 2669–2679, 2013.

[12] A. Asadi, Q. Wang, and V. Mancuso, "A survey on device-to-device communication in cellular networks," *IEEE Communications Surveys & Tutorials*, vol. 16, no. 4, pp. 1801–1819, 2014.

[13] L. Wei, R. Q. Hu, Y. Qian, and G. Wu, "Enable device-to-device communications underlaying cellular networks: challenges and research aspects," *IEEE Communications Magazine*, vol. 52, no. 6, pp. 90–96, 2014.

[14] P. Xu, Y. Yuan, Z. Ding, X. Dai, and R. Schober, "On the outage performance of non-orthogonal multiple access with 1-bit feedback," *IEEE Transactions on Wireless Communications*, vol. 15, no. 10, pp. 6716–6730, 2016.

[15] Z. Ding, Z. Yang, P. Fan, and H. V. Poor, "On the performance of non-orthogonal multiple access in 5G systems with randomly deployed users," *IEEE Signal Processing Letters*, vol. 21, no. 12, pp. 1501–1505, 2014.

[16] L. Dai, B. Wang, Y. Yuan, S. Han, I. Chih-Lin, and Z. Wang, "Non-orthogonal multiple access for 5G: solutions, challenges, opportunities, and future research trends," *IEEE Communications Magazine*, vol. 53, no. 9, pp. 74–81, 2015.

[17] S. M. R. Islam, N. Avazov, O. A. Dobre, and K. S. Kwak, "Power-domain non-orthogonal multiple access (NOMA) in 5G systems: Potentials and challenges," *IEEE Communications Surveys & Tutorials*, vol. 19, no. 2, pp. 721–742, 2017.

[18] X. Ge, S. Tu, G. Mao, C. X. Wang, and T. Han, "5G ultra-dense cellular networks," *IEEE Wireless Communications*, vol. 23, no. 1, pp. 72–79, 2016.

[19] K. Doppler, M. Rinne, C. Wijting, C. Ribeiro, and K. Hugl, "Device-to-device communication as an underlay to lte-advanced networks," *IEEE Communications Magazine*, vol. 47, no. 12, pp. 42–49, 2009.

[20] T. Peng, Q. Lu, H. Wang, S. Xu, and W. Wang, "Interference avoidance mechanisms in the hybrid cellular and device-to-device systems," in *Proc. IEEE Pers. Indoor and Mobile Radio Commun. Symp. (PIMRC)*, 2010, pp. 617–621.

[21] S. Xu, H. Wang, T. Chen, and Q. Huang, "Effective interference cancellation scheme for device-to-device communication underlaying cellular networks," in *Proc. IEEE Veh. Technol. Conf. (VTC) Fall*, 2010, pp. 1–5.

[22] C. Xu, L. Song, Z. Han, and Q. Zhao, "Interference-aware resource allocation for device-to-device communications as an underlay using sequential second price auction," in *Proc. IEEE Int. Conf. Commun. (ICC)*, 2012, pp. 445–449.

[23] D. Feng, L. Lu, Y. W. Yi, G. Y. Li, G. Feng, and S. Li, "Device-to-device communications underlaying cellular networks," *IEEE Transactions on Communications*, vol. 61, no. 8, pp. 3541–3551, 2013.

[24] B. Zhou, H. Hu, S. Q. Huang, and H. H. Chen, "Intracluster device-to-device relay algorithm with optimal resource utilization," *IEEE Transactions on Vehicular Technology*, vol. 62, no. 5, pp. 2315–2326, 2013.

[25] J. C. F. Li, M. Lei, and F. Gao, "Device-to-device (d2d) communication in mu-mimo cellular networks," in *Proc. IEEE Global Commun. Conf. (GLOBECOM)*, 2012, pp. 3583–3587.

[26] N. Golrezaei, P. Mansourifard, A. F. Molisch, and A. G. Dimakis, "Base-station assisted device-to-device communications for high-throughput wireless video networks," in *Proc. IEEE Int. Conf. Commun. (ICC)*, 2014, pp. 7077–7081.

[27] N. Golrezaei, A. G. Dimakis, and A. F. Molisch, "Device-to-device collaboration through distributed storage," in *Proc. IEEE Global Commun. Conf. (GLOBECOM)*, 2012, pp. 2397–2402.

[28] Q. Wang and B. Rengarajan, "Recouping opportunistic gain in dense base station layouts through energy-aware user cooperation," in *World of Wireless, Mobile and Multimedia Networks*, 2013, pp. 1–9.

[29] "Wi-fi peer-to-peer (p2p) specification v1.1," *Wi-Fi Alliance*, vol. 1, pp. 1–159, 2010.

[30] "Zigbee specification," *Zigbee Alliance*, vol. 1, 2006.

[31] Bluetooth., "Bluetooth specification version 1.1," vol. 1, 2001. [Online]. Available: http://www.bluetooth.com

[32] S. Ding, "A survey on integrating manets with the internet: Challenges and designs," *Computer Communications*, vol. 31, no. 14, pp. 3537–3551, 2008.

[33] B. Wang and K. J. R. Liu, "Advances in cognitive radio networks: A survey," *IEEE Journal of Selected Topics in Signal Processing*, vol. 5, no. 1, pp. 5–23, 2011.

[34] J. Liu, N. Kato, J. Ma, and N. Kadowaki, "Device-to-device communication in lte-advanced networks: A survey," *IEEE Communications Surveys & Tutorials*, vol. 17, no. 4, pp. 1923–1940, 2015.

[35] K. Doppler, C. H. Yu, C. B. Ribeiro, and P. Janis, "Mode selection for device-to-device communication underlaying an LTE-advanced network," in *Proc. IEEE Wireless Commun. & Netw. Conf. (WCNC)*, 2010, pp. 1–6.

[36] H. Min, J. Lee, S. Park, and D. Hong, "Capacity enhancement using an interference limited area for device-to-device uplink underlaying cellular networks," *IEEE Transactions on Wireless Communications*, vol. 10, no. 12, pp. 3995–4000, 2011.

[37] Q. C. Li, R. Q. Hu, Y. Xu, and Y. Qian, "Optimal fractional frequency reuse and power control in the heterogeneous wireless networks," *IEEE Transactions on Wireless Communications*, vol. 12, no. 6, pp. 2658–2668, 2013.

[38] H. S. Chae, J. Gu, B. G. Choi, and Y. C. Min, "Radio resource allocation scheme for device-to-device communication in cellular networks using fractional frequency reuse," in *Proc. 17th Asia-Pacific Conf. Commun. (APCC)*, 2011, pp. 58–62.

[39] H. Zhu and J. Wang, "Device-to-device communication in cellular networks with fractional frequency reuse," in *Proc. IEEE Int. Conf. Commun. (ICC)*, 2014, pp. 5503–5507.

[40] P. Bao, G. Yu, and R. Yin, "Novel frequency reusing scheme for interference mitigation in D2D uplink underlaying networks," in *Proc. Int. Wireless Commun. Mobile Comput. Conf. (IWCMC)*, 2013, pp. 491–496.

[41] X. Lin, J. G. Andrews, and A. Ghosh, "Spectrum sharing for device-to-device communication in cellular networks," *IEEE Transactions on Wireless Communications*, vol. 13, no. 12, pp. 6727–6740, 2014.

[42] Z. Zhang, R. Q. Hu, Y. Qian, A. Papathanassiou, and G. Wu, "D2D communication underlay uplink cellular network with fractional frequency reuse," in *Proc. Int. Conf. Des. Reliable Commun. Netw. (DRCN)*, 2015, pp. 247–250.

[43] C. H. Yu, O. Tirkkonen, K. Doppler, and C. Ribeiro, "On the performance of device-to-device underlay communication with simple power control," in *Proc. IEEE Veh. Technol. Conf. (VTC) Spring*, 2009, pp. 1–5.

[44] J. Gu, S. J. Bae, B. G. Choi, and Y. C. Min, "Dynamic power control mechanism for interference coordination of device-to-device communication in cellular networks," in *Proc. 3rd Int. Conf. Ubiquitous Future Netw.*, 2011, pp. 71–75.

[45] C. H. Yu, K. Doppler, C. B. Ribeiro, and O. Tirkkonen, "Resource sharing optimization for device-to-device communication underlaying cellular networks," *IEEE Transactions on Wireless Communications*, vol. 10, no. 8, pp. 2752–2763, 2011.

[46] N. Lee, X. Lin, J. G. Andrews, and R. W. Heath, "Power control for D2D underlaid cellular networks: Modeling, algorithms, and analysis," *IEEE Journal on Selected Areas in Communications*, vol. 33, no. 1, pp. 1–13, 2015.

[47] J. Illian, P. Penttinen, H. Stoyan, and D. Stoyan, *Statistical Analysis and Modelling of Spatial Point Patterns*. Wiley, 2008.

[48] T. S. 3Gpp, "3rd generation partnership project; technical specification group radio access network; evolved universal terrestrial radio access (E-UTRA) and evolved universal terrestrial radio access network (E-UTRAN); overall description; stage 2 (release 8)," 2009.

[49] R. Q. Hu and Y. Qian, "An energy efficient and spectrum efficient wireless heterogeneous network framework for 5G systems," *IEEE Communications Magazine*, vol. 52, no. 5, pp. 94–101, 2014.

[50] Y. Liu, Z. Ding, M. Elkashlan, and H. V. Poor, "Cooperative non-orthogonal multiple access with simultaneous wireless information and power transfer," *IEEE Journal on Selected Areas in Communications*, vol. 34, no. 4, pp. 938–953, 2016.

[51] T. Cover, "Broadcast channels," *IEEE Transactions on Information Theory*, vol. 18, no. 1, pp. 2–14, 1972.

[52] S. Sen, N. Santhapuri, R. R. Choudhury, and S. Nelakuditi, "Successive interference cancellation: a back-of-the-envelope perspective," in *ACM Workshop on Hot Topics in Networks. (HOTNETS)*, 2010, pp. 1–6.

[53] M. O. Hasna, M. S. Alouini, A. Bastami, and E. S. Ebbini, "Performance analysis of cellular mobile systems with successive co-channel interference cancellation," *Wireless Communications IEEE Transactions on*, vol. 2, no. 1, pp. 29–40, 2003.

[54] 3GPP, "Study on downlink multiuser superposition transmission (MUST) for LTE," 3rd Generation Partnership Project (3GPP), Technical report (TR) 36.859, 04 2015, version 13.0.0. [Online]. Available: https://portal.3gpp.org/desktopmodules/Specifications/SpecificationDetails.aspx?specificationId=2912

[55] Z. Ding, X. Lei, G. K. Karagiannidis, R. Schober, J. Yuan, and V. Bhargava, "A survey on non-orthogonal multiple access for 5G networks: Research challenges and future trends," *IEEE Journal on Selected Areas in Communications*, vol. PP, no. 99, pp. 1–1, 2017.

[56] Y. Saito, Y. Kishiyama, A. Benjebbour, T. Nakamura, A. Li, and K. Higuchi, "Non-orthogonal multiple access (NOMA) for cellular future radio access," in *Proc. IEEE Veh. Technol. Conf. (VTC) Spring*, 2013, pp. 1–5.

[57] A. Benjebbour, A. Li, K. Saito, Y. Saito, Y. Kishiyama, and T. Nakamura, "NOMA: From concept to standardization," in *Standards for Communications and Networking*, 2016, pp. 18–23.

[58] D. Tse and P. Viswanath, *Fundamentals of wireless communication*. Cambridge, 2013.

[59] T. Takeda and K. Higuchi, "Enhanced user fairness using non-orthogonal access with SIC in cellular uplink," in *Proc. IEEE Veh. Technol. Conf. (VTC) Fall*, 2011, pp. 1–5.

[60] A. Benjebbour, Y. Saito, Y. Kishiyama, A. Li, A. Harada, and T. Nakamura, "Concept and practical considerations of non-orthogonal multiple access (NOMA) for future radio access," in *Proc. Int. Symp. Intell. Signal Process. Commun. Syst. (ISPACS)*, 2014, pp. 770–774.

[61] Y. Saito, A. Benjebbour, Y. Kishiyama, and T. Nakamura, "System-level performance of downlink non-orthogonal multiple access (NOMA) under various environments," in *Proc. IEEE Veh. Technol. Conf. (VTC) Spring*, 2015, pp. 1–5.

[62] Z. Ding, P. Fan, and H. V. Poor, "User pairing in non-orthogonal multiple access downlink transmissions," in *Proc. IEEE Global Commun. Conf. (GLOBECOM)*, 2015, pp. 1–5.

[63] N. Zhang, J. Wang, G. Kang, and Y. Liu, "Uplink non-orthogonal multiple access in 5G systems," *IEEE Communications Letters*, vol. 20, no. 3, pp. 458–461, 2016.

[64] S. Shi, L. Yang, and H. Zhu, "Outage balancing in downlink non-orthogonal multiple access with statistical channel state information," *IEEE Transactions on Wireless Communications*, vol. 15, no. 7, pp. 4718–4731, 2015.

[65] F. Liu, P. Mahonen, and M. Petrova, "Proportional fairness-based user pairing and power allocation for non-orthogonal multiple access," in *Proc. IEEE Pers. Indoor and Mobile Radio Commun. Symp. (PIMRC)*, 2015, pp. 1127–1131.

[66] Z. Zhang, H. Sun, R. Q. Hu, and Y. Qian, "Stochastic geometry based performance study on 5G non-orthogonal multiple access scheme," in *Proc. IEEE Global Commun. Conf. (GLOBECOM)*, 2017, pp. 1–6.

[67] A. Papoulis and S. U. Pillai, "Probability, random variables, and stochastic processes, fourth edition," vol. 111, no. 1, pp. 1637–1637, 2002.

[68] H. A. David, "Order statistics," *International Encyclopedia of the Social & Behavioral Sciences*, vol. 67, no. 339, pp. 10 897–10 901, 2001.

[69] H. Sun, B. Xie, R. Q. Hu, and G. Wu, "Non-orthogonal multiple access with SIC error propagation in downlink wireless MIMO networks," in *Proc. IEEE Veh. Technol. Conf. (VTC) Fall*, 2017.

[70] Z. Zhang and R. Q. Hu, "Uplink non-orthogonal multiple access with fractional power control," in *Proc. IEEE Wireless Commun. & Netw. Conf. (WCNC)*, 2017, pp. 1–6.

[71] Z. Zhang, R. Q. Hu, and Y. Qian, "D2d communication underlay in uplink cellular networks with distance based power control," in *Proc. IEEE Int. Conf. Commun. (ICC)*, 2016, pp. 1–6.

[72] Z. Ding, R. Schober, and H. V. Poor, "A general MIMO framework for NOMA downlink and uplink transmission based on signal alignment," *IEEE Transactions on Wireless Communications*, vol. 15, no. 6, pp. 4438–4454, 2016.

[73] Z. Yang, Z. Ding, P. Z. Fan, and N. Al-Dhahir, "A general power allocation scheme to guarantee quality of service in downlink and uplink NOMA systems," *IEEE Transactions on Wireless Communications*, vol. 15, no. 11, pp. 7244–7257, 2016.

[74] Z. Ding, P. Fan, and H. V. Poor, "On the coexistence between full-duplex and NOMA," *IEEE Wireless Communications Letters*, vol. PP, no. 99, pp. 1–1, 2018.

[75] S. N. Chiu, D. Stoyan, W. S. Kendall, and J. Mecke, Eds., *Stochastic Geometry and Its Applications*, ser. Wiley Series in Probability and Statistics. Chichester, UK: John Wiley & Sons, Ltd, Aug. 2013.

[76] N. Otao, Y. Kishiyama, and K. Higuchi, "Performance of non-orthogonal multiple access with SIC in cellular downlink using proportional fair-based resource allocation," in *Proc. IEEE Int. Symp. Wireless Commun. Syst. (ISWCS)*, 2012, pp. 476–480.

[77] A. Benjebbovu, A. Li, Y. Saito, Y. Kishiyama, A. Harada, and T. Nakamura, "System-level performance of downlink NOMA for future lte enhancements," in *Proc. IEEE Global Commun. Conf. (GLOBECOM) Workshops*, 2014, pp. 66–70.

[78] H. Elsawy and E. Hossain, "Analytical modeling of mode selection and power control for underlay D2D communication in cellular networks," *IEEE Transactions on Communications*, vol. 62, no. 11, pp. 4147–4161, 2014.

[79] Z. Ding, P. Fan, and H. V. Poor, "Impact of user pairing on 5G non-orthogonal multiple access," *IEEE Transactions on Vehicular Technology*, vol. 65, no. 8, pp. 6010–6023, 2014.

[80] R. Zhang and C. K. Ho, "MIMO broadcasting for simultaneous wireless information and power transfer," *IEEE Transactions on Wireless Communications*, vol. 12, no. 5, pp. 1989–2001, May 2013.

[81] Z. Yang, Z. Ding, P. Fan, and N. Al-Dhahir, "The impact of power allocation on cooperative non-orthogonal multiple access networks with SWIPT," *IEEE Transactions on Wireless Communications*, vol. PP, no. 99, pp. 1–1, 2017.

[82] P. Diamantoulakis, K. N. Pappi, Z. Ding, and G. K. Karagiannidis, "Wireless powered communications with non-orthogonal multiple access," *IEEE Transactions on Wireless Communications*, vol. 15, no. 12, pp. 8422–8436, 2016.

[83] Z. Ding, I. Krikidis, B. Sharif, and H. V. Poor, "Wireless information and power transfer in cooperative networks with spatially random relays," *Wireless Communications IEEE Transactions on*, vol. 13, no. 8, pp. 4440–4453, 2014.

[84] E. Boshkovska, D. W. K. Ng, N. Zlatanov, and R. Schober, "Practical non-linear energy harvesting model and resource allocation for SWIPT systems," *IEEE Communications Letters*, vol. 19, no. 12, pp. 2082–2085, 2015.

[85] X. Zhang and J. G. Andrews, "Downlink cellular network analysis with a dual-slope path loss model," *IEEE Transactions on Communications*, vol. 63, no. 5, pp. 1881–1894, 2015.

[86] C. Galiotto, N. K. Pratas, N. Marchetti, and L. Doyle, "A stochastic geometry framework for LoS/NLoS propagation in dense small cell networks," in *Proc. IEEE Int. Conf. Commun. (ICC)*, 2015, pp. 2851–2856.

[87] J. G. Andrews, T. Bai, M. Kulkarni, A. Alkhateeb, A. Gupta, and J. R. W. Heath, "Modeling and analyzing millimeter wave cellular systems," *IEEE Transactions on Communications*, vol. 65, no. 1, pp. 403–430, 2017.

[88] I. Atzeni, J. Arnau, and M. Kountouris, "Downlink cellular network analysis with LoS/NLoS propagation and elevated base stations," *IEEE Transactions on Wireless Communications*, vol. 17, no. 1, pp. 142–156, 2017.

[89] Y. Kim, T. J. Lee, and I. K. Dong, "Joint information and power transfer in SWIPT-enabled CRFID networks," *IEEE Wireless Communications Letters*, vol. 7, no. 2, pp. 186–189, Apr. 2018.

[90] M. A. Kishk and H. S. Dhillon, "Joint uplink and downlink coverage analysis of cellular-based RF-powered IoT network," *IEEE Transactions on Green Communications & Networking*, vol. 2, no. 2, pp. 446–459, June 2018.

[91] J. Liu, M. Sheng, L. Liu, and J. Li, "Network densification in 5G: From the short-range communications perspective," *IEEE Communications Magazine*, vol. 55, no. 12, pp. 96–102, 2017.

[92] Z. Zhang and R. Q. Hu, "Dense cellular network analysis with LoS/NLoS propagation and bounded path loss model," *IEEE Communications Letters*, vol. 22, no. 11, pp. 2386–2389.

[93] 3GPP, "Evolved Universal Terrestrial Radio Access (E-UTRA); Further advancements for E-UTRA physical layer aspects," 3rd Generation Partnership Project (3GPP), Technical report (TR) 36.814, 03 2017, version 9.2.0. [Online]. Available: https://portal.3gpp.org/desktopmodules/Specifications/SpecificationDetails.aspx?specificationId=2493